

**Automation of the Cytokinesis-Block  
Micronucleus assay using imaging flow cytometry  
for high throughput radiation biodosimetry**

by

**Matthew A. Rodrigues**

B.Sc. Applied Physics, Laurentian University, 2006  
M.Sc. Biomedical Physics, Ryerson University, 2008

A thesis submitted to the Faculty of Graduate and Postdoctoral Affairs

in partial fulfillment of the requirements for the degree of

**Doctor of Philosophy**

in

Physics, Specialization in Medical Physics

Ottawa-Carleton Institute of Physics  
Department of Physics  
CARLETON UNIVERSITY  
Ottawa, ON, Canada

May, 2015

© 2015, Matthew A. Rodrigues

## **ABSTRACT**

The cytokinesis-block micronucleus (CBMN) assay is employed in biodosimetry to determine the dose of radiation to exposed individuals from the frequency of micronuclei (MN) in binucleated lymphocyte cells (BNCs). The assay is traditionally performed using a microscope-based scoring procedure that can be labour-intensive, time consuming and subject to variability of interpretation between scorers. This thesis investigates the feasibility of adapting the CBMN assay to an imaging flow cytometry method using the ImageStream<sup>x</sup> (ISX) imaging flow cytometer and hypothesises that dose estimations can be obtained with adequate sensitivity for triage radiation biodosimetry.

A protocol to perform the CBMN assay on the ISX along with a data analysis method using the Image Data Exploration and Analysis Software (IDEAS®) were developed. Using irradiated whole blood samples it was shown that the ISX-CBMN method could automatically image and enumerate BNCs and MN. Additionally, between 0-4 Gy the rate of MN per BNC follows a linear quadratic dependence with dose, similar to what is observed when performing the assay using traditional protocols.

The ISX-CBMN method was then expanded into a multi-parameter radiation biodosimetry tool. Irradiated whole blood samples were analyzed using an optimized version of the IDEAS® analysis template that incorporated automated scoring of mononuclear cells (MNCs). Dose response calibration curves for the rate of MN per BNC, percentage of MNCs and the replication index (RI) were generated. Results indicated that this multi-parameter method may be able to provide dose estimations for individuals who have received a radiation dose of higher than 4 Gy.

The traditional CBMN assay is limited by the large blood culture volume (500  $\mu$ L - 2 mL) and the 72 h culture time. It was posited that the ISX-CBMN method could overcome both of these requirements and results showed that dose estimations could be generated

to within 0.5 Gy of the delivered dose after only 48 h of culture time with an initial blood volume of 200  $\mu$ L. The adaptation of the CBMN assay to an imaging flow cytometry method greatly increases its applicability in high throughput triage radiation biodosimetry.

## PREFACE

This thesis contains three manuscripts that, when taken together as a whole, outline the development, optimization and validation of automating the CBMN assay using imaging flow cytometry (FCM) for applications in radiation biodosimetry. Each manuscript, presented as a separate chapter in this thesis, has been expanded upon to include more details regarding the rationale, experimental methods and pertinent results.

Chapter 1 contains a general introduction to mass casualty events involving radiation, the biological and cellular effects of ionizing radiation, radiation biodosimetry and both traditional and imaging FCM. It also discusses the rationale for high-throughput automated methods for radiation biodosimetry.

Chapter 2 presents background information on the CBMN assay and standard protocols and procedures as applied to radiation biodosimetry. Also presented is an introduction to the principles and concepts of both traditional and imaging flow cytometry.

Chapter 3 is based on the manuscript entitled “Automated analysis of the cytokinesis-block micronucleus assay for radiation biodosimetry using imaging flow cytometry” published in *Radiation and Environmental Biophysics* (53(2), 273-282, 2014). Additional sections describing the procedure used to stain cells for DNA content, the use of cell surface markers and cytoplasm stains as well a more detailed description of the masking strategy used in IDEAS® are included.

Chapter 4 is based on the manuscript entitled “Multi-Parameter Dose Estimations in Radiation Biodosimetry using the Automated Cytokinesis-Block Micronucleus Assay with Imaging Flow Cytometry” published in *Cytometry Part A* (85(10), 883-893, 2014). Additional sections describing results on receiver operating characteristics (ROC) analysis of the automated scoring method in IDEAS® as well as individual donor variability are included.

Chapter 5 is based on the methods developed and results obtained for the manuscript entitled “Validation of the Cytokinesis-Block Micronucleus Assay using Imaging Flow Cytometry for High Throughput Triage Radiation Biodosimetry” submitted to Health Physics (March, 2015). Additional sections detailing the methods used to determine the minimum blood volume required to score sufficient BNCs, 0-10 Gy dose response calibration curves for the rate of MN per BNC for the 72 h, 200  $\mu$ L; 48 h, 2 mL and 48h, 200  $\mu$ L culture conditions as well as dose estimations on all blinded samples examined between 0-10 Gy are presented.

Chapter 6 contains a summary of the thesis findings and general conclusions on the advancements made in automating the CBMN assay using imaging FCM presented in this thesis as well as a short discussion on possible future work to be performed in this area of automated radiation biodosimetry

For consistency, the references have been unified throughout the thesis and are listed at the end of this thesis.

## STATEMENT OF ORIGINALITY

This thesis describes the results of research conducted by the author during the course of the Medical Physics Ph.D. program at Carleton University. Three separate manuscripts make up the thesis and are each presented as a separate chapter in this thesis document.

1. M.A. Rodrigues, L.A. Beaton-Green, B.C. Kutzner and R.C. Wilkins. “Automated analysis of the cytokinesis-block micronucleus assay for radiation biodosimetry using imaging flow cytometry” *Radiat. Environ. Biophys.* 53(2), 273-282. 2014. The results of this paper make up the majority of Chapter 3, which describes the adaptation and automation of the CBMN assay using the ISX imaging flow cytometer for radiation biodosimetry. I designed all experiments, performed all data collection and analysis and prepared and revised the manuscript for publication with the help of all co-authors.
2. M.A. Rodrigues, L.A. Beaton-Green, B.C. Kutzner and R.C. Wilkins. “Multi-Parameter Dose Estimations in Radiation Biodosimetry using the Automated Cytokinesis-Block Micronucleus Assay with Imaging Flow Cytometry” *Cytometry Part A.* (85(10), 883-893, 2014). The results of this paper make up the majority of Chapter 4, which describes a multi-parameter approach for blinded dose estimations using the automated CBMN method on an imaging flow cytometer. I designed all experiments, performed all data collection and analysis, and prepared and revised the manuscript for publication with the help of all co-authors.
3. M.A. Rodrigues, L.A. Beaton-Green and R.C. Wilkins. “Validation of the Cytokinesis-Block Micronucleus Assay using Imaging Flow Cytometry for High Throughput Triage Radiation Biodosimetry”. Submitted to *Health Physics* (March 2015). The results of this paper make up the majority of Chapter 5, which describe

the results of reducing both the initial culture time and blood volume necessary to perform the CBMN assay on the ISX imaging flow cytometer for the purposes of increased throughput in radiation biodosimetry. I designed all experiments, performed all data collection and analysis, and prepared the manuscript for publication with the help of all co-authors.

## **ACKNOWLEDGEMENTS**

It is somewhat surreal to think that four years have passed since I walked into my first class as a new PhD student at Carleton, and now here I am, putting the finishing touches on my thesis! During my time at Carleton my life has changed significantly, but while all of those changes were occurring, I managed to complete some very interesting research. Many thanks are owed to so many people who have made this thesis possible.

First, to my supervisor Dr. Ruth Wilkins for supporting, mentoring and encouraging me every step of the way. She allowed me to steer this project largely on my own but always provided advice and direction at all the right times. As a result of her guidance and the conversations we've had over the last four years, I have grown tremendously both as a scientist and as a person. She always made sure to remind me that one day I would get to this point, especially on the most difficult days when I really needed the reminder. During the final push to the end, she also always reminded me to go home and get some sleep! I could not be more grateful to have had Dr. Wilkins as a supervisor.

I must also thank the other members of the Radiobiology lab at Health Canada who supported me tremendously along the way. Thank you to Dr. Lindsay Beaton for always being there to discuss new research ideas, to pass manuscript drafts back and forth countless times and for suggesting that extra important idea that I hadn't thought of in so many of my experiment designs. Thank you to Sylvie Lachapelle and Catherine Ferrarotto for the blood draws from numerous anonymous donors over the years. None of my experiments would have been possible without your help. Finally, thank you to Barbara Kutzner for teaching me nearly everything I know about working in a biology laboratory, for jumping in and helping me to process samples when it became too much for one pair of hands, for lending an ear when I just needed someone to talk to...and for being my friend.

Thank you to all of my fellow teaching assistants and laboratory supervisors whom I worked with in the Carleton Physics department. Special thanks are due to Etienne Rollin and Tamara Rozina for doing their best with scheduling to accommodate my off-campus status and for always keeping things fun and good-natured as we imparted knowledge on a new crop of undergraduates every year.

To my family for your unconditional love and support during every moment of this journey. Thanks to my sister Sara for the long conversations (both in person and by email) about the trials and tribulations of PhD work, TAing and the good, bad and everything in between about life. Also, thank you for the numerous heavy metal concerts you've come to with me...we absolutely needed the escape from our desks! To my mother Jane, for not giving up all those years ago when the three of us were at the bottom of what seemed like an impossible mountain to climb. Without your constant life lessons, perseverance, work ethic and the countless sacrifices you have made, this degree would not have been possible and I would not be the man I am today. Thank you for everything. Somewhere, dad is looking down on us proudly...with his cigarette in one hand and his coffee mug in the other.

Finally, to Melissa Hillier. Thank you for walking into my life on that warm, sunny, spring afternoon and making it better than I ever could have possibly imagined. I am constantly inspired by the importance you place on family values, your remarkable work ethic and how you strive to live in selflessness. Your love and support as I worked tirelessly to wrap up this thesis has been more appreciated than any written words can adequately express. I am excited to experience all of the amazing things that the future has in store for us and to fall more in love with you with each day that passes.

# TABLE OF CONTENTS

ABSTRACT .....	II
PREFACE .....	IV
STATEMENT OF ORIGINALITY.....	VI
ACKNOWLEDGEMENTS.....	VIII
LIST OF TABLES .....	XVI
LIST OF FIGURES.....	XVII
1. INTRODUCTION.....	0
1.1. Introduction to radiation biodosimetry.....	0
1.2. Mass casualty events involving ionizing radiation .....	0
1.2.1. Malicious events .....	1
1.2.1.1. Radiological Exposure Devices (RED) .....	1
1.2.1.2. Radiological Dispersal Devices (RDD) .....	1
1.2.1.3. Improvised Nuclear Devices (IND).....	2
1.2.2. Accidental events.....	2
1.2.2.1. Nuclear reactor emergencies and criticality accidents .....	3
1.2.2.2. Lost or stolen radioactive sources .....	3
1.2.3. Biodosimetry requirements following mass casualty events .....	4
1.3. Biological effects of total body exposure to ionizing radiation .....	5
1.3.1. The Acute Radiation Syndrome (ARS).....	5
1.3.1.1. Prodromal radiation phase .....	6
1.3.1.2. The latent phase.....	6
1.3.1.3. The Hematopoietic syndrome.....	6
1.3.1.4. The Gastrointestinal syndrome .....	7
1.3.1.5. The Cerebrovascular syndrome .....	7
1.3.2. Summary of the ARS and further defining of biodosimetry requirements .....	8
1.4. Cellular effects of ionizing radiation .....	9
1.4.1. Single and double DNA strand breaks from direct or indirect action.....	9
1.4.2. Chromosome structure, damage and aberrations .....	10

1.4.2.1. The cell cycle, DNA replication and chromosome structure .....	10
1.4.2.2. Chromosomal aberrations as a result of ionizing radiation.....	12
1.4.2.3. Relation between dose and chromosomal aberrations .....	13
1.5. Bidosimetric assays for the quantification of radiation-induced DNA damage.....	15
1.5.1. Dicentric Chromosome Assay.....	15
1.5.2. CBMN assay.....	16
1.6. Flow cytometry .....	18
1.6.1. Traditional FCM .....	19
1.6.2. Imaging FCM .....	21
1.7. Thesis statement.....	22
1.7.1. Thesis statement .....	22
1.7.2. Thesis outline.....	23
1.7.3. Ethical considerations .....	23
2. BACKGROUND INFORMATION ON THE CBMN ASSAY FOR RADIATION BIODOSIMETRY AND IMAGING FCM.....	24
2.1. The traditional CBMN assay in radiation biodosimetry.....	24
2.1.1. Whole blood culture .....	24
2.1.2. Culture processing and slide preparation .....	25
2.1.3. Scoring the slides .....	26
2.1.4. Manual scoring methods.....	27
2.1.5. Automated scoring methods .....	28
2.1.5.1. Slide-based scoring using Metafer MNScore and IMSTAR Pathfinder™ software.....	29
2.1.5.2. Automated scoring using FCM methods.....	32
2.2. Imaging FCM on the ImageStream <sup>x</sup> .....	33
2.2.1. Overview.....	33
2.2.2. Illumination, optics and image collection .....	34
2.2.3. IDEAS® (Image Data Exploration and Analysis Software) for the ISX ...	35

3. AUTOMATED ANALYSIS OF THE CYTOKINESIS-BLOCK MICRONUCLEUS ASSAY FOR RADIATION BIODOSIMETRY USING IMAGING FLOW CYTOMETRY .....	39
3.1. Summary.....	39
3.2. Introduction .....	39
3.3. Materials and methods .....	40
3.3.1. Blood collection and irradiation .....	40
3.3.2. Blood collection and irradiation for 0-1 Gy calibration curves .....	41
3.3.3. CBMN assay.....	41
3.3.4. DNA staining with DRAQ5 .....	41
3.3.5. Cytoplasm stains and cell surface markers .....	43
3.3.6. Data collection on the ImageStream <sup>x</sup> .....	46
3.3.7. Data analysis in IDEAS® .....	47
3.4. Results .....	54
3.5. Discussion.....	58
3.6. Acknowledgements .....	63
4. MULTI-PARAMETER DOSE ESTIMATIONS IN RADIATION BIODOSIMETRY USING THE AUTOMATED CYTOKINESIS-BLOCK MICRONUCLEUS ASSAY WITH IMAGING FLOW CYTOMETRY .....	64
4.1. Summary.....	64
4.2. Introduction .....	64
4.3. Materials and methods .....	65
4.3.1. Blood collection, irradiation, CBMN assay and data collection on the ImageStream <sup>x</sup> .....	65
4.3.2. Receiver operating characteristics .....	65
4.3.3. Individual donor variability in the ISX-CBMN method .....	67
4.3.3.1. Blood collection, irradiation and CBMN assay for donor variability ..	67
4.3.3.2. Data collection on the ImageStream <sup>x</sup> and data analysis .....	68
4.4. Results .....	68
4.4.1. Data analysis in IDEAS® .....	68
4.4.2. Calibration curves .....	76
4.4.3. Receiver operating characteristics .....	80

4.4.3.1. Receiver operating characteristics for micronuclei.....	81
4.4.3.2. Receiver operating characteristics for binucleated cells.....	83
4.4.4. Intra-donor variability in the ISX-CBMN method.....	84
4.5. Discussion.....	89
5. VALIDATION OF THE CYTOKINESIS-BLOCK MICRONUCLEUS ASSAY USING IMAGING FLOW CYTOMETRY FOR HIGH THROUGHPUT TRIAGE RADIATION BIODOSIMETRY .....	100
5.1. Summary.....	100
5.2. Introduction .....	100
5.3. Materials and methods .....	102
5.3.1. Determination of minimum culture volume .....	102
5.3.2. Blood collection, irradiation and CBMN assay for calibration curves ....	103
5.3.3. Blood collection, irradiation and CBMN assay for validation with blinded samples.....	104
5.3.4. Data collection on the ImageStream <sup>x</sup> and data analysis .....	104
5.4. Results.....	105
5.4.1. Dose response calibration curves and estimation of blinded doses between 0-10 Gy .....	105
5.4.2. Estimation of blinded doses between 0-10 Gy .....	108
5.4.2.1. Dose response calibration curves between 0-4 Gy.....	113
5.4.2.2. Estimation of blinded doses between 0-4 Gy.....	115
5.4.2.3. Determination of the standard error on dose estimations.....	118
5.4.3. Minimum collection time required to estimate doses to within 0.5 Gy...	119
5.5. Discussion.....	121
5.6. Conclusion .....	126
6. GENERAL CONCLUSIONS.....	128
6.1. Summary of thesis findings .....	128
6.2. Further work and suggested improvements with the ISX-CBMN method....	130
6.3. Concluding remarks .....	132
REFERENCES.....	134
APPENDIX I – AUTOMATED CBMN: STANDARD PROTOCOL ON THE ISX .....	142

## LIST OF ABBREVIATIONS

$\alpha$	Alpha particle
$\beta$	Beta particle
$\gamma$	Gamma photons
ARS	Acute Radiation Syndrome
BF	Brightfield
BNC	Binucleated Cell
CABAS	Chromosome Aberration Calculation Software
CBMN	Cytokinesis-Block Micronucleus
CCD	Charge Coupled Device
CCRPB	Consumer and Clinical Radiation Protection Bureau
CI	Confidence Interval
CSF	Colony-Stimulating Factor
Cyt-B	Cytochalasin B
DAPI	4',6-diamidino-2-phenylindole
DCA	Dicentric Chromosome Assay
DNA	Deoxyribonucleic Acid
DSB	Double Strand Break
FBS	Fetal Bovine Serum
FCM	Flow Cytometry
FISH	Fluorescence <i>In Situ</i> Hybridization
FL	Fluorescent Channel
FN	False Negative
FP	False Positive
FSC	Forward Scatter
Gy	Gray
IAEA	International Atomic Energy Agency
IDEAS®	Image Data Exploration and Analysis Software
IND	Improvised Nuclear Device
ISX	ImageStream <sup>x</sup>
LD <sub>50</sub>	Median Lethal Dose
LED	Light Emitting Diode
LQM	Linear Quadratic Model

MN	Micronucleus
MNC	Mononuclear Cell
PBL	Peripheral Blood Lymphocyte
PBS	Phosphate Buffered Saline
PCC	Premature Chromosome Condensation
PHA	Phytohaemagglutinin
PMT	Photomultiplier Tube
R/N	Radiological/Nuclear
RBC	Red Blood Cell
RDD	Radiological Dispersal Device
RED	Radiological Exposure Device
RI	Replication Index
RPMI	Roswell Park Memorial Institute
RT	Room Temperature
SEM	Standard Error of the Mean
SSB	Single Strand Break
SSC	Side Scatter
TDI	Time Delay Integration
TN	True Negative
TP	True Positive
WBC	White Blood Cell

## LIST OF TABLES

<b>Table 4-1:</b> Number of TP, FP, TN and FN MN in the original and optimized IDEAS® analysis template.....	82
<b>Table 4-2:</b> ROC characteristics for MN in the original analysis template for all doses....	82
<b>Table 4-3:</b> ROC characteristics for MN in the optimized analysis template for all doses.....	82
<b>Table 4-4:</b> Number of TP, FP, TN and FN BNCs in the original and optimized analysis templates. ....	83
<b>Table 4-5:</b> ROC characteristics for BNCs in the original analysis template for all doses.....	83
<b>Table 4-6:</b> ROC characteristics for BNCs in the optimized analysis template for all doses. ....	84
<b>Table 5-1:</b> The number of BNCs scored at each culture volume using the IDEAS® template .....	103
<b>Table 5-2:</b> Coefficient values calculated for each quadratic fit for the four calibration curves .....	114

## LIST OF FIGURES

<b>Figure 1-1:</b> Illustration of the three major syndromes of the ARS and the latent phase ...	8
<b>Figure 1-2:</b> Direct and indirect action of radiation .....	10
<b>Figure 1-3:</b> Schematic of the size ranges and stages of a chromosome adapted from Hall and Giaccia [16] .....	12
<b>Figure 1-4:</b> Illustrations of various chromosome aberrations .....	13
<b>Figure 1-5:</b> Frequency of chromosomal aberrations per cell as a function of dose .....	14
<b>Figure 1-6:</b> Hydrodynamic focusing in the ISX .....	19
<b>Figure 1-7:</b> Schematic of a typical flow cytometer .....	20
<b>Figure 1-8:</b> A typical dot plot and histogram generated from FCM data.....	21
<b>Figure 2-1:</b> BNC/MN formation and acridine orange-stained cells.....	26
<b>Figure 2-2:</b> The ISX along with a screenshot of the INSPIRE software .....	33
<b>Figure 2-3:</b> Optics and illumination of the ISX .....	34
<b>Figure 2-4:</b> Screenshot of the layout of the IDEAS® software.....	35
<b>Figure 2-5:</b> Plots generated in the analysis area of the IDEAS® software.....	36
<b>Figure 2-6:</b> Illustrations of the use of various masks in the IDEAS® software .....	38
<b>Figure 3-1:</b> The excitation and emission spectra of DRAQ5.....	42
<b>Figure 3-2:</b> Images from the ISX illustrating the use of the BF, DRAQ5, CD3 and PKH67 stains.....	45
<b>Figure 3-3:</b> Scatter plot of DRAQ5 lobe count versus aspect ratio .....	48
<b>Figure 3-4:</b> Histogram of BF aspect ratio .....	48
<b>Figure 3-5:</b> Histogram of DRAQ5 area .....	50
<b>Figure 3-6:</b> Scatter plot of DRAQ5 width versus homogeneity .....	51
<b>Figure 3-7:</b> Scatter plot of DRAQ5 aspect ratio intensity versus compactness .....	51
<b>Figure 3-8:</b> DRAQ5-stained BNC and MN with associated masks .....	53
<b>Figure 3-9:</b> Histogram of the spot count feature created using the BNC and MN masks.....	54
<b>Figure 3-10:</b> Various images captured by the ISX.....	55
<b>Figure 3-11:</b> Data from four experiments as well as the dose response curve from 0 to 4 Gy .....	56
<b>Figure 3-12:</b> Data from four experiments from 0 to 7 Gy .....	57
<b>Figure 3-13:</b> Data from five experiments from 0 to 1 Gy.....	58
<b>Figure 4-1:</b> Confusion matrix and typical performance metrics calculated using the matrix. ....	66
<b>Figure 4-2:</b> Scatter plot of DRAQ5 area versus intensity for elimination of debris .....	69
<b>Figure 4-3:</b> A histogram of BF aspect ratio.....	70
<b>Figure 4-4:</b> Scatter plot of DRAQ5 lobe count versus aspect ratio intensity .....	71
<b>Figure 4-5:</b> Scatter plot of DRAQ5 aspect ratio intensity versus DRAQ5 compactness.....	72
<b>Figure 4-6:</b> Scatter plot of DRAQ5 symmetry versus BF contrast.....	73
<b>Figure 4-7:</b> Scatter plot of DRAQ5 correlation versus contrast.....	73
<b>Figure 4-8:</b> Various cell images from the ISX.....	75
<b>Figure 4-9:</b> Histogram of the spot count feature created using the BNC and MN masks.....	76
<b>Figure 4-10:</b> Scatter plot of lobe count using the mononuclear mask versus DRAQ5 aspect ratio intensity.....	76

<b>Figure 4-11:</b> Rate of MN per BNC versus dose (Gy) for six donors (3 male (m), 3 female (f)).	77
<b>Figure 4-12:</b> Average rate of MN per BNC versus dose (Gy)	78
<b>Figure 4-13:</b> The percentage of MNCs versus dose for 6 donors (3 male (m) and 3 female (f)).	79
<b>Figure 4-14:</b> The weighted average percentage of MNCs versus dose (Gy)	79
<b>Figure 4-15:</b> The RI versus dose for 6 donors (3 male (m) and 3 female (f))	80
<b>Figure 4-16:</b> Average RI versus dose (Gy)	80
<b>Figure 4-17:</b> Box and whisker plots for 24 data points collected at 0 Gy from donor 21(m)	85
<b>Figure 4-18:</b> Box and whisker plots for 25 data points collected at 2 Gy from donor 21(m)	85
<b>Figure 4-19:</b> Box and whisker plots for 25 data points collected at 0 Gy from donor 28(m)	87
<b>Figure 4-20:</b> Box and whisker plots for 25 data points collected at 2 Gy from donor 28(m)	87
<b>Figure 4-21:</b> Box and whisker plot for donors 21(m) and 28(m) at both 0 Gy and 2 Gy	89
<b>Figure 5-1:</b> Average rate of MN per BNC versus dose (Gy) for the 48 h, 2 mL culture condition	106
<b>Figure 5-2:</b> Average rate of MN per BNC versus dose (Gy) for the 72 h, 200 $\mu$ L culture condition	107
<b>Figure 5-3:</b> Average rate of MN per BNC versus dose (Gy) for the 48 h, 200 $\mu$ L culture condition	107
<b>Figure 5-4:</b> Dose estimations based on the rate of MN per BNC	109
<b>Figure 5-5:</b> Dose estimation based on the percentage of MNCs	109
<b>Figure 5-6:</b> Dose estimation based on the RI	110
<b>Figure 5-7:</b> Estimated dose (Gy) versus delivered dose (Gy) determined by the ISX-CBMN method for all 20 blinded samples using the four culture conditions	112
<b>Figure 5-8:</b> Calibration curves from 0 to 4 Gy for the four culture time and volume conditions	114
<b>Figure 5-9:</b> Estimated dose (Gy) versus delivered dose (Gy) determined by the ISX CBMN method for all nine unknown samples using the four culture time and volume conditions	117
<b>Figure 5-10:</b> Average absolute value of the difference between the estimated dose and the delivered dose (Gy) versus collection time for all unknown samples cultured for 72 h with initial blood volumes of 2 mL and 200 $\mu$ L	120
<b>Figure 5-11:</b> Average absolute value of the difference between the estimated dose and the delivered dose (Gy) versus collection time for all unknown samples cultured for 48 h with initial blood volumes of 2 mL and 200 $\mu$ L	120

## **1. INTRODUCTION**

### **1.1. Introduction to radiation biodosimetry**

Radiation biological dosimetry (biodosimetry) is the use of biological markers to assess the dose received by an individual following exposure to ionizing radiation. When an individual or a large population of people have been exposed to high doses (>2 Gy), such as in a radiation accident, rapid decisions regarding triage and therapy must be made. An ideal biodosimeter should have the capacity to estimate doses with sufficient accuracy, thereby providing confirmation of each patient's medical triage status. Lloyd et al. have provided dose estimation ranges considered to be of sufficient accuracy for triage through the use of biodosimetry methods. For doses below 4 Gy, between 4 – 6 Gy and above 8 Gy, estimations within  $\pm 0.5$  Gy,  $\pm 1.0$  Gy and  $\pm 2.0$  Gy, respectively, of the true value are considered acceptable [1].

Several methods of biodosimetry are available, all of which quantify and correlate permanent damage of critical cellular structures to a dose estimation. The Dicentric Chromosome Assay (DCA), Cytokinesis-Block Micronucleus (CBMN) assay, Fluorescence *In Situ* Hybridization (FISH) and Premature Chromosome Condensation (PCC) assay are all examples of well-established biodosimeters with the DCA being the gold standard [2-4]. The advantages and disadvantages of some of these biodosimeters are discussed in section 1.5 with the focus of this thesis being on the CBMN assay.

### **1.2. Mass casualty events involving ionizing radiation**

A mass casualty event is defined as an event that involves injury to a significant number of individuals and as such, strains or exceeds the response capability of local emergency responders. When such an event involves ionizing radiation, the result may

be a large population that has received a wide range of doses with some being high enough to cause severe medical consequences or death. A number of publications have divided mass casualty situations into various subsets of malicious and accidental events. Regardless of the nature of the event, the ability to access laboratories which can perform biodosimetric assays to generate estimates of the doses received is critical [4-6].

### **1.2.1. Malicious events**

Scenarios for malicious events involving the deliberate exposure of a population to ionizing radiation have been identified and are typically listed in three broad categories: Radiological Exposure Devices (RED), Radiological Dispersal Devices (RDD) and Improvised Nuclear Devices (IND).

#### **1.2.1.1. Radiological Exposure Devices (RED)**

The use of a RED would involve the placement of a sealed radioactive source, such as Co-60 or Cs-137, in a densely populated environment in an attempt to deliberately expose large numbers of people to high doses of ionizing radiation. Depending on the location of the device (e.g. shopping mall, concert, sports stadium, etc.) and the length of time spent near it, tens to hundreds of people may be exposed to a wide range of doses [7]. In a scenario such as this, it is anticipated that the number of people receiving a high dose (> 2 Gy) would be low [5].

#### **1.2.1.2. Radiological Dispersal Devices (RDD)**

A RDD involves the use of an explosive or mechanical device to disseminate radiological material over a densely populated area resulting in radioactive contamination of the area and exposure of members of the public. It is anticipated that a relatively small

area would be impacted, but if the device is located in a densely populated area (e.g. downtown of a large metropolis) there may be hundreds to thousands of casualties. External contamination (radioactive material adhered to one's body or clothing) and internal contamination (inhalation or ingestion of radioactive material) are also possible which would increase the doses received. Overall, doses received by exposed individuals would depend on the type and amount of radioactive material used. While it is generally accepted that most doses would be lower than 1 Gy, there is the possibility that a number of individuals in close proximity to the explosion might receive doses of 2 Gy or higher and would require prompt medical treatment [5, 8].

#### **1.2.1.3. Improvised Nuclear Devices (IND).**

An IND is a device in which nuclear material (e.g. highly enriched uranium) is detonated causing considerable explosive damage as well as significant injury and death from the initial explosion, heat generation and ionizing radiation. The effects of such an event occurring in a major metropolitan area would be catastrophic and would result in hundreds to thousands of casualties requiring medical treatment for various physical injuries as well as for high radiation doses (> 2 Gy).

#### **1.2.2. Accidental events**

As with malicious events, scenarios involving the accidental exposure of a population or an individual to ionizing radiation have been identified and are grouped into the following categories: nuclear reactor emergencies and criticality accidents, and lost or stolen radioactive sources.

### **1.2.2.1. Nuclear reactor emergencies and criticality accidents**

Nuclear reactor emergencies or criticalities occur when the nuclear fuel inside a reactor is breached, or when uncontrolled nuclear fission occurs inadvertently. Both of these situations can result in significant doses to anyone in close proximity to the site, including nuclear energy workers and members of the public. The accidents at the Chernobyl (Ukraine) and Fukushima (Japan) nuclear power plants in 1986 and 2011 respectively are considered to be the two of the worst accidents in history. Following the release of radioactive material at Chernobyl, 134 plant staff and emergency personnel received radiation doses greater than 1 Gy which resulted in the acute radiation syndrome (ARS), and 28 later died [9]. The aftermath of the Fukushima plant accident was much less severe with no deaths resulting from radiation exposure. However, it has been estimated that approximately 200,000 members of the general public were screened for radiation exposure and contamination, and 30 plant workers received doses greater than 100 mGy resulting in hospitalization [10, 11].

### **1.2.2.2. Lost or stolen radioactive sources**

An event involving lost or stolen radioactive sources can result in several different exposure scenarios depending on factors such as the specific isotope involved, activity, length of exposure and its distribution. As such, the population affected by such an event is highly unpredictable but these events typically result in high whole body or partial body exposures to individuals in close proximity to the radioactive source [5]. Two of the most serious radiation accidents involving the exposure to and/or direct contact with radioactive sources occurred in Goiania, Brazil and Samut Prakarn, Thailand. In 1987 in Goiania, an abandoned Cs-137 radiotherapy unit was stolen and broken open, resulting in dispersal of radioactive material around the city. Of the 112,000 people screened for

exposure/contamination, 249 were determined to be contaminated and four would later die as a direct result of total body radiation doses estimated to be between 4-6 Gy [12]. In 2000 in Samut Prakarn, a similar accident occurred involving a stolen and opened Co-60 radiotherapy unit. The unit was transported to a junkyard where the source was removed and 60 individuals were exposed and/or contaminated, including 52 clean-up workers. Three people died as a consequence of their exposure with total body doses estimated to be in excess of 6 Gy [13].

### **1.2.3. Biodosimetry requirements following mass casualty events**

Following a radiation emergency such as the ones described above, physical dosimetry through the use of dosimeters or dose reconstruction techniques, that can provide an estimation of the dose received by exposed individuals, will likely not be available. In this case, biodosimetry through the use of cytogenetic assays that identify damage to critical cell structures becomes one of the only ways to approximate the dose received. In addition, a key advantage of biodosimetry, relative to physical dosimetry, is that it also accounts for individual variation in radiation sensitivity. When biodosimetry must be performed on large numbers of casualties, obtaining dose estimations quickly is critical to determine the proper treatment course. Medical intervention is typically only required for patients receiving a dose of 1 Gy or higher, thus cytogenetic assays that can rapidly and reliably identify this dose threshold within a few days of exposure are ideal [1]. This dictates a need to develop guidelines and operating procedures for the organization and management of the triage of large numbers of casualties based on dose assessment in order to rapidly identify and begin timely preventive measures to individuals at risk of developing the ARS [14]. Biodosimetry is essential to this process but most cytogenetic assays in their current forms do not meet the demands of a mass casualty accident or

emergency. Recently, automated or semi-automated systems have been developed to increase throughput capabilities that could provide rapid initial dose estimates for large numbers of casualties [15].

### **1.3. Biological effects of total body exposure to ionizing radiation**

Following a total body exposure to radiation, a number of biological processes take place that can be fatal at high doses. At doses of 1 Gy, symptoms of the ARS will begin to develop and the median lethal dose (LD<sub>50</sub>) is 4 Gy, at which point 50% of individuals exposed will die in the absence of medical intervention. It has been speculated that the LD<sub>50</sub> can be increased to 7 Gy with careful nursing and antibiotic treatments and possibly through bone marrow transplants. This illustrates the need for rapid dose estimations using biodosimetry such that medical intervention can begin as quickly as possible [16].

#### **1.3.1. The Acute Radiation Syndrome (ARS)**

The ARS is caused by high doses of irradiation (>1 Gy) of the entire body, or most of the body, in a short time period (seconds to minutes) [17]. Three distinct syndromes which manifest themselves as a result of exposure to ionizing radiation make up the ARS; the hematopoietic, gastrointestinal and cerebrovascular (or neurovascular) syndromes. As a precursor to each one of these syndromes, the prodromal radiation phase, where specific symptoms appear immediately following irradiation, as well as a latent phase, where the patient may appear symptom free for a certain time interval after irradiation, also manifest themselves [16].

#### **1.3.1.1. Prodromal radiation phase**

The prodromal radiation phase describes the symptoms that appear shortly after radiation exposure and last for approximately 48 h. Hallmarks of this phase are nausea and vomiting, but fever, headache and erythema (reddening of the skin) have also been observed. Additionally, a depletion of various subsets of white blood cells (T-lymphocytes, B-lymphocytes, neutrophils, eosinophils) occurs after exposure to ionizing radiation [18]. It has been suggested in the literature that it may be possible to use lymphocyte counts as an initial estimator of dose during the prodromal phase but this requires multiple blood draws that can be difficult to obtain in mass casualty situations [16, 17].

#### **1.3.1.2. The latent phase**

At total body doses close to the  $LD_{50}$ , a symptom-free interval of time (with apparent clinical improvement) known as the latent phase follows the prodromal syndrome. The time interval depends on the dose received but it is typically between 7 days for doses of 8 Gy and 30 days for doses of 2 Gy. During the latent phase the hematopoietic stem cells are significantly depleted and towards the end of this phase a number of symptoms develop including infection, fever, bleeding and possibly anemia [16].

#### **1.3.1.3. The Hematopoietic syndrome**

Blood stem cells (hematopoietic cells) are highly sensitive to ionizing radiation due to their rapid turnover. The threshold of the hematopoietic syndrome is 2 Gy and at total body doses between 2-5 Gy, nausea, vomiting, fatigue, fever and erythema are the typical symptoms. Death, if it occurs, is typically as a result of a lack of blood stem cell elements available to replenish the mature blood cells that die off [16, 17]. Cytokine therapy through the use of colony-stimulating factors (CSFs) to restore blood stem cells has been shown

to be beneficial in some cases. CSFs are proteins that induce bone marrow stem cells to proliferate and differentiate into specific mature blood cell types [19]. A number of individuals involved in radiation accidents receiving whole body doses in the range of 2-5 Gy have received cytokine therapy with various CSFs and many have survived as a result of the treatment [19].

#### **1.3.1.4. The Gastrointestinal syndrome**

The gastrointestinal syndrome occurs at doses of 6-10 Gy with symptoms of nausea, vomiting and cramping of the abdomen that will typically occur within 1-2 h. Stem cells inside the glands of the intestines (crypts) that are responsible for producing new cells for the villi (finger-like projections that aid in the absorption of nutrients) die as a result of doses in the range of 6-10 Gy. The cells on the surface of the villi continue to be rubbed away by normal digestive processes with no replacement cells produced in the crypts. Consequently, the villi shorten, shrink and eventually the surface lining of the intestine is completely devoid of cells, resulting in the inability of the intestines to absorb nutrients that leads to death within 3-10 days following exposure [16, 17, 20].

#### **1.3.1.5. The Cerebrovascular syndrome**

The organs of the nervous system (brain, spinal cord) are generally regarded as being quite resistant to the effects of ionizing radiation, mostly as a result of the slow rate of cell replication [16]. However, at whole body doses approaching and exceeding 10 Gy, death typically occurs within 24-48 h. Clinical features of this syndrome include severe nausea and vomiting, fever, headache, dizziness, confusion and disorientation. The cause of death from this syndrome is not well understood but has been attributed to an increase in

the fluid content inside the brain from damaged small vessels resulting in a buildup of pressure within the skull [16, 17].

### 1.3.2. Summary of the ARS and further defining of biodosimetry requirements

Figure 1-1 illustrates the three major syndromes of the ARS as well as the latent phase times (in days) associated with each syndrome. The latent phase shortens with increasing dose and therefore, it is advantageous to perform physical and biological dosimetry to estimate radiation dose as rapidly as possible. A rapid biodosimetry method that can accurately estimate doses of 2 Gy or greater within the first 7-10 days following exposure is ideal, allowing medical treatments such as cytokine therapy, antibiotics for infection, platelet transfusions and bone marrow transplantation to begin as soon as possible. There is therefore a need for a rapid, robust, high-throughput biodosimetry assay to aid in emergency medical triage where a large number of individuals may have received high doses of ionizing radiation as well as to identify and provide reassurance for those who have not been exposed.

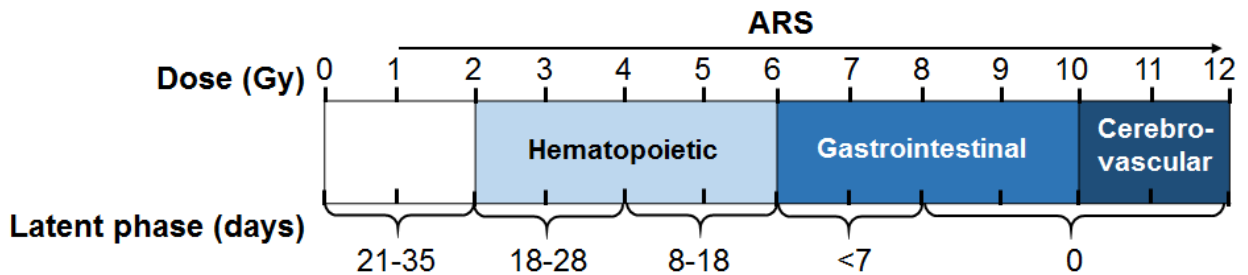


**Figure 1-1:** Illustration of the three major syndromes of the ARS and the latent phase length (in days) associated with each syndrome.

## **1.4. Cellular effects of ionizing radiation**

It is well-known that deoxyribonucleic acid (DNA) is the primary target for cell damage from ionizing radiation. DNA damage can occur as a result of direct action in which particulate radiation, such as electrons produced by photons in Compton and photoelectric interactions, strike the DNA molecules. Alternatively, damage may be caused by indirect action where photons interact with molecules in the cell (typically water) resulting in the production of free radicals that in turn damage critical structures in the DNA [16]. The following sections describe in more detail the effects of ionizing radiation on DNA, the biological effects of exposure to high doses of whole body irradiation and the use of biodosimetric assays to quantify dose.

### **1.4.1. Single and double DNA strand breaks from direct or indirect action**

The double-helix structure of DNA has been well described and consists of two strands, composed of alternating deoxyribose sugar and phosphate groups. Two pairs of nitrogen bases, adenine-thymine and cytosine-guanine, attach to the strands and hold them together through hydrogen bonding. Ionizing radiation, in the form of gamma ( $\gamma$ ) or X-ray photons, liberate photoelectrons (via the photoelectric effect) or recoil electrons (via Compton scatter) from atoms inside surrounding cells. In turn, these secondary electrons can interact with DNA in two ways: directly or indirectly. In direct action, secondary electrons strike the DNA directly, causing breaks in one or both strands. In indirect action, secondary electrons interact with other molecules (e.g. water) inside the cell to produce free radicals (usually hydroxyl radicals) which then damage the DNA [16]. These processes are illustrated in Figure 1-2.

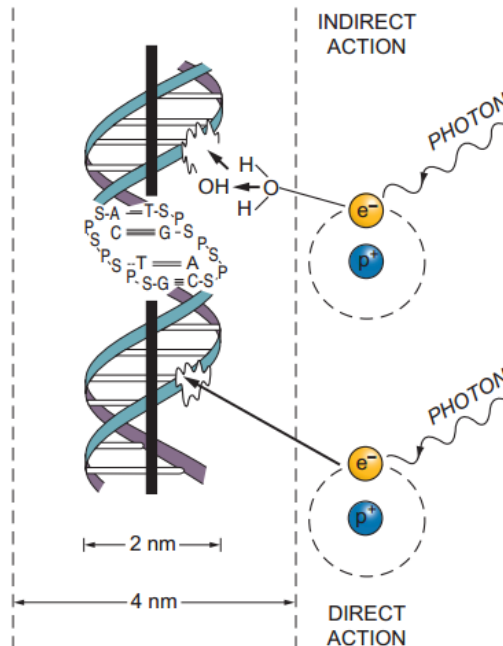


**Figure 1-2:** Direct and indirect action of radiation. **Top:** indirect action, where a secondary electron interacts with a water molecule to produce a hydroxyl radical that in turn damages the DNA strand. **Bottom:** direct action, where a secondary electron strikes the DNA strand directly. From Hall and Giaccia (2012) with permission [16].

Typically, a single strand break (SSB) is of little consequence to the cell, as the opposing strand provides a template for repair. However, a double strand break (DSB) can occur when two SSBs occur opposite one another and are close together in time and space (separation of only a few base pairs). In this case, the DNA helix breaks into two separate pieces and the damage is more difficult to repair. These DSBs can result in cell death if they cannot be adequately repaired or chromosome mutations (discussed below) if the damage is repaired incorrectly [16].

## 1.4.2. Chromosome structure, damage and aberrations

### 1.4.2.1. The cell cycle, DNA replication and chromosome structure

All cells containing nuclei go through a process known as the cell cycle, in which DNA replication and cell division are the main objectives. Cells spend approximately 90% of the

cell cycle in interphase, which is divided into 3 separate sub-phases:  $G_1$  (first gap), S (synthesis), and  $G_2$  (second gap). The cell increases to about double its size during the  $G_1$  phase, a presynthetic gap where the cell readies itself for DNA synthesis. DNA synthesis occurs during the S phase through a process called replication, where the chromosome material is duplicated.  $G_2$  is the final gap before division where the cell continues to grow, the chromosome material is condensed and the cell prepares for division. Following  $G_2$ , the cell proceeds through mitosis, where the chromosomes are separated into two identical sets each contained in their own individual nucleus, and then cytokinesis where the cell divides into two new cells. Between  $G_2$  and mitosis, the chromatin (a macromolecule consisting of DNA, RNA and proteins) begins to condense and chromosomes are formed. The series of events that make up mitosis are divided into several stages; prophase (chromatin condenses into chromosomes), prometaphase (nuclear membrane disintegrates), metaphase (chromosomes converge at the center of the cell on what is known as the metaphase plate), anaphase (chromosomes are separated and resulting chromatids move towards opposite ends of the cell) and telophase (the completion of mitosis in which both sets of chromosomes are surrounded by a new nuclear membrane) [21]. Figure 1-3 shows the structure of a typical condensed metaphase chromosome that consists of a centromere where the sister chromatids attach, with p- (small) and q- (large) arms extending from the centromere [16, 21]. Most modern biodosimetry assays to quantify radiation dose are performed on metaphase chromosomes such that damage can be visualized and scored.

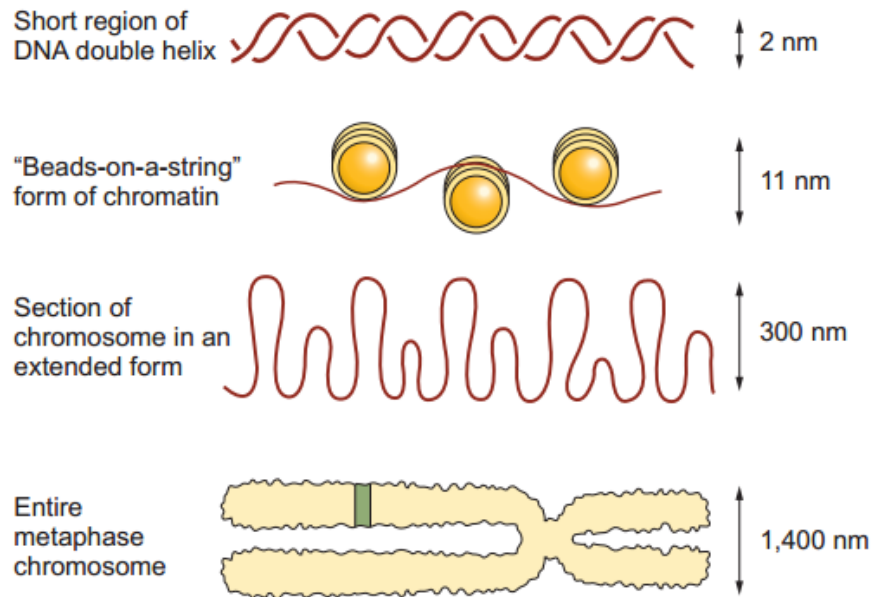


**Figure 1-3:** Schematic of the size ranges and stages of a chromosome adapted from Hall and Giaccia [16]. The DNA double helix structure is depicted along with the nucleosomes (proteins that the DNA wraps around) and a full metaphase chromosome. From Hall and Giaccia (2012) with permission [16].

#### 1.4.2.2. Chromosomal aberrations as a result of ionizing radiation

Following exposure to ionizing radiation, DNA DSBs that are improperly repaired, or not repaired at all, result in chromosome damage known as aberrations [16, 22]. This damage is expressed during metaphase when chromosomes condense. The two aberrations most specific to ionizing radiation are the dicentric and the ring chromosomes.

A dicentric chromosome, shown in Figure 1-4A, occurs when broken ends from two separate chromosomes combine (illegitimate unions) and then replicate. After replication, the result is a chromosome with two centromeres (dicentric) and acentric fragments. The formation of a ring is shown in Figure 1-4B where two broken ends from the same chromosome join together. Replication generates overlapping rings and acentric fragments. These aberrations are important in biological dosimetry as their visualization and quantification allows a direct estimation of radiation dose received.

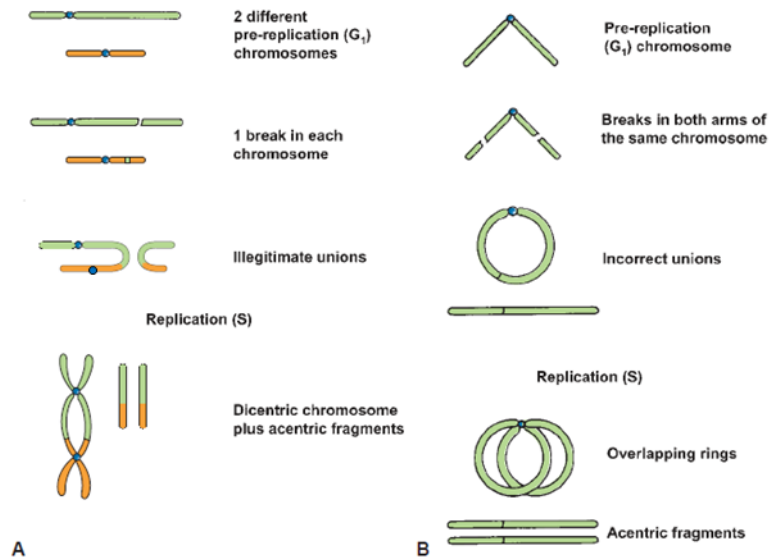


**Figure 1-4:** Illustrations of various chromosome aberrations. **A.** Formation of a dicentric chromosome and acentric fragments. A break in each chromosome and incorrect rejoining of the broken ends results in a dicentric chromosome (two centromeres) and acentric fragments following replication. **B.** Formation of a centric ring and an acentric fragment. Breaks in each arm of a non-replicated chromosome rejoin incorrectly and create rings and acentric fragments following replication. From Hall and Giaccia (2012) with permission [16].

#### 1.4.2.3. Relation between dose and chromosomal aberrations

Figure 1-5 shows a typical dose response curve for chromosomal aberrations in lymphocytes produced by exposure to  $\gamma$  photons from Co-60. The linear component of the curve results from two breaks produced by one event while the quadratic component comes from two breaks caused by two individual events. Therefore, the formation of a chromosomal aberration is based on the probability of interaction that has both linear and quadratic components, and is typically described through the linear quadratic model (LQM):

$$Y = c + \alpha D + \beta D^2 \quad (1-1)$$

where  $Y$  is the number of aberrations per cell as a function of the dose  $D$ ,  $c$  is the background frequency and  $\alpha$  and  $\beta$  are constants corresponding to the linear and quadratic components of the dose respectively. At low doses, the chance of both breaks in a DSB being caused by the same charged particle is high, and thus the probability of an aberration is proportional to dose ( $\alpha D$ ). At higher doses, the two breaks are more likely to be caused by two separate charged particles, and the probability is therefore proportional to the square of the dose ( $\beta D^2$ ). Several biodosimetry assays have been developed to quantify chromosomal aberrations, some of which will be discussed in section 1.5.

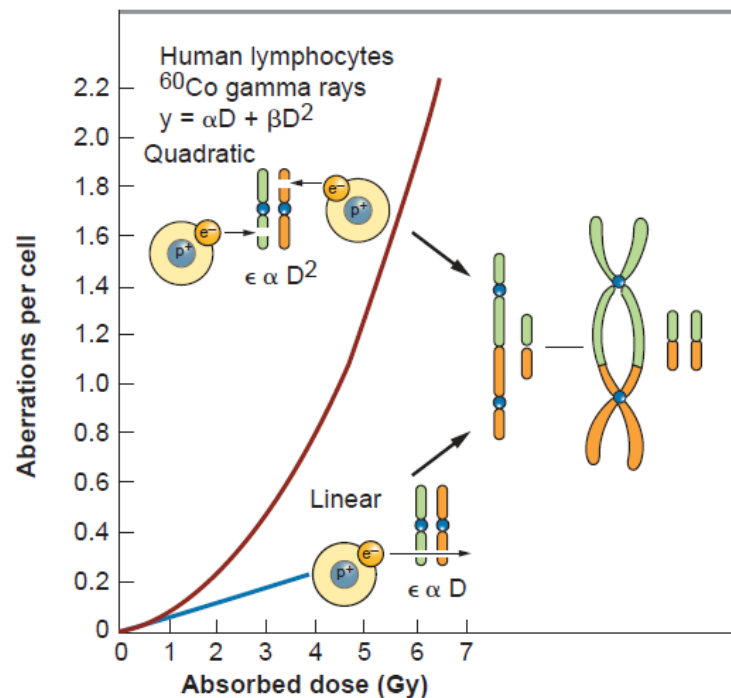


**Figure 1-5:** Frequency of chromosomal aberrations per cell as a function of dose. At low doses, both breaks in a DSB may be caused by the same particle and the probability of an aberration is proportional to dose ( $D$ ). At higher doses both breaks are likely to be caused by two separate particles and the probability of an aberration is proportional to the square of the dose ( $D^2$ ). From Hall and Giaccia (2012) with permission [16].

## **1.5. Biodosimetric assays for the quantification of radiation-induced DNA damage**

Following a radiation accident or mass casualty event, there are a number of biodosimetry assays which can be used to relate radiation-induced chromosomal damage to dose. Sullivan et al. [6] recently reviewed many of the currently available and newly emerging biodosimetric assays. The assays their publication focused on were the Premature Chromosome Condensation (PCC) assay, Lymphocyte Depletion Kinetics assay, Fluorescence In Situ Hybridization (FISH) assay, Gene Expression,  $\gamma$ -H2AX, DCA and the CBMN assay. While all of these assays have applicability in radiation biodosimetry, the two most common are the DCA and the CBMN assay. A brief overview of both of these assays is given below, with a more extensive introduction to the CBMN assay provided in Chapter 2.

### **1.5.1. Dicentric Chromosome Assay**

The Dicentric Chromosome Assay (DCA) is considered to be the gold standard in biological dosimetry. This cytogenetic assay is considered to be highly sensitive to ionizing radiation due to the low levels of spontaneous background dicentric chromosomes in the body (1-2 dicentrics per 1000 cells) [23, 24]. Blood samples are drawn, cultured in a growth medium and stimulated to proliferate through the addition of phytohaemagglutinin (PHA). After 44 h in culture, Colcemid is added to arrest cells in the first metaphase. The cells are left to incubate for another 4 h, then they are processed and dropped on microscope slides to obtain metaphase spreads that are scored by microscopy for the presence of dicentrics. The DCA has a dose range of approximately 0.1-5 Gy [3, 5, 25], but beyond 5 Gy the linear quadratic relation between dose and dicentrics per chromosome breaks down since

higher radiation doses reduce cell proliferation. This leads to fewer cells actually reaching metaphase as damaged cells cycle slower than undamaged cells.

While the DCA is accurate, it is quite time consuming as all scoring must be performed manually, a disadvantage in the event of a mass casualty radiological incident. Attempts have been made to increase the throughput of the DCA by reducing the number of metaphase spreads or dicentric chromosomes that need to be scored [1] or by rapidly (10 s) scanning metaphase spreads for obvious damage (Quickscan) [25, 26]. Additionally, the use of automated metaphase finders to locate spreads and identify dicentric chromosomes has been introduced [27, 28]. Attempts to use conventional flow cytometry (FCM) to identify chromosomes have been made in the past, but the sensitivity of the technique was not sufficient to identify dicentric chromosome or fragments [29, 30]. A more recent attempt to automate the DCA for higher throughput was performed by Beaton et al. who used imaging FCM to successfully identify and score fluorescently stained mono- and dicentric chromosomes [31].

### **1.5.2. CBMN assay**

As mentioned previously, ionizing radiation can produce acentric chromosome fragments. These fragments are broken pieces of DNA which lack centromeres and therefore are unable to be pulled into new daughter cells. Thus, they remain in the cytoplasm following mitosis and form into small, individual nuclei known as micronuclei (MN). MN can also be generated from whole chromosome pieces containing centromeres that get left behind at anaphase as a result of damage to the spindle or kinetochore apparatus [32-34]. The standard procedure for measuring MN in lymphocytes is as follows: blood samples are drawn, placed into culture and stimulated to proliferate by PHA. At 44 h following initial culture, the addition of Cytochalasin B (Cyt-B) arrests cells after

nuclear division but before division into two new individual daughter cells (cytokinesis) can take place resulting in cells with two nuclei (binucleated). At 72 h after initial culture, cells are processed, fixed, stained and samples are dropped on slides for scoring of the number of MN contained within binucleated cells (BNCs) [35]. It is advantageous to score BNCs since these cells have completed one and only one nuclear division, and MN in these cells can be specifically and efficiently scored while excluding non-dividing mononuclear cells that are unable to express MN. Therefore, the cytokinesis-block MN (CBMN) assay is the standard method for enumerating MN in cultured lymphocytes [5].

The CBMN assay is not strictly specific to ionizing radiation as MN can be formed in a variety of other ways such as through exposure to environmental chemicals that can cause chromosome breaks (clastogenic agents) [36], mutations in kinetochore proteins (structures on chromatids where spindle fibers attach during mitosis) [34], smoking and age [36]. All of these factors lead to an increase in background MN, making the CBMN assay less specific to ionizing radiation than the DCA at lower doses with a dose range of approximately 0.3 – 5 Gy [5, 37]. In a recent publication, Tucker et al. [38] analyzed CBMN assay data on 3104 individuals between 0 – 88 years of age to assess the lowest detectable dose of ionizing radiation. For males and females in their 20's, the minimum detectable dose was found to be 0.18 Gy and 0.20 Gy respectively. For males and females in their 50's the minimum detectable doses were 0.23 Gy and 0.25 Gy respectively, and for males and females in their 70's the doses were 0.24 Gy and 0.26 Gy respectively. The CBMN assay also suffers from the same complications as the DCA above 5 Gy as the reduction of cells proceeding through to cytokinesis at such high doses hinders the effectiveness of the assay since damaged cells cycle slower than undamaged cells.

Like the DCA, the CBMN assay is an accurate estimator of dose, but can be time consuming when scored by manual microscopy. Attempts have been made to increase

the throughput of the CBMN assay for triage biodosimetry by counting fewer BNCs than the traditional 500 or 1000 and McNamee et al. showed that doses of greater than 1 Gy were detectable by counting only 200 BNCs, which took 15 min [35]. Recently, automated slide scoring systems such as the Metafer 4 software (MetaSystems) coupled to a fluorescent microscope have been used to automatically detect BNCs and MN, thereby increasing throughput and eliminating scorer variability. Varga et al. established an automated scoring procedure in which slides can be scored in 7 min though a significant decrease in the proportion of MN per BNC scored was observed when compared to manual scoring [39]. Willems et al. used the technique to correctly identify doses up to 3 Gy with an uncertainty of 0.2 Gy and estimated that 60 samples can be scored by two technicians in a 12 h period [37].

## **1.6. Flow cytometry**

Flow cytometry (FCM) is a method for the rapid measurement of optical and fluorescent characteristics of single cells. A wide variety of cell properties such as specific populations, cell surface receptors, nucleic acid concentration and enzymatic activity can be quantified by labelling (attaching) fluorescent compounds (probes) to specific structures including proteins and nucleic acids [40]. The labelled cells are then placed in suspension and drawn into a stream of laminar flowing fluid inside the flow cytometer, allowing them to pass single file through an interrogation point. At this interrogation point, a set of lasers orthogonally intersect the cells, and the resulting scattered fluorescent photons are filtered and collected by a series of optical elements [41].

### 1.6.1. Traditional FCM

A traditional flow cytometer consists of three main systems: fluidics, optics and electronics. The fluidics system transports cells single-file through the interrogation point. The optics system consists of lasers or light emitting diodes (LEDs) to illuminate fluorescent dyes that have been added to the cells and optical filters direct the fluorescent signals to the appropriate detectors [40]. When a sample of cells in solution is introduced into the flow cytometer, the cells are hydrodynamically focused in a stream of sheath fluid as seen in Figure 1-6. This focusing allows the cells to pass single-file through the interrogation point inside the flow cell.

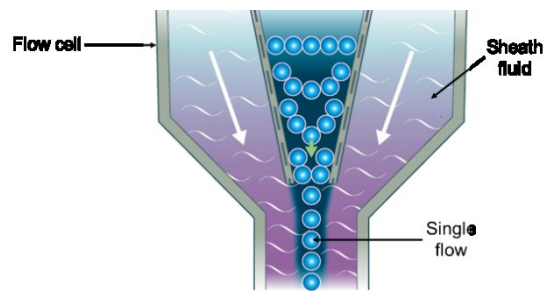


**Figure 1-6:** Hydrodynamic focusing produces a single-file stream of cells inside the flow cell of the cytometer. From Rahman (2006) with permission [40].

Focused cells pass through one or more monochromatic lasers orthogonally directed at the bottom of the flow cell; this is the interrogation point. If the cells are labeled with a fluorochrome, photons of a specific wavelength will be emitted isotropically upon excitation. Forward scattered (FSC) photons and side scattered (SSC) photons provide information on cell size and cell granularity respectively. Photons emitted from the fluorochromes are collected and separated into individual fluorescence channels and detected by photomultiplier tubes (PMTs) and specificity of detection is controlled by optical filters (long pass, short pass and/or band pass). Dichroic filters placed on a 45°

angle to the emitted photons allow transmission and 90° deflection of photons (depending on wavelength) (Figure 1-7). When multiple fluorochromes are used in an experiment, spectral overlap between channels (including auto-fluorescence) is a possibility but can be corrected by fluorescence compensation. Compensation calculates (as a %) the amount of interference a fluorochrome has in a channel that was not assigned to measure it and then removes this interference [40]. The logistics of a typical flow cytometer system are shown in Figure 1-7. Characteristics from the scattered fluorescent photons are then used to generate scatter plots that can differentiate between features of multiple populations in a sample, or histograms to evaluate the frequency of a particular cell characteristic as shown in Figure 1-8 [40, 41].

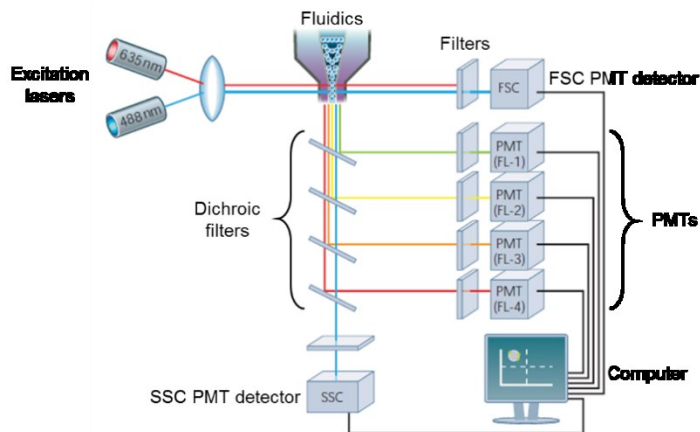


**Figure 1-7:** Schematic of a typical flow cytometer setup adapted from Rahman (with permission) [40]. The intersection of the excitation lasers with the fluidics system is shown, as well as the geometrical configuration of the filters and PMTs.

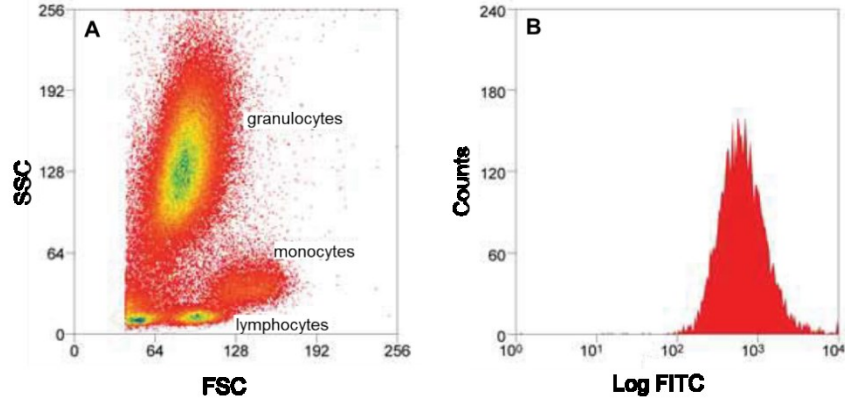


**Figure 1-8:** A typical dot plot and histogram generated from FCM data adapted from Rahman (with permission) [40]. **A.** Intensity of forward scatter (FSC) versus side scatter (SSC) of cells in a blood sample. Clusters represent various cell types as labelled (granulocytes, monocytes and lymphocytes). **B.** Histogram of the fluorescein isothiocyanate (FITC) fluorochrome detected in the sample.

### 1.6.2. Imaging FCM

Imaging FCM combines all of the aspects of traditional FCM, and adds the imaging capabilities of fluorescent microscopy. The ImageStream<sup>x</sup> (ISX) developed by EMD-Millipore (Billerica, MA) possesses the ability to both pass cells through the flow cell at a very high rate (several thousand cells per second) and to acquire images of all individual cells passing through the interrogation point. The Image Data Exploration and Analysis Software (IDEAS®) analysis program coupled with the ISX allows for qualitative measurements of size, shape, texture, intensity and many other characteristics of all images in a dataset [42].

A more in-depth overview of the ISX, including sample preparation requirements, optics and detection systems, data collection procedures and analysis software, is provided in Chapter 2.

## **1.7. Thesis statement**

### **1.7.1. Thesis statement**

The hypothesis of this thesis is that the CBMN assay can be performed on an imaging flow cytometer in such a way as to provide rapid, high throughput dose estimations with adequate sensitivity for use in triage radiation biodosimetry following a mass casualty radiological event. The thesis consists of three separate studies that investigated the feasibility of performing the CBMN assay on an imaging flow cytometer, the optimization and expansion towards a multi-parameter dose estimation methodology for biodosimetry and finally, the testing of reductions in culture time and volume to improve the throughput and applicability of the CBMN assay in a mass casualty event.

The first study consisted of adapting and automating the CBMN assay for use on the ISX, as a novel method of automated biodosimetry. Modification of the widely accepted sample preparation method for microscope-based CBMN for adaptation on the ISX was performed and a data analysis template for identifying MN and BNCs was developed.

The second study involved optimization of the automated analysis method developed in the IDEAS® software, as well as the development of a multi-parameter method for dose estimations in radiation biodosimetry. The feasibility of using the percentage of mononuclear cells (MNCs) and the replication index (RI) in combination with the rate of MN per BNC to estimate blinded doses was investigated.

The third study involved validating the assay by generating dose estimations from irradiated, blinded samples. Additionally, reductions in whole blood culture time and volume were investigated in an attempt to decrease the overall time required to perform the assay, therefore making this imaging flow cytometry version of the CBMN assay more applicable in high throughput triage radiation biodosimetry.

### **1.7.2. Thesis outline**

This thesis details the work performed to adapt the CBMN assay to a new imaging flow cytometry method to provide rapid and accurate dose estimations for use in triage radiation biodosimetry following a mass casualty radiological event. Chapter 2 provides background on the CBMN assay and its application in radiation biodosimetry. The principles of imaging flow cytometry and the components of the ISX imaging flow cytometer are also described. Chapter 3 describes the new laboratory protocol developed to perform the CBMN assay on the ISX as well as proof of concept dose calibration curves which correlate the rate of MN per BNC to dose. A multi-parameter dose estimation method which investigates the possibility of providing dose estimations up to 10 Gy by using the percentage of MNCs and the RI as complementary parameters of measure in addition to the rate of MN per BNC was developed and is described in Chapter 4. Chapter 5 describes the procedures performed to test and validate the newly adapted ISX-CBMN method by performing dose estimations on blinded samples using standard culture time and volume conditions. Furthermore, the ability of the method to provide accurate dose estimations with reduced culture time and/or volume is also investigated. Finally, a summary of the thesis findings, future research project ideas and concluding remarks are presented in Chapter 6.

### **1.7.3. Ethical considerations**

All studies in this thesis were approved by the Research Ethics Board of Health Canada. The anonymity of donors was maintained during the study and information about individual characteristics (i.e. sex and age) was only provided following completion of the data analysis.

## **2. BACKGROUND INFORMATION ON THE CBMN ASSAY FOR RADIATION BIODOSIMETRY AND IMAGING FCM**

### **2.1. The traditional CBMN assay in radiation biodosimetry**

The micronucleus (MN) test was first described by Schmid in 1975 [43] as a method to quantify chromosome fragments that remain in the cytoplasm after the cell divides. These fragments are much smaller than the principle nucleus and typically form into MN following the completion of at least one full mitosis. The original peripheral blood lymphocyte (PBL) MN assay was described by Countryman and Heddle in 1976, who scored MN in a number of irradiated PBL samples, but the assay lacked a method of determining whether the cells had actually completed one mitosis [44]. In 1985, Fenech and Morley [32, 33] were able to quantify the number of MN inside the cytoplasm of cells that had indeed undergone one mitosis through addition of the chemical Cyt-B. Cyt-B is a cell permeable cytotoxic compound that blocks the formation of actin filaments inside the cell that aid in cell division and therefore prevents cytokinesis, the final stage of cell division [45]. The resulting assay became known as the Cytokinesis-Block Micronucleus assay which is now the standard method for measuring MN in cultured lymphocytes. Since MN can also be generated following interactions between chromosomes and ionizing radiation, this assay has subsequently been adapted as a biodosimeter of radiation exposure.

#### **2.1.1. Whole blood culture**

The typical blood cell culture method for the CBMN assay involves drawing a venous blood sample into a tube containing lithium heparin anticoagulant. Cultures are then prepared by adding one part whole blood to nine parts of a culture medium. The culture

medium consists of Roswell Park Memorial Institute (RPMI) 1640 medium, fetal bovine serum (FBS), L-glutamine (a standard amino acid), penicillin and streptomycin (antibiotics to prevent cell infection) and PHA. RPMI is a bicarbonate buffering system composed of inorganic salts, amino acids and vitamins that support the growth of cells in culture [46]. FBS comes from blood drawn from a bovine fetus and is a widely used serum in cell culture due to it having a very low level of antibodies and containing many cell growth factors. PHA is a carbohydrate-binding protein that triggers cell division in lymphocytes [32].

Cell cultures are incubated for a period of 72 h. Cyt-B is added to the cultures at either 24 h or 44 h. 44 h is the preferred Cyt-B addition time for many toxicology-based CBMN applications as this ensures that most cells will have passed through at least one mitosis. However, for radiation biodosimetry, adding Cyt-B after 24 h is preferable to capture cells that have only completed one nuclear division [5, 47].

### **2.1.2. Culture processing and slide preparation**

The standard method of culture processing varies slightly between laboratories but typically, cell suspensions are centrifuged, the supernatant is removed and the cell pellets are resuspended in a hypotonic potassium chloride (KCl) solution that causes the cells to swell. A methanol:acetic acid solution is then added to terminate any ongoing biological processes, hence “fixing” the cells in their current state. The fixed cells are then re-suspended in a small volume of the methanol:acetic acid solution to achieve a desired cell concentration for slide preparation. Cell suspensions are then dropped onto glass slides and dried for 24 h. Finally, slides are stained with a DNA stain such as acridine orange fluorescent dye. Acridine orange strongly binds to components in the DNA and weakly to components in the cytoplasm. When cells stained with acridine orange are excited by blue light from a fluorescent microscope, green photons (525 nm) are emitted from the DNA

and orange photons are emitted from the cytoplasm (Figure 2-1B and Figure 2-1C) [35, 48].

### 2.1.3. Scoring the slides

Figure 2-1 illustrates the process of BNC formation with MN inside the cytoplasm as well as an acridine orange-stained BNC, and a BNC with one MN [47, 48].

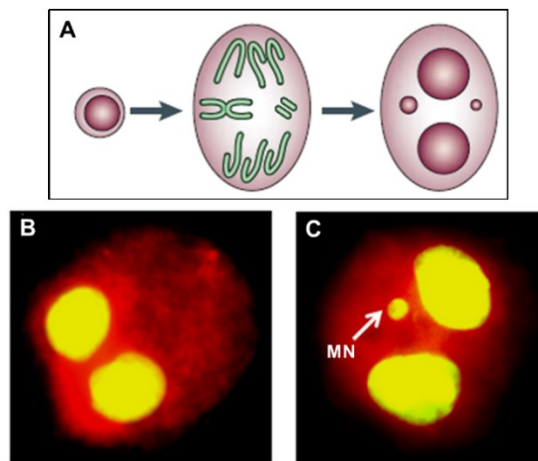


**Figure 2-1:** BNC/MN formation and acridine orange-stained cells. **A.** MN generation from acentric fragments lagging behind at anaphase [47]. From Fenech (2007) with permission. **B.** Acridine orange-stained BNC showing the cytoplasm in orange and the nuclei in yellow. **C.** Acridine orange-stained BNC with the two main nuclei and one MN in yellow [48]. From Lim (2012) with permission.

In 2003, a detailed publication by Fenech et al. outlined the criteria for properly scoring BNCs and MN [49]. A BNC should have two distinct individual nuclei within a clear, intact cytoplasm with the two nuclei being approximately equal in size, staining pattern and intensity (Figure 2-1B). If the two nuclei are overlapping, the cell may only be scored as a BNC if the boundaries of each nucleus are distinguishable. For a MN to be scorable it must be round or oval in shape, not linked or connected to the nuclei, have its own distinguishable boundary and have roughly the same staining intensity as the main nuclei (Figure 2-1C). Additionally, a MN should have a diameter of approximately 1/256 to 1/9 of one of the main nuclei, though this parameter is rather subjective with manual scoring

methods. Typically, a total of 1000 BNCs are scored per sample [49]. Following exposure to ionizing radiation, virtually all somatic cells experience a delay in the G<sub>2</sub> phase of the cell cycle that halts progression into mitosis and results in reduced proliferation. At very high radiation doses (above 5 Gy), delays in the S phase are also observed with an even greater reduction in proliferation [50]. Müller and Rode [51] have shown that the frequency of MNCs increases from approximately 50% to 100% between 5-15 Gy and that the quantification of MNCs could offer the possibility to accurately quantify doses beyond 5 Gy. It should be noted that the MNC frequency depends on culture conditions and therefore, standardization of these conditions is essential for proper quantification of this parameter in radiation biodosimetry. The CBMN assay has been applied extensively in radiation dosimetry using both manual and more recently, automated slide scoring methods. In addition, robotic and FCM methods have been developed with varying degrees of success. These applications will be discussed below.

#### **2.1.4. Manual scoring methods**

The CBMN assay has been used to provide biodosimetric information in many studies including monitoring of hospital workers occupationally exposed to ionizing radiation, and to estimate doses to individuals who were exposed during accidents. It has also been adapted for use in the case of a mass casualty radiological event.

Hospital workers occupationally exposed to radiation were studied using the CBMN assay and overall, a higher frequency of MN was noted when compared to control populations. In 2000, Thierens et al. [52] performed the CBMN assay on 71 individuals (35 males and 36 females) working as doctors, nurses or technicians involved in interventional radiology procedures. When compared to a control group of 60 individuals (23 males and 37 females) not occupationally exposed, a statistically significant increase

in MN was observed. Similar trends were observed in studies of overexposed hospital workers by Bigatti et al. [53], Jha and Sharma [54], and Barquinero et al. [55]. Both Liu et al. [56] and Thierens et al. [57] compared the effectiveness of the standard CBMN assay to the DCA for estimating doses to individuals who were accidentally exposed to ionizing radiation. Both studies revealed a satisfactory agreement between the two methods, indicating that the CBMN assay may be used for the purposes of triage in cases of accidental overexposure where the dose must be estimated quickly.

In the case of a mass casualty event, it would be necessary to reduce the time required to perform the CBMN assay. One proposed strategy is to reduce the total number of BNCs scored. In 2001, Voisin et al. reduced the number of BNCs scored 1000 to 500 in order to provide a dose estimation and showed good agreement when compared to the results of the DCA [58]. In 2009, McNamee et al. further reduced the number of BNCs scored to 200 in an attempt to increase the throughput of the assay [35]. It was determined that among three independent laboratories, doses of greater than 1 Gy could be identified when only 200 BNCs were scored.

While the CBMN assay does provide higher throughput than the DCA, manual scoring is still time consuming and introduces uncertainties in the dose estimations as a result of scorer variability, hence the need for an automated method.

#### **2.1.5. Automated scoring methods**

The framework for automating the CBMN assay began in the early 1990's. In 1993, Castelain et al. generated an algorithm based on a sequence of greyscale and binary operators to score MN on Giemsa stained slides [59]. In 1994, Verhaegen et al. developed a similar algorithm using binary images developed from Giemsa stained slides, along with a combination of low and high magnification images to automatically detect MN [60]. A

number of other works have been presented on automating the CBMN assay for occupational and triage biodosimetry using both slide counting and cytometry methods and are discussed below.

#### **2.1.5.1. Slide-based scoring using Metafer MNScore and IMSTAR Pathfinder™ software**

Most methods that currently exist to automatically score MN are based on slide-scoring using the MNScore software module integrated in the metaphase finder of the Metafer (MetaSystems, Germany) slide scanning platform. Varga et al. [39] described a method in which slides are fluorescently stained with 4',6-diamidino-2-phenylindole (DAPI) and then a number of classifiers, such as cell area and symmetry, are applied to automatically count BNCs and MN. Using 73 donors (27 with breast cancer and 46 controls) the authors showed that the automated slide scoring technique generated highly reproducible results when compared to manual scoring. However, the number of MN scored using the automated technique was considerably lower (by a factor of approximately 3) than the number of MN scored manually. Schunck et al. [61] performed similar automated slide scoring of the CBMN assay using blood from 4 donors irradiated to 1, 2 and 4 Gy, and noted a linear quadratic relation between dose and rate of MN per 1000 BNCs, as expected. They also reported a reduction in the number of MN counted with values similar to those of Varga et al. The explanation offered by the authors for this phenomenon is that the stricter scoring parameters in image analysis may cause some MN that would be scored by visual inspection to be missed using automated scoring. Two examples of this are failure of the automated system to count MN that are in contact with the nuclei and nuclei that are too small for the threshold size parameters set in scoring software.

In 2010, Willems et al. used the Metafer system to develop a rapid CBMN triage method to be used following a large-scale radiation accident [37]. Their results showed that while calibration curves for both automated MN and manual MN both show a linear quadratic dependence, the number of number of MN scored automatically is lower by a factor of 2 when compared to manual scoring at a dose of 3 Gy, consistent with the findings of both Varga et al. [39] and Schunk et al. [61]. Despite this, their method was able to generate dose estimations to within 0.2 Gy of the delivered dose when scoring blinded samples and they have estimated that their method could allow for the processing of approximately 60 samples in a 12 h period. In 2014, De Amicis et al. [62] and De Sanctis [63] used a similar automated slide-scoring method to generate calibration curves and also reported that the number of MN scored at 3 Gy is lower by a factor of 2, similar to the observations of Willems et al., [37] Varga et al. [39] and Schunk et al. [61]. Still, dose estimations were generated to within 0.3 Gy (or less) of the delivered dose for a number of blinded samples between 0-4 Gy after 8 min of slide scoring time [62, 63]. The results of these works indicate that accurate dose estimations can be generated even with shallower dose response calibration curves. However, the reduction in the number of MN in these calibration curves increased the uncertainty and therefore decreased the overall precision of these dose estimations.

A further advancement in automating the CBMN assay has been the Rapid Automated Biodosimetry Tool (RABiT), developed at Columbia University [64-66]. It has been suggested that the RABiT can be used to perform the CBMN assay for radiation biodosimetry using only a fingerstab of blood (50  $\mu$ L). All processes following blood sample collection are automated through the use of multi-well plates and robotics to culture, incubate, process and score cells for biodosimetry. The authors claim that the system, in combination with high speed image analysis of slides, can currently analyze 6000 samples

per day, with development in place to reach an ultimate throughput of 30,000 samples per day [65]. While dose response calibration curves that follow a linear quadratic relation up to 4 Gy have been generated using the system, the number of BNCs scored in their generation was an order of magnitude lower than the number of BNCs scored to generate similar curves in the works mentioned previously [66].

The IMSTAR Pathfinder™ Screentox Auto-MN system for automated scoring of MN in the CBMN assay was developed as part of the European Union Framework Programme NewGeneris to explore the risks of the development of cancer during childhood as a result of *in utero* and maternal exposure to genotoxic compounds [67]. The Pathfinder™ system detects the cytoplasm in each individual cell then examines the morphological characteristics of MN and nuclei within those cells. This enables scoring of the MN frequency in mono-, bi- or multi-nucleated cells and estimation of the cytokinesis-block proliferation index. Digital filters are then applied to correct for intra-cytoplasm staining variations, non-homogenous background levels as well as nuclei and MN staining variations as well as to separate touching and overlapping cells. Visual verification of five automated image capturing sessions was performed and high correlations to the results of visual scoring were observed. Absolute MN frequencies obtained through automated scoring were found to be lower than those obtained by manual scoring, but a clear dose response was observed with the automated system [67-69]. In the context of the NewGeneris project, MN scoring data was obtained for a cohort in Crete and higher levels of MN in BNCs as well as a higher proliferation index were observed in peripheral blood lymphocytes of mothers compared to lymphocytes from cord blood of newborns [70]. These results indicated the importance of examining both mono- and bi-nucleated T-lymphocytes for biomonitoring of newborns [71].

All of the aforementioned automated CBMN methods are based on slide-scoring that can be time consuming as slides must be prepared under proper temperature and humidity conditions that are often difficult to control. In addition, current slide staining techniques can be subject to some variability and may produce slides that have non-uniformly stained BNCs and MN, causing them to be missed by the scoring software. FCM may offer an advantage as microscope slides are not used, and the staining procedures are based on dye concentrations directly related to the cell count in each sample.

#### **2.1.5.2. Automated scoring using FCM methods**

As early as 1984, attempts have been made to adapt the CBMN assay to traditional FCM [72]. Schreiber et al. and Nüsse and Marx developed an elegant FCM method based on ethidium bromide fluorescence and forward and side scatter intensities to differentiate between debris and lysed nuclei and MN [73, 74]. This method was limited by an inflated MN frequency since MN could not be distinguished from debris or dead/dying cells. In recent years, these methods have been built upon in several studies attempting to distinguish true MN from apoptotic chromatin in mouse lymphoblastoids [75] and human TK6 cells [76]. While these modifications did improve the sensitivity of the assay, making the distinction between MN and free chromosomes was still not possible. While traditional FCM can increase the throughput of the CBMN assay, the one major drawback is that cells require lysing prior to analysis to release nuclei and MN. This eliminates the ability to apply the analysis to biodosimetry since it is imperative to control the number of times a cell has passed through mitosis in order to correlate the number of MN per BNC to dose and as such, cells should not be lysed.

## 2.2. Imaging FCM on the ImageStream<sup>X</sup>

The ISX is an imaging FCM system capable of analyzing large numbers of cells in suspension, capturing high resolution photographs of fluorescently stained individual cells at a rate of several hundred or thousand cells per second [42]. The sections below present a brief overview of the ISX system.

### 2.2.1. Overview

The ISX shown in Figure 2-2: is a bench top imaging flow cytometer designed to acquire 12 channels of cellular imagery. The system combines the speed of traditional FCM with the ability to take high resolution photographs of fluorescently labelled cells using a charge-coupled device (CCD) camera. The ISX is completely controlled by the INSPIRE software that is integrated into the machine, with data analysis performed separately in the IDEAS® software [77].



**Figure 2-2:** The ISX along with a screenshot of the INSPIRE software used to control the instrument. From Amnis INSPIRE User's Manual (2010) with permission [77].

### 2.2.2. Illumination, optics and image collection

Figure 2-3 illustrates the optics of the ISX. Up to six images can be acquired simultaneously from the same cell including brightfield (BF) and multiple fluorescent images. Cells are passed through the flow cell using hydrodynamic focusing (described in section 1.6.1) and are simultaneously interrogated orthogonally by a BF source and one or more lasers. The fluorescently scattered light is magnified by one of three objective lenses (20x, 40x or 60x), collected through a series of lenses and filters, and directed towards a dichroic filter stack that decomposes the spectrum, emitting light of different wavelength ranges at different angles. This light then impinges on different channels of the CCD (256 pixels per row) allowing for multiple images to be collected simultaneously. The ISX is equipped with autofocus and velocity detection systems to ensure that images remain focused during acquisition even if the cell flow speed varies.

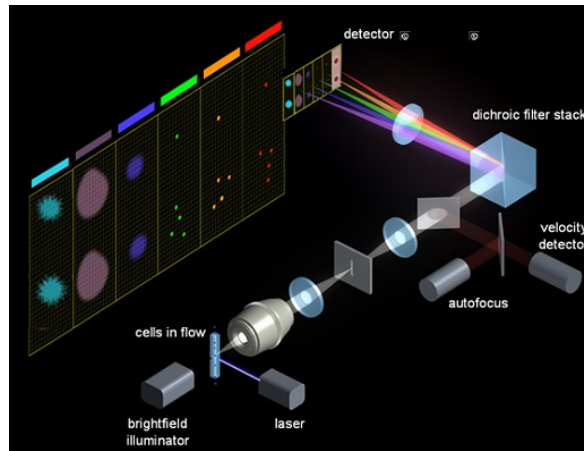


**Figure 2-3:** Optics and illumination of the ISX. Focused cells are orthogonally interrogated with one or more lasers, fluorescently scattered light is focused and filtered through the use of lenses and mirrors, then directed towards a CCD camera where images are captured. From Amnis INSPIRE User's Manual (2010) with permission [77].

The CCD operates in time delay integration (TDI) mode whereby objects captured in one row of pixels are transferred to another row on the CCD in synchrony with the velocity of the cells. Images are created by compiling all rows of pixels that allows for the generation

of focused, high quality images free of streaking even at high cell velocities. BF illumination is accomplished with a LED that illuminates the flow cell orthogonally. Fluorescence excitation is achieved through variable power lasers at 405 nm (10-125 mW), 488 nm (10-100 mW) and 658 nm (10-120 mW).

### 2.2.3. IDEAS® (Image Data Exploration and Analysis Software) for the ISX

The Image Data Exploration and Analysis Software (IDEAS®) is designed specifically to analyze output data from the ISX [78].

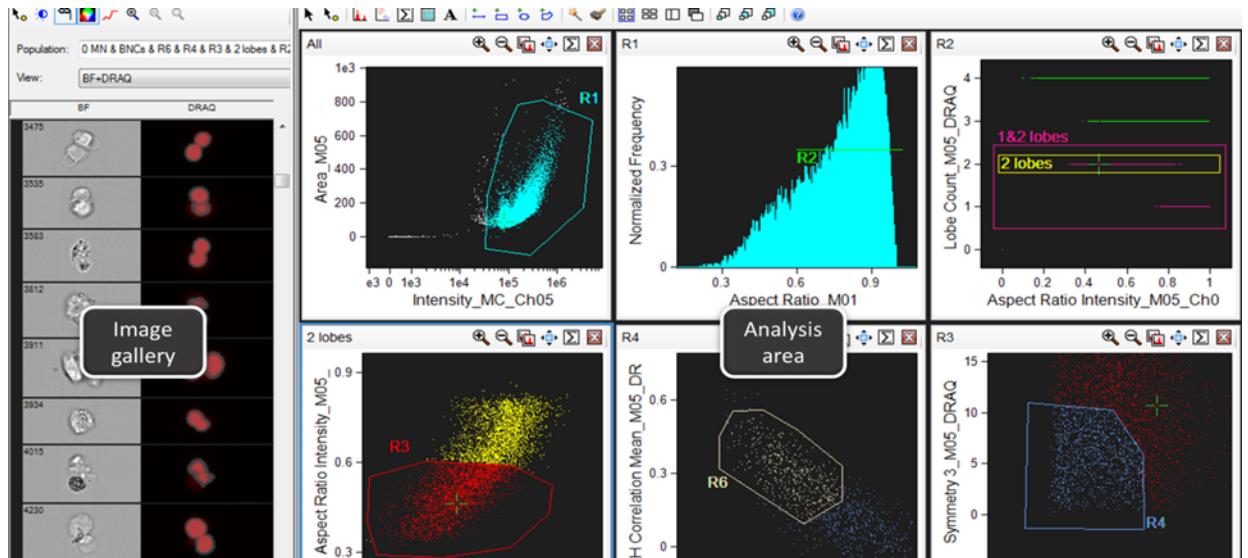
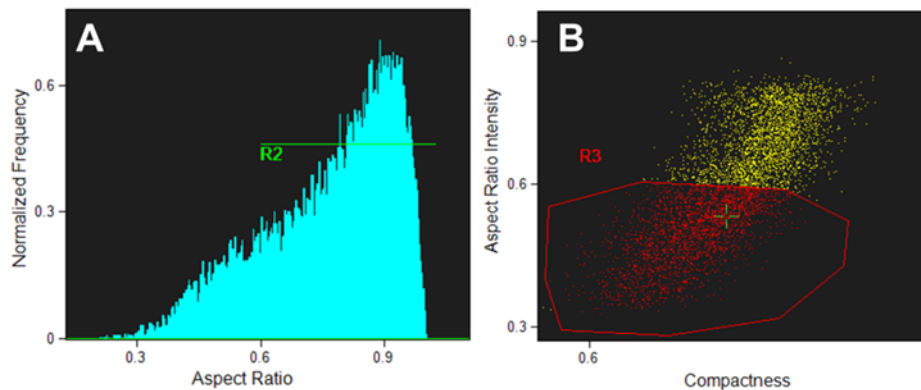


**Figure 2-4:** Screenshot of the layout of the IDEAS® software. The left side shows the cell image gallery and the right side shows the analysis area, where dot plots, histograms and statistics tables can be generated and displayed.

IDEAS® provides an image gallery in which every cell in each data file can be individually viewed and analyzed. The IDEAS® application window is divided into two panels – the image gallery and the analysis area (Figure 2-4). In the analysis area, various panels can be created for any cell population based features such as size, shape, texture and signal strength. A single feature can be viewed by creating a histogram or a combination of any

two features can be viewed on a scatter plots. Gates (linear, square, circular or polygonal) can be placed around any group of cells (or population) within the panel to highlight populations of interest and ignore undesired populations. The image gallery can display all individual cell images or images of all cells in a population within a gate. Additionally, the gallery can display BF images, fluorescent images and masks from every channel simultaneously and in any order the user desires.

Composite images can also be created such that information from two or more channels (e.g. BF and fluorescence) can be viewed as one image.



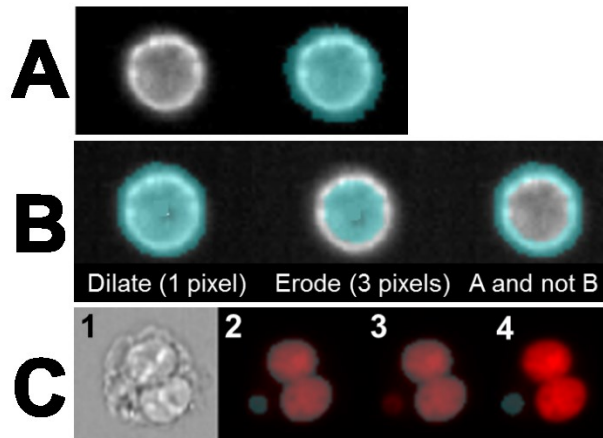
**Figure 2-5:** Plots generated in the analysis area of the IDEAS® software. **A.** Histogram created using the aspect ratio feature with a linear gate (R2). **B.** Dot plot created using the aspect ratio intensity and compactness features with a polygonal gate (R3).

Figure 2-5A shows a histogram created using the aspect ratio feature with a linear gate (R2) to highlight a desired subset of cells within the plotted population. Figure 2-5B shows a dot plot created using the aspect ratio intensity and compactness features with a polygonal gate (R3). Individual cells of interest can then be selected (green crosshairs) and set as the active event in the image gallery.

To assist with analysis, cells of interest as well as events to be ignored can be selected ('tagged') in IDEAS® such that they can be used as reference populations to

determine the feature(s) that best differentiate them. The “find best feature” option uses the desired and undesired populations as a reference to determine which features in the software best statistically separate them based on a variety of characteristics such as size (area, width, etc.), shape (aspect ratio, compactness, etc.), texture (contrast, spot count, etc.) and signal strength (intensity, mean pixel, etc.). Dot plots can then be created using these features to separate the desired events from the undesired events in the entire data set.

Once the undesired events have been gated out of a population, it is possible to identify more specific characteristics in the desired population using masks. Masks superficially highlight a set of pixels in a specified region of interest. Figure 2-6 demonstrates the use of various masks in the IDEAS® software. Figure 2-6A shows a cell represented by the greyscale image (left) and the mask used to highlight the cell represented by the superficial cyan colouring (right). Figure 2-6B illustrates the use of mask combinations to create a cytoplasm mask. A dilate mask (left) and an erode mask (center) have been created separately using the same image and are then combined using the ‘and not’ Boolean logic functions (right), leaving only the outer shell of the cell highlighted. Figure 2-6C illustrates the use of the spot masking in combination with Boolean logic to highlight MN. Spot masking is used to highlight both the main nuclei and the MN (Figure 2-6C2). Boolean logic is then used to display the main nuclei and the MN separately (Figure 2-6C3 and Figure 2-6C4) such that they can be counted.



**Figure 2-6:** Illustrations of the use of various masks in the IDEAS® software. **A.** A cell image (left) and a cyan coloured mask highlighting the cell (right). **B.** Creation of a cell cytoplasm mask using both the dilate and erode masks and then combining them using Boolean logic. **C.** A BNC with one MN (**C1**) where spot masking is used to highlight the two main nuclei and the MN (**C2**). Boolean logic is then applied to display the highlighted main nuclei (**C3**) and MN (**C4**) separately for scoring. Panels A and B from Amnis IDEAS® User's Manual (2010) with permission [78].

Once a complete analysis template has been created using histograms, dot plots, masking and any other options that are desired, as shown in Figure 2-4, the template can be saved and applied to any population that is collected with the ISX. This ensures that all populations are analyzed in the same fashion with no user intervention required.

### **3. AUTOMATED ANALYSIS OF THE CYTOKINESIS-BLOCK MICRONUCLEUS ASSAY FOR RADIATION BIODOSIMETRY USING IMAGING FLOW CYTOMETRY**

#### **3.1. Summary**

This chapter is based on the publication titled *Automated analysis of the cytokinesis-block micronucleus assay for radiation biodosimetry using imaging flow cytometry* published in the journal of Radiation and Environmental Biophysics (53(2), 273-282, 2014) [79]. This study investigated the feasibility of adapting the CBMN assay to an imaging FCM method using whole blood from healthy, anonymous donors. A fully automated method to perform and analyze the CBMN assay on the ISX was developed, and indicate that binucleated cells and MN can be identified, imaged and enumerated automatically by imaging flow cytometry.

For clarity and completeness, additional sections have been included within this chapter that detail the procedure used for DNA staining, the results of investigating the use of cell surface and cytoplasm markers and the results of dose calibration curves generated between 0-1 Gy to examine the sensitivity of the method in its current form.

#### **3.2. Introduction**

The CBMN assay [35, 36] is a proven dosimetric technique that is robust and sensitive enough to provide accurate biological dose estimates. Historically, the method is performed by manual slide scoring and is labour-intensive, time-consuming and subject to variability of interpretation between scorers. The assay gives accurate dose estimations but is not able to be performed quickly enough to be useful following a mass casualty radiation event in which the dose to hundreds or thousands of casualties may need to be

determined. As such, several methods of automating the assay have been developed recently as described in section 2.1.5.

This chapter introduces a new automated method developed in our laboratory to perform the CBMN assay on the ISX imaging flow cytometry system for the purposes of radiation biodosimetry. The ISX combines the high-throughput advantages of traditional flow cytometry with the image analysis methods of standard microscopy-based methods. Modifications to existing standard protocols, procedures used for DNA staining as well as specific data collection and analysis parameters are discussed.

### **3.3. Materials and methods**

#### **3.3.1. Blood collection and irradiation**

For the CBMN assay, peripheral blood was collected from four healthy anonymous donors in two 10 mL and one 4 mL lithium-heparinized Vacutainer® tubes (BD Biosciences, Mississauga, ON). All donors were non-smokers between the ages of 20 and 60 years and in relatively good health at the time of blood donation. Each sample was divided into 2.5-mL aliquots and irradiated at 0, 1, 2, 3, 4, 5, 6 and 7 Gy. Irradiation was performed using a cabinet X-ray machine (X-RAD 320, Precision X-Ray Inc., North Branford, CT, USA) at 250 kVp and 12.5 mA with a 2 mm Al filter. Each tube of blood was inserted on its side into the middle of 9 cm of water-equivalent build-up material resulting in a dose rate of 1.3 Gy/min calibrated using a UNIDOS PTW TW30010-10 ion chamber and T10002 electrometer (Freiburg, Germany) calibrated at the National Research Council, Ottawa, ON ( $N_k = 48.3 \text{ mGy/nC}$  at 250 kV, assuming air kerma to be equal to dose).

### **3.3.2. Blood collection and irradiation for 0-1 Gy calibration curves**

To generate calibration curves from 0-1 Gy, peripheral blood was collected from health anonymous donors and irradiated at 0, 0.25, 0.5, 0.75 and 1 Gy using the same conditions described in section 3.3.1.

### **3.3.3. CBMN assay**

The CBMN assay was modified from the standard procedure of Fenech and Morley [32] to allow for the analysis on the ISX (EMD-Millipore, Billerica, MA, USA) imaging flow cytometer. Whole blood samples were diluted 1:9 with RPMI 1640 culture medium containing 10% fetal bovine serum, 2 mmol L-glutamine, 100 U/mL penicillin, 100 µg/mL streptomycin (Sigma-Aldrich, Oakville, ON) and 1% phytohaemagglutinin (PHA) (Life Technologies, Burlington, ON) to achieve 20 mL cultures in 25 cm<sup>2</sup> vented flasks. The cultures were incubated (37 °C, 5% CO<sub>2</sub> for 24 h before the addition of cytochalasin B (4 µg/mL; Sigma-Aldrich) as recommended by the IAEA [5]. After an additional 48 h, cell suspensions were transferred to 50 mL polypropylene tubes and centrifuged at 200xg for 8 min. The supernatant was removed, and the cell pellets were resuspended in 30 mL of a 1X concentration of FACS lysing solution (BD Biosciences) then incubated at room temperature for 10 min. The samples were then washed twice at 1300xg with 10 mL of phosphate-buffered saline (PBS) solution, and the pellet was resuspended in 100 µL of PBS. Lymphocyte cell concentrations were in the range of 1-2 x 10<sup>7</sup> cells/mL.

### **3.3.4. DNA staining with DRAQ5**

DRAQ5 fluorescent probe (Thermo Scientific, Rockford, IL) is a far-red DNA stain used for labelling the DNA content in live or fixed cells. DRAQ5 stains DNA through high binding affinity for nucleotide base pairs (adenine-thymine and cytosine-guanine) [80]. The

rationale for the use of DRAQ5 in the ISX-CBMN protocol is twofold: ease of use and excitation wavelength range.

Introduction of DRAQ5 to the sample required only addition of the stain at the proper volume to achieve the desired concentration in each sample (50  $\mu\text{M}$ ) which was determined through titration experiments. Unlike many other fluorescent dyes, there are no additional washing or rinsing steps required. Further, complete staining of the nuclei occurs rapidly, within 5 min of introduction to the sample. Figure 3-1 shows the maximum excitation and emission wavelengths of DRAQ5. The maximum excitation wavelength is around 650 nm that aligns well with the 658 nm excitation laser in the ISX.

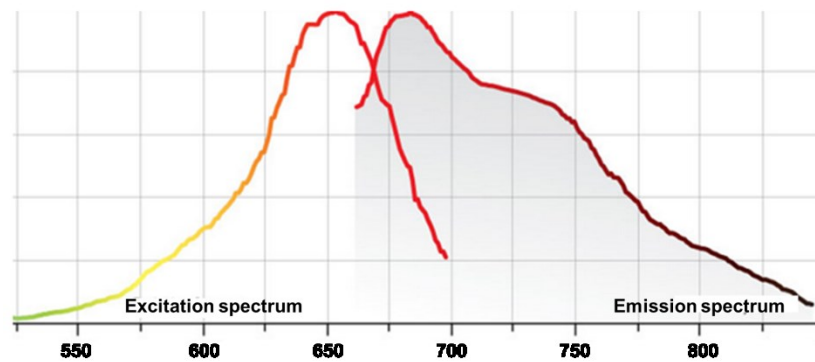


**Figure 3-1:** The excitation and emission spectra of DRAQ5. The maximum excitation is 650 nm while the maximum emission is 685 nm [80].

Diluting DRAQ5 in PBS to a concentration of 50  $\mu\text{M}$  allowed for the power of the 658 nm laser to be relatively low (20 mW) while maintaining a sufficiently high intensity signal. The recommended volume of native DRAQ5 to be added is 1  $\mu\text{L}$  to a sample that contains  $4 \times 10^5$  cells/mL. To calculate the volume of 50  $\mu\text{M}$  DRAQ5 to be added to each sample based directly on the cell concentration, the following relation was used:

$$\text{Volume of DRAQ5} = \frac{\text{number of cells per mL}}{4 \times 10^5 \text{ cells per mL}} \quad (3-1)$$

Adding diluted DRAQ5 in this manner eliminated any large variations in stain intensity between samples and also allowed all settings on the ISX and in the data analysis template to remain constant.

### **3.3.5. Cytoplasm stains and cell surface markers**

One of the key aspects of the CBMN assay is clear delineation of the cytoplasm to identify true BNCs. The BF images from the ISX provide a very clear delineation of the cytoplasm, but several experiments were performed to investigate the feasibility of using cell surface markers and membrane stains to better enhance the cytoplasm. Two fluorescent dyes were used in this process; the cluster of differentiation 3 (CD3) antibody and PKH67 cell membrane stain. CD3 is a protein complex found in T lymphocytes; lymphocytes that mature in the thymus gland and are stimulated by PHA [81]. The R-phycoerythrin (PE) CD3 antibody binds to CD3 and has maximum excitation and emission wavelengths of 496 nm and 520 nm respectively. PKH67 incorporates a green fluorescent dye into the lipid regions of the cell membrane and has a maximum fluorescent excitation and emission wavelengths of 490 nm and 502 nm respectively. Several titration experiments were performed to determine the optimal concentration of each stain to be added to each sample based on cell concentrations and ISX settings. This allowed nuclei and cytoplasmic material to be viewed simultaneously in samples stained with CD3 and DRAQ5 as well as in additional samples stained with PKH67 and DRAQ5. Figure 3-2 shows images obtained from the ISX. In some cases using CD3 and PKH67 the cytoplasm is stained uniformly as seen in Figure 3-2A and Figure 3-2C respectively.

However, in other cases the staining is sparse and does not provide a clear delineation of the cytoplasm (Figure 3-2B and Figure 3-2D). Several experiments were performed but the use of CD3 or PKH67 offered little to no enhancement over the delineation of the cytoplasm provided by the BF images. Furthermore, the introduction of these stains to the sample required additional processing time, cost and generated more cell loss for no significant gain, all factors that are undesirable for triage biodosimetry. Therefore, it was ultimately decided to remove the use of additional stains and rely solely on BF imaging of the cytoplasm to compliment DRAQ5 imaging of the MN and BNCs.

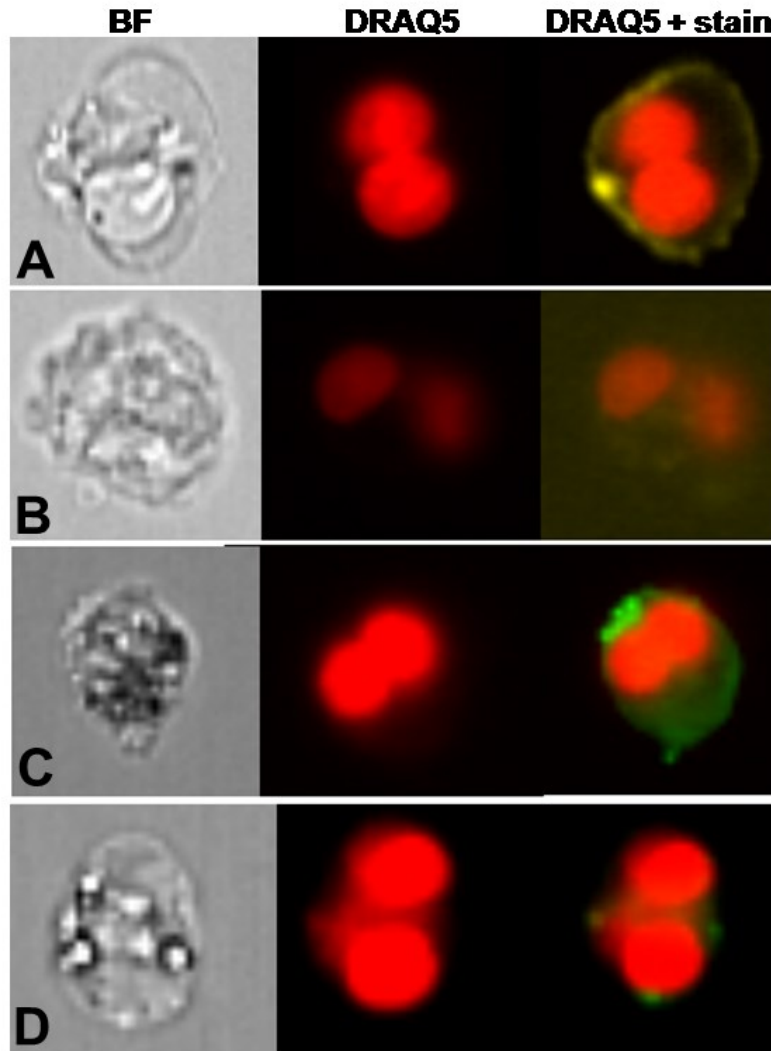


**Figure 3-2:** Images from the ISX illustrating the use of the BF, DRAQ5, CD3 and PKH67 stains. **A.** A BNC stained with DRAQ5 and CD3 illustrating a well delineated cytoplasm. **B.** A BNC stained with DRAQ5 and CD3 illustrating a poorly delineated cytoplasm. **C.** A BNC stained with DRAQ5 and PKH67 illustrating a well delineated cytoplasm. **D.** A BNC stained with DRAQ5 and PKH67 illustrating a poorly delineated cytoplasm. In all images it is clear that the cytoplasm can be easily identified using the BF images.

In most slide-based methods of the CBMN assay, DAPI is typically used to stain MN and BNCs [37, 39, 67]. While the use of several fluorescent dyes including DAPI was considered for the ISX-CBMN method, DRAQ5 offers several significant advantages. First, the optimal excitation wavelength of DRAQ5 is 650 nm [80]. The ISX contains a 658 nm laser that allows maximum excitation to be achieved easily, even at low laser powers.

This offers the advantage of visualizing even dimly stained nuclei and MN. By contrast, the optimal excitation wavelength of DAPI is 345 nm [82]. The closest laser to this wavelength in the ISX is 405 nm, that would require a higher laser power to achieve maximum excitation, and may not allow for the visualization of dimly stained nuclei and MN. Additionally, UV excitation lasers are not standard in most imaging cytometers, so choosing a dye such as DRAQ5 that is complimentary to the standard cytometer equipment makes the method developed here more transferable to other laboratories. Second, the most important advantage that DRAQ5 offers over DAPI is the reduction in washing and incubation times. When adding DAPI to a suspension of cells, an incubation time of 2-10 min followed by an additional washing step to remove any excess stain is recommended [82]. This can result in a loss of cells and adds additional processing time to the method. DRAQ5 has a shorter incubation time (2-5 min) and does not require an extra washing step following addition to a sample. Therefore, in radiation biodosimetry where speed of sample processing is a critical factor, DRAQ5 offers several significant advantages over DAPI and other fluorescent dyes. The final version of the ISX-CBMN protocol can be found in Appendix I.

### **3.3.6. Data collection on the ImageStream<sup>x</sup>**

The ISX flow cytometer is an imaging flow cytometry system capable of taking high-resolution photographs of individual cells at a rate of several hundred cells per second. All samples were stained with DRAQ5 (5 mM, eBioscience, San Diego, CA, USA) which has an affinity for double-stranded DNA. Appropriate volumes of DRAQ5 at a concentration of 50  $\mu$ M were added to each 100  $\mu$ L cell suspension. All samples were run on the ISX at 40x magnification with the 658 nm laser set to 20 mW in channel 5 and the bright field (BF) LED in channel 1. Events with areas smaller than 100 pixels (25  $\mu$ m<sup>2</sup>) and larger than

2,000 pixels ( $500 \mu\text{m}^2$ ) were excluded (note that 1 pixel =  $0.25 \mu\text{m}^2$ ). These parameters eliminated the collection of small debris and maximized BNC collection while maintaining a collection speed of approximately 100 events per second. The data were analyzed using a template developed in the IDEAS® software package (EMD-Millipore).

### **3.3.7. Data analysis in IDEAS®**

An analysis template was designed in IDEAS® which gated out undesirable events based on size, intensity, aspect ratio and DRAQ5 homogeneity and subsequently identified and automatically scored the MN frequency in BNCs in the remaining events. Once established, this template was used to analyze all data files. Detailed steps of the analysis are described below. All events were first sorted using the lobe count feature applied to the DRAQ5 channel to differentiate cells with two distinct DRAQ5-stained nuclei from all other events in the data set (Figure 3-3). Cytoplasmic material can be viewed in the BF channel; a histogram of the BF aspect ratio was created in order to distinguish between two mononucleated cells captured together in one image and a true BNC (Figure 3-4). In IDEAS®, the aspect ratio is defined as the length of the minor axis of the image divided by the length of the major axis of the image and is a measure of the roundness of the object. Therefore, single cells will have an aspect ratio close to 1, while two mononuclear cells captured together in the same image will be more elongated and have an aspect ratio closer to 0.5.

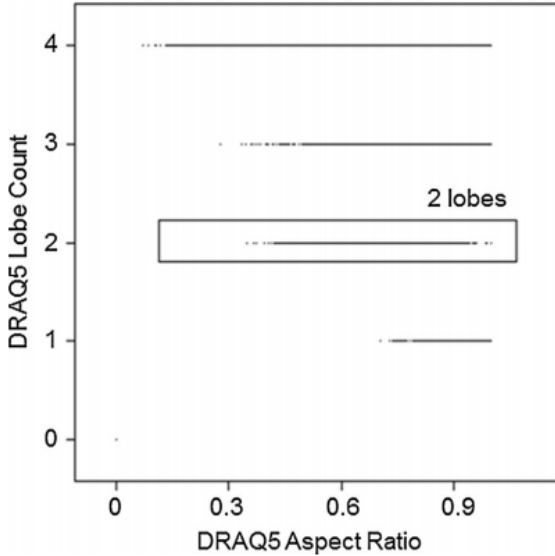


**Figure 3-3:** Scatter plot of DRAQ5 lobe count versus aspect ratio showing the gate created to include all cells with two DRAQ5-stained nuclei and to exclude debris, single cells and cells with more than two nuclei.

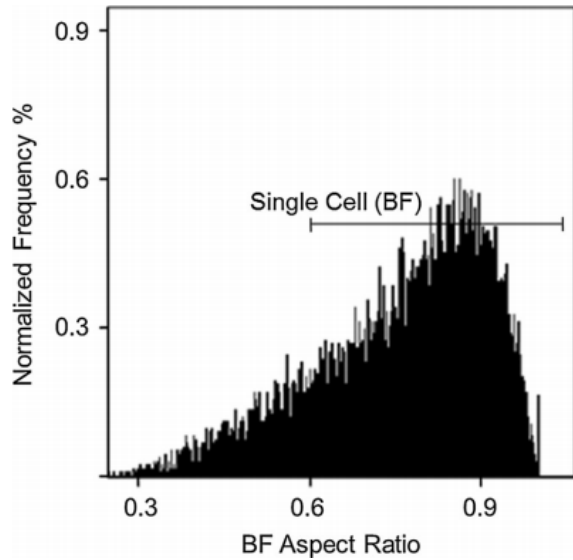


**Figure 3-4:** Histogram of BF aspect ratio showing the gate created to distinguish single cells from two MNCs captured together in the same image. Aspect ratio is defined as the length of the minor axis of the image divided by the length of the major axis of the image and describes how round an object is. Two MNCs captured together in the same image would be found below the lower limit of the gate (i.e., below an aspect ratio of 0.6).

All cells with an aspect ratio greater than 0.6 were determined to be true BNCs by optimization using a combination of the definition of aspect ratio and visual verification that less than 20% of the excluded events were true BNCs. Initially, the lower limit was set to 0.5, but upon visual inspection, many events with two single cells captured together in the same image were passing through the filtering gate and being included as BNCs. When raising the aspect ratio threshold to 0.7, these events were eliminated; however, more than 20% of events which were true BNCs were being filtered out due to their cytoplasm falling below the roundness threshold for an aspect ratio of 0.7. Thus, it was determined that an aspect ratio of 0.6 gave an optimal trade-off between gating out two mononuclear cells captured together in one image while allowing true BNCs to be carried forward in the analysis.

To remove any remaining debris, a histogram of DRAQ5 area was created, and any cells with an area of less than  $50 \mu\text{m}^2$  or greater than  $300 \mu\text{m}^2$  were rejected (Figure 3-5). A scatter plot of cell homogeneity in the DRAQ5 channel versus cell width in the DRAQ5 channel was generated (Figure 3-6). Homogeneity is a texture feature based on the local intensity in the DRAQ5 images. BNCs with two well-defined nuclei have a more uniform intensity profile and a higher homogeneity as compared to debris and other cells where the nuclei are not well separated from each other inside the cytoplasm. To set the gate limits, the excluded population was examined to verify that no more than 20% of these events were true BNCs. It was determined that cells with a mean homogeneity lower than 10 were deemed to be less than ideal BNCs. The width feature creates an elongated rectangle around the two nuclei in the DRAQ5 channel and calculates the length of the shorter side. Nuclei with widths less than  $12 \mu\text{m}$  or greater than  $18 \mu\text{m}$  were determined not to be BNCs and were removed from analysis by visually ensuring that less than 20% of these excluded events were not true BNCs. Finally, a plot of DRAQ5 compactness

versus DRAQ5 aspect ratio intensity was generated (Figure 3-7). Compactness of DRAQ5 measures the degree of how well the object is packed together and allows for differentiation from well-rounded objects, such as cells with a single nucleus, to more irregular objects, such as BNCs.

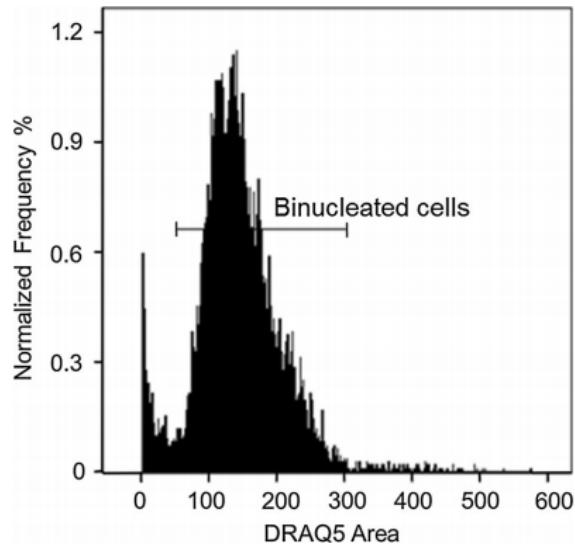


**Figure 3-5:** Histogram of DRAQ5 area showing the gate encompassing cells between 50 and 300  $\mu\text{m}^2$  to exclude any small or large debris or cells.

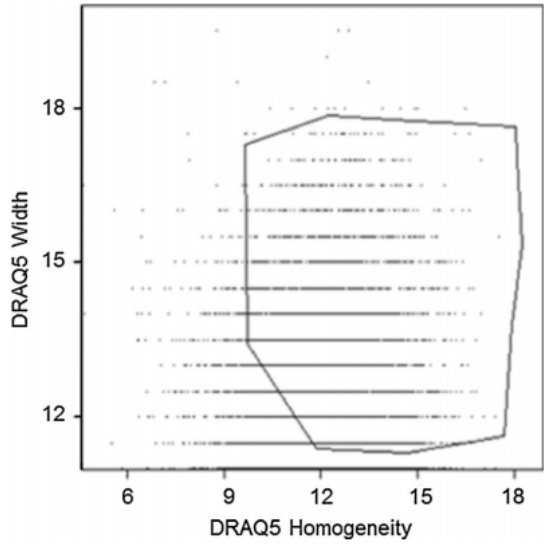


**Figure 3-6:** Scatter plot of DRAQ5 width versus homogeneity illustrating the gate to include cells with more uniform distribution of DRAQ5 stain (homogeneity greater than 10) and to reject cells that were too small or too large (width less than 12  $\mu\text{m}$  or greater than 18  $\mu\text{m}$ , respectively).

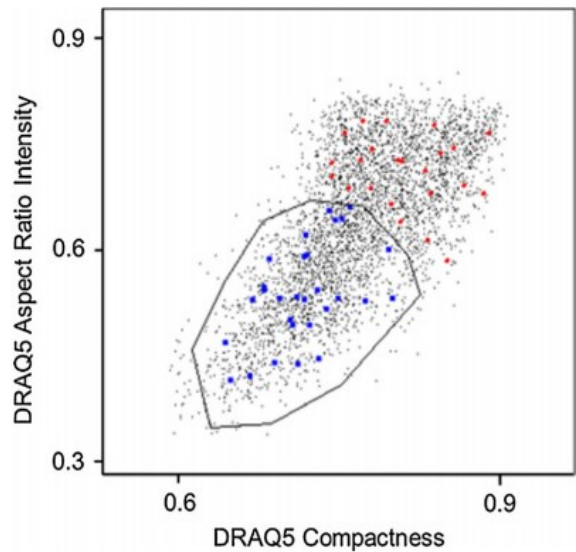


**Figure 3-7:** Scatter plot of DRAQ5 aspect ratio intensity versus compactness with the gate created to encompass the acceptable BNC population (solid blue squares inside gate). Cells highlighted by solid red diamonds are not BNCs and fall outside the gate.

To set the gates in Figure 3-7, inspection of the excluded population was again performed to ensure that less than 20% of these events were BNCs. Most BNCs were

found to have a DRAQ5 compactness between 0.6 and 0.8, so all events outside of this range were rejected. The DRAQ5 aspect ratio intensity is typically employed to distinguish single nuclei from double nuclei. The majority of BNCs were found to have an aspect ratio intensity between 0.4 and 0.7, and events outside of this range were excluded. Figure 3-7 also illustrates how a selected population of BNCs (solid blue squares) falls well within the gate and a selected population of non-BNCs (solid red triangles) falls outside of the gate. The gating strategy presented here effectively selects for BNCs while eliminating small and large debris, single cells and other non-desirable objects within each data set. Using the gated data, a masking system developed in IDEAS® was used to identify MN in each image.

The IDEAS® software contains a large selection of criteria for image analysis, called features, which generate quantitative and positional information about an image. Features are applied to locations of an image through the use of masks that identify pixels within the region of interest of the image. To perform automated MN identification and counting, a series of masks were created in IDEAS®. First, a DRAQ5 intensity threshold was applied to remove any debris that remained in the population following the gating strategy described above. Next, spot masking was used to identify both DRAQ5-stained MN and BNCs. The spot mask makes use of the spot-to-cell background ratio, which is the spot pixel value divided by the background, as well as the radius value of the spot. A DRAQ5 MN mask was created to identify spots in images that had a spot-to-cell background value of at least 1.5 and a radius of at least 8 pixels. An area range between 10 pixels ( $2.5 \mu\text{m}^2$ ) and 100 pixels ( $25 \mu\text{m}^2$ ) was then placed on the MN mask to ensure that all MN scored adhered to the guidelines specified by Fenech et al. [47, 67]. These guidelines state that MN should have an area between  $1/256$  and  $1/9$  of the main nuclei. A typical nucleus in the images obtained has an area of about 300 pixels ( $75 \mu\text{m}^2$ ), which translates the criteria

limits for MN to about 1 pixel ( $0.25 \mu\text{m}^2$ ) and 33 pixels ( $8.25 \mu\text{m}^2$ ), respectively. To avoid the incorrect masking of very small debris or DRAQ5 intensity artifacts, the lower limit area on the MN mask was increased by a factor of 10 to the final value of 10 pixels ( $2.5 \mu\text{m}^2$ ). In a similar fashion, a BNC spot mask was created to identify images that contained two distinguishable DRAQ5-stained nuclei within a single cell. Here, the spot-to-cell background ratio was set to at least 2.5, and the radius was set to a minimum of 18 pixels to mask both nuclei while excluding any MN from the mask. A threshold area was set to 300 pixels, sufficient to mask all nuclei. Figure 3-8a shows a BNC with one MN, Figure 3-8b shows the MN mask and Figure 3-8c shows the BNC mask. Finally, to count the MN in each data set, a spot count feature was applied, which counted all masked MN. A histogram of MN frequency was then plotted, with a gate on each bin from 0 to 4 MN per BNC. The gate on the 4 MN bin is inclusive of 4 or more MN per BNC Figure 3-9.

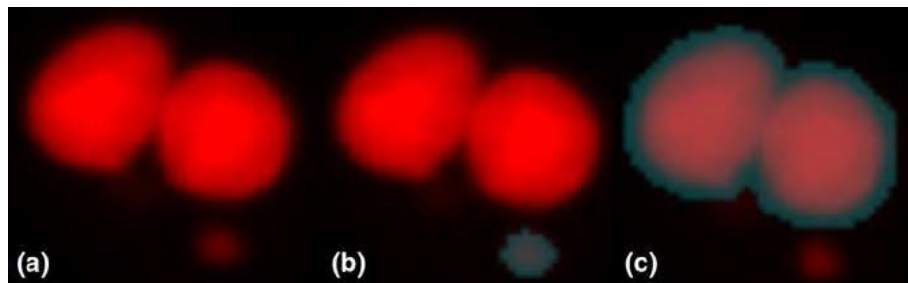


**Figure 3-8:** (a) A DRAQ5-stained BNC with a single MN. (b) The MN mask highlighting the MN. (c) The BNC mask encompassing the two nuclei.

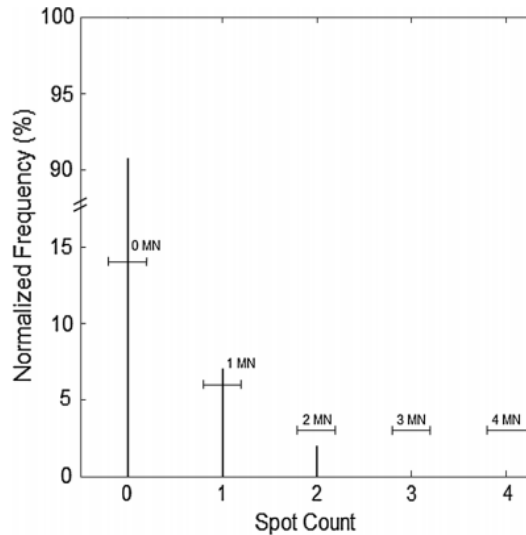


**Figure 3-9:** Histogram of the spot count feature created using the BNC and MN masks for a sample irradiated with 4 Gy. The gates shown are used to count the number of cells that are binucleated with no MN (0 MN) and the BNCs with the corresponding number of MN in each bin. The gate on the 4 MN bin counts all cells with 4 or more MN. The normalized frequency represents the percentage of each type of cell from the total number of cells in the population.

### 3.4. Results

The ISX allows the opportunity to visualize particles on several channels as they pass through the cytometer. The BF channel allows for both imaging of the cytoplasm and composite image generation in which the DRAQ5-stained nuclei and MN can be overlaid to clearly distinguish between true BNCs with MN (first to third rows of Figure 3-10) and two individual mononuclear cells captured in the same image (fifth row of Figure 3-10). It is straightforward to identify mononuclear cells and associated MN (fourth row of Figure 3-10) as well as multi-nucleated cells (sixth row of Figure 3-10) by simply creating additional ages using the lobe count feature.

To improve delineation of the cytoplasm, the use of cytoplasm stains and cell surface markers was investigated. While all stains employed were easily visualized by the ImageStream<sup>x</sup>, uniformity of the stain was not as good as expected and offered little enhancement over the gating strategies developed using the BF images. Furthermore, the

staining steps added additional time and cost to the sample preparation method for no significant gain, which is undesirable for the applications of this method to rapid triage biodosimetry.

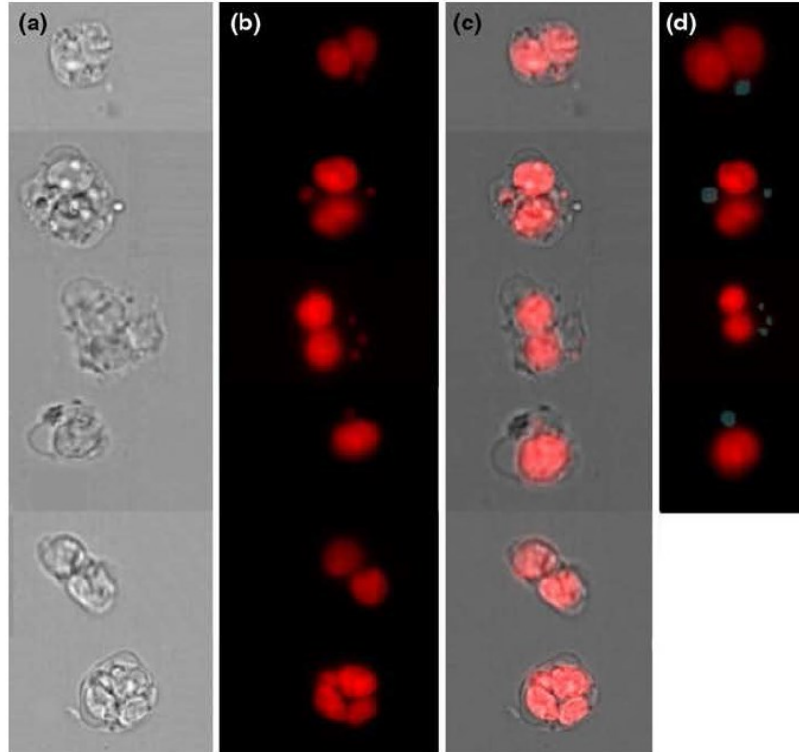


**Figure 3-10:** Various images captured by the ISX. (a) BF images clearly depicting the cytoplasm boundaries around the nuclei. (b) DRAQ5-stained nuclei and MN. (c) Composite BF/DRAQ5 images created to illustrate the use of the BG image to delineate the cytoplasm surrounding the nuclei. (d) *First row* a BNC with one masked MN, *second row* a BNC with two masked MN, *third row* a BNC with three masked MN, *fourth row* a mononuclear cell with one masked MN, *fifth row* two mononuclear cells captured in the same image, *sixth row* a tetranucleated cell.

Four independent experiments were conducted employing the methods described above. Figure 3-11 shows the data from the individual experiments as well as the dose response curve that is a weighted average of the four data sets generated for doses between 0 Gy and 4 Gy. The ordinate is presented as the rate of MN per BNC, and the data follow a linear-quadratic function ( $R^2 = 0.994$ ); however, examination of the equation

of the fit reveals that the linear term contributes to the fit more than the quadratic term. Given the early stages of this work, the increasing frequency of MN per BNC with dose is encouraging and indicates that this method is sensitive enough to distinguish between a 0 Gy and 2 Gy irradiated sample as the two means are statistically different ( $P = 0.00021$ ), which would be sufficient for rapid casualty triage. Figure 3-12 shows the results from 0 Gy to 7 Gy, which is also a weighted average of the four data sets. It can be seen that the MN frequency increased up to 4 Gy and then starts to decrease at higher doses.

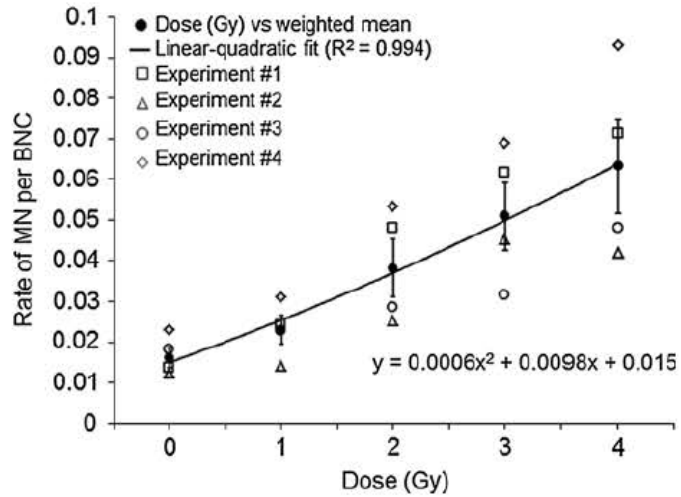


**Figure 3-11:** Data from four experiments as well as the dose response curve from 0 to 4 Gy, which represents the weighted mean number of MN/BNC identified for each dose. Error bars represent the standard error of the mean and the curve is fit with a linear-quadratic function ( $R^2 = 0.994$ )

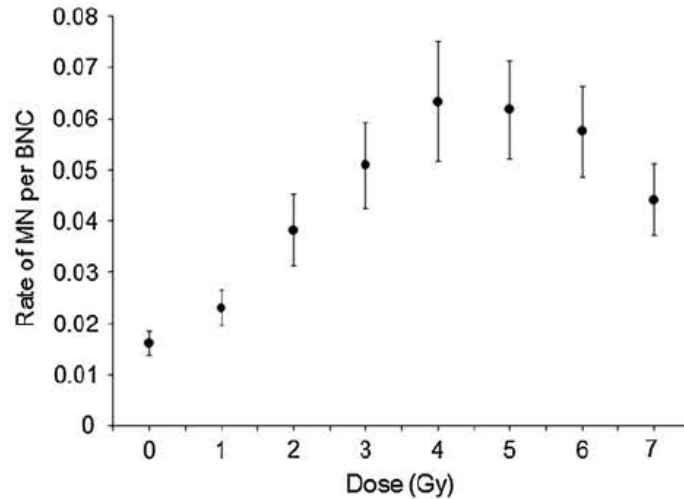


**Figure 3-12:** Data from four experiments from 0 to 7 Gy. Shaded circles represent the weighted average number of MN/BNC identified for a given dose and the error bars represent the standard error of the mean.

To evaluate the sensitivity of the method at doses below 1 Gy, five additional independent experiments with five donors were conducted employing the methods described in section 3.3. Figure 3-13 shows an increase in the average rate of MN per BNC from an average of 0.007 at 0 Gy to an average of 0.013 at 1 Gy, indicating that differentiation between doses at 0 Gy and 1 Gy should be identifiable. Examining the error bars at doses of 0 Gy, 0.25 Gy, 0.5 Gy and 0.75 Gy, there is no significant difference between the 0 Gy and 0.75 Gy point, but the error bars at the 0 Gy and 1 Gy points do not overlap each other. Therefore, the lower limit of the sensitivity of the ISX-CBMN method in its current form is 1 Gy.

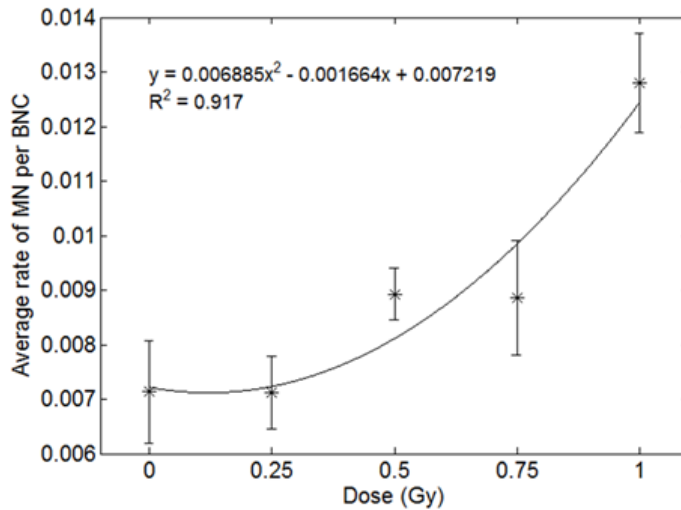


**Figure 3-13:** Data from five experiments from 0 to 1 Gy. Stars represent the weighted mean number of MN/BNC identified for a given dose and the error bars represent the standard error of the mean.

### 3.5. Discussion

An automated, imaging flow cytometry method for performing the CBMN assay for the purposes of radiation biodosimetry has been presented. In situations where large numbers of casualties may need to be assessed for possible radiation exposure, a method that is quick and robust is desirable.

In a recent publication (2013) Fenech et al. [67] provided a comprehensive review of several automated MN assays that use imaging cytometry systems. As mentioned previously, they also developed a list of criteria that all imaging systems should be able to fulfill to ensure accurate, reliable and reproducible results. While the method presented here does not use slide-based scoring, it does satisfy a number of the outlined criteria, as explained below. Imaging of the cytoplasm is as important as imaging the nuclei and MN, such that mono-, bi- and multi-nucleated cells can be identified and quantified. It has been demonstrated that this can be accomplished with the ISX. Another consideration that Fenech et al. [67] pointed out is that imaging cytometry systems should have a high

detection efficiency for MN in both mononucleated cells and BNCs. The frequency of MN per BNC measured by the ImageStream<sup>x</sup> is currently one full order of magnitude lower than traditional microscopy-based methods of CBMN for radiation biodosimetry [35, 36]. Studies by Varga et al. [39] and Schunck et al. [61], in which the Metafer system was used to automate the slide-scoring method for CBMN, both reported lower rates of MN as compared to the traditional manual scoring method. According to the authors, the stricter scoring parameters applied in image analysis can cause some MN that would normally be counted manually, to be missed. For example, MN in contact with the nuclei would normally be counted manually, but are excluded by virtue of the automated scoring parameters. In this work, the lower MN frequency may also be due to some of the true BNCs being removed from the final population as a result of the gating strategy. It may also be as a result of the cells being in solution as opposed to on slides. In this three-dimensional system, some MN may be hidden behind a nucleus such that they cannot be visualized or MN may be at a different depth of field than the nuclei and are not intense enough to be clearly identified and masked. Additional data were collected using the extended depth of field option on the ISX, but no improvement in MN frequency or image quality was observed. Therefore, the lower MN frequency may simply be a general phenomenon of automated analysis methods. Beaton et al. [31] recently reported on this same trend while performing the DCA on the ISX. This is likely not a major drawback for the purposes of triage biodosimetry as the low MN frequency would be accounted for in the dose response curve. All samples would be analyzed using the same IDEAS<sup>®</sup> template employed to generate the curve and the results compared to the curve itself; thus, the low MN frequency likely becomes irrelevant. Further, in a mass casualty event, the distinction between low (0 Gy) and high doses (>2 Gy) must be made quickly [6]. The dose response curve shown in Figure 3-11 indicates that the automated method

developed in this work is capable of rapidly making the distinction between 0 Gy and 2 Gy. Furthermore, it can be argued that in a situation where a casualty has received a total body dose of greater than 4 Gy, such as a radiation accident, the deterministic effects would trigger medical intervention long before the 72-h incubation period required for the CBMN assay is complete and rapid dose determination becomes less important than accuracy [16]. Conversely, when optimizing the method to determine its sensitivity, the low MN frequency will likely play a significant role. It is possible that the MN frequency can be increased by further refining and optimizing the analysis strategy to detect any smaller MN that may be gated out or missed by the masking.

In order to obtain maximum confidence to accept or reject objects as MN, a sufficiently high magnification must be employed in all imaging cytometry methods [67]. The ISX has three objectives (20x, 40x and 60x), all of which were investigated for their ability to image BNCs and MN with sufficient resolution. The 40x objective proved to give the best combination of acquisition speed and image resolution. At higher magnification, a reduction in collection speed was observed and therefore, to obtain sufficient image quality while maintaining high throughput, all data were collected using settings optimized for the 40x objective.

Apart from the measurement of MN, the CBMN assay has been adapted to quantify other important biomarkers such as nucleoplasmic bridges, nuclear buds and necrotic or apoptotic cells [67]. While the measurement of these falls outside of the scope of this chapter, the breadth of applications within the IDEAS® software package may indeed make it possible in future to quantify these structures.

At high doses of radiation, it can be seen that the frequency of MN per BNC falls off, specifically after 5 Gy (Figure 3-12). The number of BNCs acquired and scored also decreased beyond 5 Gy. This is consistent with results of dose response curves recently

generated by Lyulko et al. [66] and Müller and Rode [51] in which similar trends were observed up to 10 Gy and 15 Gy, respectively. The reduction in BNC and MN frequency at higher doses can likely be explained by the effect of radiation on cell proliferation and the inability of the cells to pass through karyokinesis [51]. Müller and Rode [51] have suggested that higher doses can be estimated through scoring the fraction of mononuclear cells as well as the ratio of trinucleated to tetranucleated cells following radiation exposure. It has been shown in this work that these structures can be detected and imaged using the ISX. Therefore, accurately estimating doses higher than 5 Gy is likely possible through the development of an IDEAS® template that can evaluate all of these criteria simultaneously, that would be significantly faster than manual scoring.

At lower doses of radiation (< 1 Gy) Figure 3-13 shows that the rate of MN per BNC nearly doubles between 0 Gy and 1 Gy. Additionally, it can be seen that the error bars (represented by the SEM of the five donors) do not overlap between the 0 Gy and the 1 Gy dose point, indicating small variability between donors. However, there is no significant difference in the rate of MN per BNC between 0 Gy and 0.75 Gy as illustrated by the overlapping error bars. Therefore, it is reasonable to suggest that in its current form, the ISX-CBMN method may be able to generate accurate dose estimates below 1 Gy but with low precision.

In addition to satisfying the aforementioned criteria, performing the CBMN assay on the ISX has other advantages. It combines the speed of sample preparation with a data analysis method that is free of user intervention or individual bias. Willems et al. [37] recently estimated that their automated MN scoring procedure could allow 2 technicians to process approximately 60 samples in a 12 h shift. We estimate that the imaging flow cytometry CBMN method developed here can allow for the complete analysis of at least the same number of samples, perhaps even more, in a 12 h period due to the fact that the

flow CBMN method does not require slide preparation time. With the condensed method employed in this work, approximately 2 h was needed to completely process the 8 samples used to generate Figure 3-12, from the end of incubation to a stage where they were ready to be run on the ISX. Once ready for analysis on the ISX, each sample can take between 10 and 20 min to acquire and another 5-10 min to analyze with the IDEAS® analysis template. The data collection and analysis time for all doses presented here (0-7 Gy) was approximately 2 h. Thus, a total of about 4 h was required to generate Figure 3-12 by a single person working alone in the laboratory from end of incubation to final results.

An average of 1,800 BNCs was counted in the analysis template for each dose point, but the number of cells detected is much higher. The gating strategy removes many unsuitable cells (e.g., mononuclear cells), and further improvements to the analysis template should increase the efficiency of separating more BNCs from debris and other non-desirable events. Still, 1,800 BNCs is nearly double the number of BNCs that are scored per sample by conventional microscope-based CBMN. Future refinement of the data collection parameters on the ISX, as well as the analysis template, may make it possible to automatically identify, count and analyze 1,000 BNCs and associated MN in 15 min per sample. Furthermore, the IDEAS® software possesses a batch processing mode that has the capability to process several data files simultaneously and to save the statistical data as a report. This batch processing mode in combination with the use of a 96-well plate could allow even further improvements in throughput. Still, as with all methods to perform the CBMN assay, the 72 h sample incubation time remains the major limiting factor on the overall speed of the assay. Hence, a reduction in the time from incubation to results is of utmost importance in a mass casualty event, and the imaging flow CBMN method presented in this chapter could conceivably generate a dose estimation for a single individual in as little as 2 h following the incubation time.

The results presented in this chapter indicate that imaging flow cytometry can be used to automate the CBMN assay for the purposes of rapid triage biodosimetry. This work compliments other recent publications in which imaging flow cytometry has been used to automate the DCA [31] and other slide-based techniques that have been developed to automate the CBMN and  $\gamma$ H2AX assays [64-66] for the purposes of radiation biodosimetry. Further work is required to optimize the masking and analysis template to possibly increase the MN detection frequency. Additional experiments will be performed in an attempt to accurately estimate high radiation doses (>5 Gy) by developing a template that simultaneously analyzes the data based on several criteria mentioned previously. Finally, determination of the sensitivity of the method at very low doses and validation using blinded samples will be performed.

### **3.6. Acknowledgements**

The author wishes to thank Richard DeMarco (Amnis Corp., EMD-Millipore) for his help with the gating and masking strategies in the IDEAS® software.

## **4. MULTI-PARAMETER DOSE ESTIMATIONS IN RADIATION BIODOSIMETRY USING THE AUTOMATED CYTOKINESIS-BLOCK MICRONUCLEUS ASSAY WITH IMAGING FLOW CYTOMETRY**

### **4.1. Summary**

This chapter is based on the publication *Multi-Parameter Dose Estimations in Radiation Biodosimetry using the Automated Cytokinesis-Block Micronucleus Assay with Imaging Flow Cytometry* published in the journal of *Cytometry Part A* (85A, 883-893, 2014) [83]. This work optimizes and expands the previously developed ISX-CBMN assay to a multi-parameter biodosimetry analysis tool in which the rate of MN per BNC, the percentage of MNCs and the RI may be used in combination to provide dose estimations with higher throughput than is currently available with standard microscopy.

Additional material describing results on receiver operating characteristics (ROC) of the automated data analysis template in IDEAS® as well as individual donor variability are included. In addition, figures have been modified from the paper such that one plot is presented per figure for clarity.

### **4.2. Introduction**

When performing the CBMN assay for the purposes of radiation biodosimetry, the fundamental parameter of measure is the rate of MN per BNC, in which only cells completing first mitosis are evaluated. In order for this parameter to be quantifiable, it is imperative that MN be scored while they remain inside the cytoplasm of a BNC. Therefore, the aforementioned procedures for performing the CBMN assay using FCM in section 2.1.5.2 are less than ideal for biodosimetry. The ISX imaging flow cytometer offers the

ability to not only identify a population of cells using traditional gating methods, but also to confirm the contents of each population by visual inspection, and effectively eliminates the need for lysing lymphocytes to liberate MN and nuclei from the cytoplasm.

This work builds upon the results of Chapter 3 in which a novel, automated protocol to perform the CBMN assay on the ISX is described. This chapter presents dose response calibration curves from 0 Gy to 10 Gy and investigates the feasibility of evaluating the percentage of MNCs as well as the RI, creating a multi-parameter approach for performing the CBMN assay to quantify blinded doses.

### **4.3. Materials and methods**

#### **4.3.1. Blood collection, irradiation, CBMN assay and data collection on the ImageStream<sup>x</sup>**

Blood was collected by the procedure described in section 3.3.1 from six healthy anonymous donors (3 males and 3 females between the ages of 27 and 48). Eleven samples, each consisting of 2.5 mL aliquots, were irradiated to doses ranging from 0 to 10 Gy in 1 Gy increments. Irradiation was performed according to the procedure described in section 3.3.1. The CBMN assay was performed on all samples according to the procedure described in section 3.3.3. Data collection on the ISX was performed according to the procedure described in section 3.3.6.

#### **4.3.2. Receiver operating characteristics**

Receiver operating characteristics (ROC) are useful for describing the performance of analysis systems such as image analysis software and diagnostic systems [84]. Every object applied to a given image classifier can fall into one of four categories: true positive (TP) (condition positive, test positive), true negative (TN) (condition negative, test

negative), false positive (FP) (condition negative, test positive) or false negative (FN) (condition positive, test negative). From these parameters, a two-by-two confusion matrix (Figure 4-1) can be used to determine several factors including sensitivity (true positive rate), specificity (true negative rate) and precision (positive predictive value), that can then provide information on the accuracy (portion of true results in the whole population) of classifiers used in image analysis [84].

		Condition		
		Condition positive	Condition negative	
Test outcome	Test outcome positive	True positive (TP)	False positive (FP)	<b>Precision</b>
	Test outcome negative	False negative (FN)	True negative (TN)	<b>Negative predictive value</b>
		<b>Sensitivity</b>	<b>Specificity</b>	<b>Accuracy</b>

**Figure 4-1:** Confusion matrix and typical performance metrics calculated using the matrix.

From the confusion matrix, sensitivity, specificity, precision, negative predictive value and accuracy are defined as follows:

$$Sensitivity = \frac{TP}{TP + FN} \quad (4-1)$$

$$Specificity = \frac{TN}{FP + TN} \quad (4-2)$$

$$Precision = \frac{TP}{TP + FP} \quad (4-3)$$

$$Negative\ Predictive\ Value = \frac{TN}{FN + TN} \quad (4-4)$$

$$Accuracy = \frac{TP + TN}{Total\ population\ sampled} \quad (4-5)$$

The percentage of FP and FN BNCs and MN have been quantified by other authors using the Metafer automated slide-scoring system [37, 62, 85]. Willems et al. [37] quantified the FP rate of MN to be 6.28%, that was then reduced to about 1% after a visual inspection of all scored BNCs. In a recent publication, De Amicis et al. [62] indicated that the sensitivity and specificity of the MNscore module of the Metafer system was about 100% for several dose points analyzed between 0 Gy and 6.4 Gy. In this work, the rates of TP, TN, FP and FN for both MN and BNCs have been quantified from one donor (D9) at each dose point. The sensitivity, specificity, precision, negative predictive value and accuracy were then determined in both the original and optimized IDEAS® templates to illustrate the improvement in the gating/masking strategy.

#### **4.3.3. Donor variability in the ISX-CBMN method**

##### **4.3.3.1. Blood collection, irradiation and CBMN assay for donor variability**

In order to test the variability in the rate of MN per BNC in individual donors, blood was collected from two anonymous donors who had donated for previous experiments. Donor 21(m) and donor 28(m) previously donated blood on November 21, 2013 and January 17, 2014 respectively. Donor 21(m) donated again on February 2, 2015 and donor 28(m) donated again on February 10, 2015. This allowed the individual variation on the rate of MN per BNC over a period of approximately 1 year to be examined in each donor. Blood samples were collected in 10 mL lithium-heparinized Vacutainer® tubes and split into ten 2 mL aliquots. Five aliquots were irradiated to 2 Gy using the protocol described in section 3.3.1 while the remaining five were not irradiated (0 Gy). The ISX-CBMN method

was then performed on all ten samples as described in section 3.3.3. Aliquoting the blood in such a way allowed for the variability in both the sample processing protocol as well as the data analysis template to be examined without having to collect blood from each donor ten separate times, something that was not practical or feasible.

#### **4.3.3.2. Data collection on the ImageStream<sup>x</sup> and data analysis**

All samples were stained with DRAQ5 according to the procedure described in section 3.3.4 and run on the ISX using the settings described in section 3.3.6. Where possible, five separate data files of at least 50,000 events were collected from each of the five samples for each donor. This ensured that at least 2000 BNCs would be scored in each of the resulting 25 data sets at each dose point.

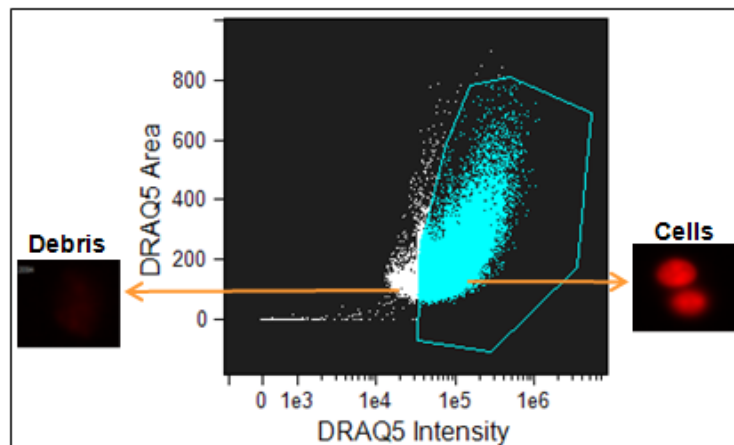
### **4.4. Results**

#### **4.4.1. Data analysis in IDEAS<sup>®</sup>**

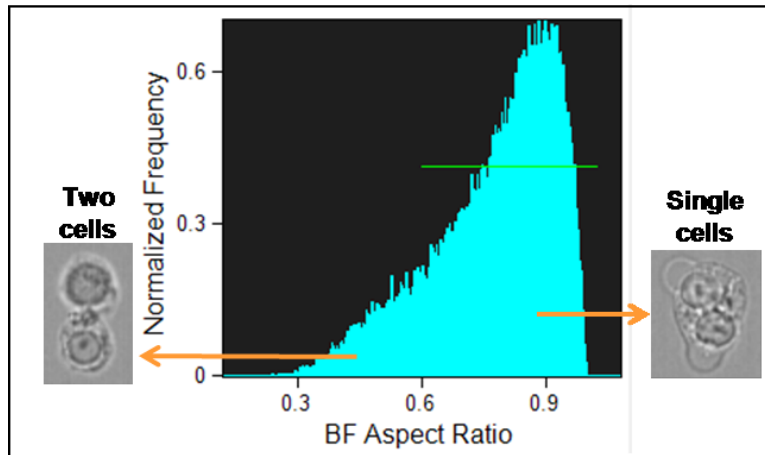
The data analysis template described in Chapter 3 has been optimized to more effectively gate out undesirable events based on parameters such as size, intensity, and aspect ratio. Through the use of these parameters, MN, BNCs, and MNCs are automatically identified and scored.

All events were first sorted using a scatter plot of DRAQ5 area versus DRAQ5 intensity to gate out any low intensity debris (Figure 4-2). A histogram of the BF aspect ratio was then created in order to distinguish between two mononucleated cells captured together in one image and a true BNC (Figure 4-3). In IDEAS<sup>®</sup>, the aspect ratio is defined as the ratio of the length of the minor axis to the length of the major axis, and is a measure of the roundness of the object. All cells with an aspect ratio of greater than 0.6 were determined through previous analysis to be most likely to be single cells [79]. The lobe

count feature was applied to the DRAQ5 channel and differentiates cells with two distinct DRAQ5-stained nuclei from all other events. A scatter plot of lobe count versus aspect ratio intensity was created and a gate (yellow) was placed around all two-lobed events, while a second gate was placed around all one and two lobed events (Figure 4-4). This second gate allowed for the identification of mononuclear cells, which will be discussed below. It should be noted that Figure 4-2 to Figure 4-4 can be generated with any nuclear dye, such as DAPI. In such a case, the gate in Figure 4-2 may be slightly different but the logistics of the geometrical parameters chosen in Figure 4-3 and Figure 4-4 remain the same, regardless of the fluorescent dye employed.



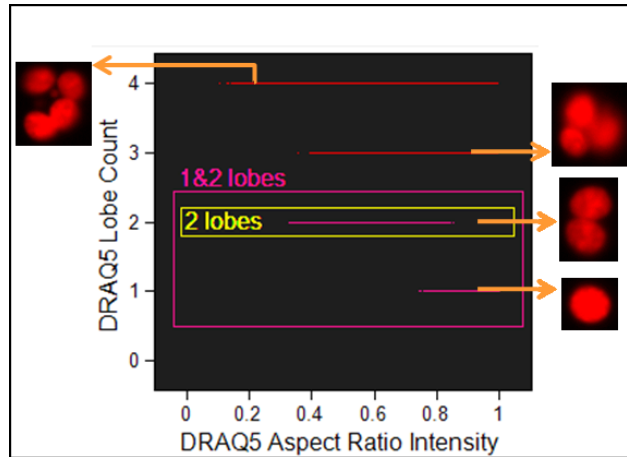
**Figure 4-2:** Scatter plot of DRAQ5 area versus intensity for elimination of debris. True cellular events have a high DRAQ5 intensity while debris events are small with low DNA content and therefore, low DRAQ5 intensity. Representative images of the populations inside and outside of the gate are shown.



**Figure 4-3:** A histogram of BF aspect ratio that differentiates between single cells and two MNCs captured together in a single image. Events with an aspect ratio of greater than 0.6 (indicated by the linear green gate) are more likely to be single cells. Representative images of the populations inside and outside of the gate are shown.

To filter any remaining debris a series of scatter plots were created as shown in Figure 4-5 to Figure 4-7. Many of the features used are based on the geometrical properties of a BNC (roundness, symmetry along an axis, etc.) and some are based on the intensity of the DRAQ5 within the cells (contrast, stain uniformity, etc.). During development of the final analysis template, we made use of the “find best feature” property in the IDEAS® software to arrive at the optimal features for filtering BNCs. This option allows the user to highlight a desired population (we chose 50 BNCs) and an undesired population (we chose 50 non-BNCs and other debris) and then apply every single feature available in the software to these populations. IDEAS® then generates a numerical value of differentiation between the two highlighted populations based on each feature; the higher the value, the better the feature is at differentiating between the two populations. After performing this test, we applied the features with the highest values to the data and determined the best combination of features to differentiate BNCs from debris using scatter plots. After

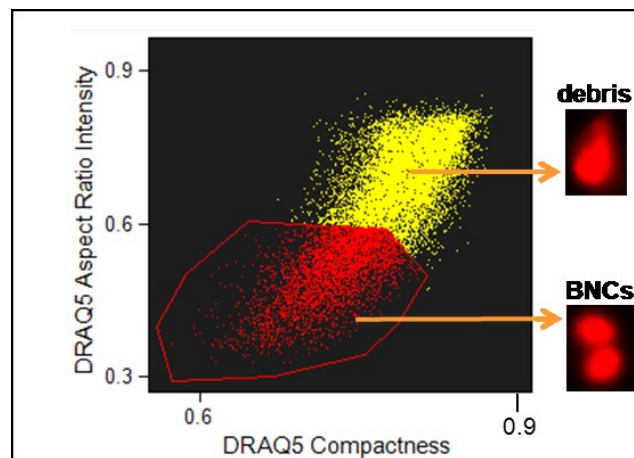
confirming by visual inspection, we arrived at the three panels presented in Figure 4-5 to Figure 4-7.



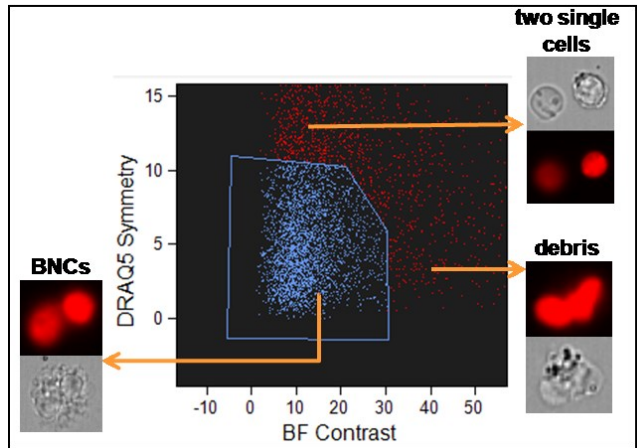
**Figure 4-4:** Scatter plot of DRAQ5 lobe count versus aspect ratio intensity for elimination of multinucleated cells. Representative images of the populations inside and outside of the gate are shown.

Figure 4-5 plots DRAQ5 aspect ratio intensity against DRAQ5 compactness, a measure of how well an object is packed together [78]. This plot presents an elegant way to simultaneously select for well-compressed objects with a low aspect ratio that are likely to be images containing two DRAQ5-stained nuclei and allows for further differentiation between BNCs and other objects. The upper limits of both features are gated out because, while the high compactness was indicative of well-rounded objects, the higher aspect ratio intensity indicates single rounded objects, whereas two rounded objects are desired. DRAQ5 symmetry is then plotted against BF contrast (Figure 4-6), taking advantage of the ability to combine image quality and geometry features in the same plot. The symmetry feature measures the tendency of an object to have two lobes oriented along a single axis of elongation that is one desired property of a BNC. The symmetry feature provided the best differentiation between BNCs and debris when combined with the BF contrast

feature, as objects with lower BF contrast had a more uniform cytoplasm. Objects with a symmetry greater than approximately 10 tended to be two mononuclear cells captured in the same image that were not gated out previously. Objects with a contrast less than about 30 had a more uniform cytoplasm. One final filtering step is a scatter plot of DRAQ5 correlation versus contrast (Figure 4-7) and was generated based largely on the results of the find best feature option in IDEAS®. Following visual inspection of the gated population in Figure 4-6, it was decided that one final filtering step between BNCs and debris was necessary. The contrast feature, as described above, is applied to the DRAQ5 channel, and again cells with a lower contrast represented images with two distinct nuclei. This was combined with the correlation feature that is a measure of graytone linear-dependencies in the image and overall, cells with correlation values between 0.2 and 0.5 were BNCs [86]. Cells with correlation values outside of this range tended to be of poor image quality.



**Figure 4-5:** Scatter plot of DRAQ5 aspect ratio intensity versus DRAQ5 compactness illustrating the gate created to differentiate BNCs from debris. Representative images of the populations inside and outside of the gate are shown.



**Figure 4-6:** Scatter plot of DRAQ5 symmetry versus BF contrast. Objects with lower symmetry are more likely to have a single axis of elongation and more likely to be two nuclei within one cytoplasm rather than two individual cells. Objects with a contrast less than 30 (arbitrary units) have a more uniform cytoplasm and are more likely to be single cells. Representative images of the populations inside and outside of the gate are shown.

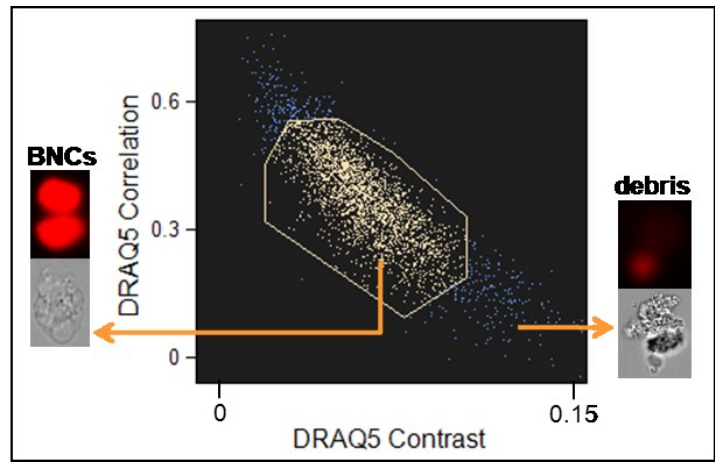


**Figure 4-7:** Scatter plot of DRAQ5 correlation versus contrast. Objects with low contrast and correlation values between 0.2 – 0.5 tended to be more uniformly stained and were more likely to be two distinct nuclei. Representative images of the populations inside and outside of the gate are shown.

To perform automated BNC, MN, and mononuclear identification and scoring, masks were created in IDEAS®. The spot masking feature, which makes use of the ratio between individual pixel intensities and the average background intensity of the image, was used

to identify both MN and BNCs [78]. A BNC mask was created to identify images that contained two distinguishable DRAQ5-stained nuclei within a single cell, using a spot-to-cell background value of 1.75 and a minimum radius of 10 pixels (Figure 4-8A). A MN mask was created to identify spots in images that had a spot-to-cell background value of 1.5 and a radius of at least 8 pixels (Figure 4-8B and Figure 4-8C). An area range between 10 pixels ( $2.5 \mu\text{m}^2$ ) and 120 pixels ( $30 \mu\text{m}^2$ ) was then placed on the MN mask to ensure that all MN scored adhered to the guidelines specified by Fenech et al. [47, 67] that state that MN should have an area  $1/256$  to  $1/9$  of one nucleus. In the images obtained, a typical nucleus has an area of about 300 pixels ( $75 \mu\text{m}^2$ ), which translates the criteria limits for MN to about 1 pixel ( $0.25 \mu\text{m}^2$ ) and 33 pixels ( $8.25 \mu\text{m}^2$ ), respectively. However, to avoid the incorrect masking of very tiny debris or DRAQ5 intensity artifacts, the lower limit area on the MN mask was increased by a factor of 10 to the final value of 10 pixels ( $2.5 \mu\text{m}^2$ ). Also, to ensure all larger MN were masked correctly, the upper limit area was increased to the final value of 120 pixels ( $30 \mu\text{m}^2$ ). Visual inspection of several images was performed during the mask development process to ensure this increase on the upper limit was large enough to sufficiently capture MN that fit into the scoring criteria, but not so large as to mask nuclei or debris that were not true MN. Finally, a mononuclear cell mask was created using the spot count feature with a spot-to-cell background value of 2 and a radius of at least 16 pixels (Figure 4-8D).

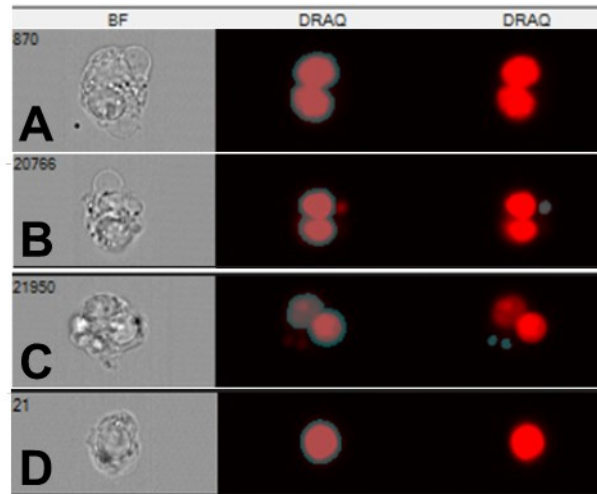


**Figure 4-8:** Panels A to D present various cell images from the ISX. Panel A shows a BNC with the BNC nuclear mask. Panel B shows a BNC with one MN illustrating both the BNC and MN masks. Panel C shows a BNC with two MN and the associated masks. Panel D shows a mononuclear cell with its associated nuclear mask.

In order to automatically count the BNCs, MN, and mononuclear cells in each data set, a spot count feature was applied to each mask to count all of the masked elements in a population. A histogram of MN frequency was plotted (Figure 4-9), with a gate on each bin from 0 to 4 MN, where the 0 MN gate is a count of all the masked BNCs with no MN in the final filtered population in Figure 4-7. The gate on the 4 MN bin is inclusive of 4 or more MN per BNC. To count the number of mononuclear cells in the data set, a gate was placed around the one and two lobed populations in Figure 4-4. The mononuclear mask was applied to this population and a new lobe count, based on the mask, was generated. A scatter plot of the new lobe count was plotted against DRAQ5 aspect ratio intensity (Figure 4-10). A gate was then placed around the one-lobed events, with a minimum aspect ratio intensity threshold 0.7. This ensured that all gated events were single cells with a single DRAQ5-stained nucleus and hence, true mononuclear cells.

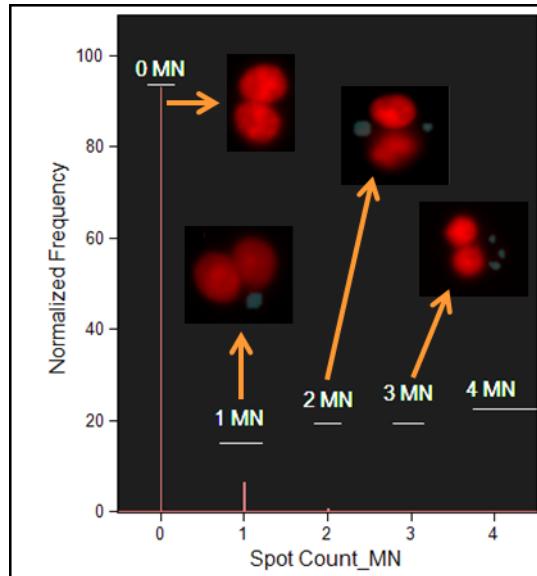


**Figure 4-9:** Histogram of the spot count feature created using the BNC and MN masks for a sample irradiated with 3 Gy. The gates shown are used to count the number of BNCs with the associated number of MN in each bin. The gate on the 4 MN bin is inclusive of any cells with four or more MN. Example images captured by the ISX are also shown.

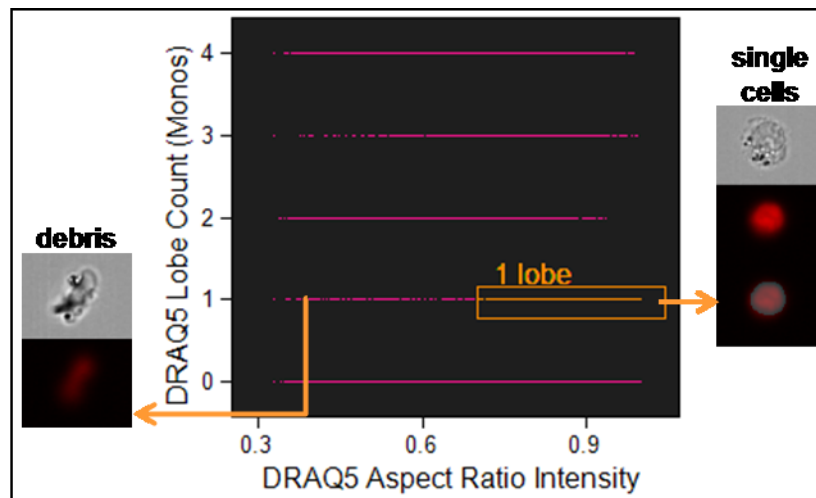


**Figure 4-10:** Scatter plot of lobe count using the mononuclear mask versus DRAQ5 aspect ratio intensity. Single-lobed objects with an aspect ratio intensity of greater than 0.7 were likely to be single cells with a uniformly stained nucleus.

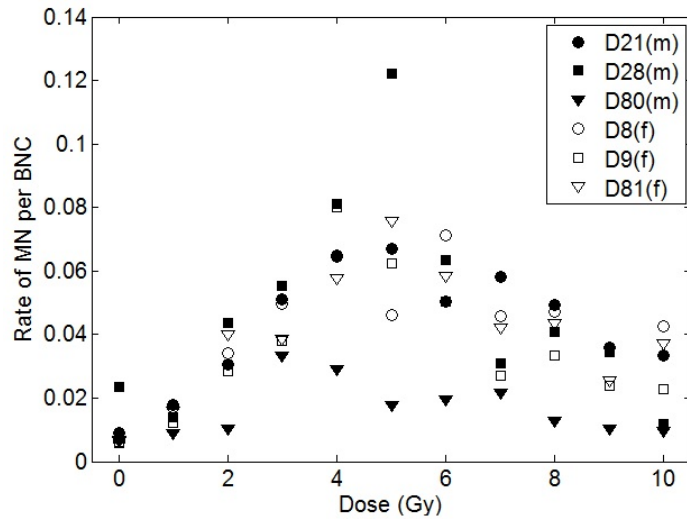
#### 4.4.2. Calibration curves

Six independent experiments with six different donors were carried out using the methods described above. Figure 4-11 presents the ratio of MN per BNC as a function of

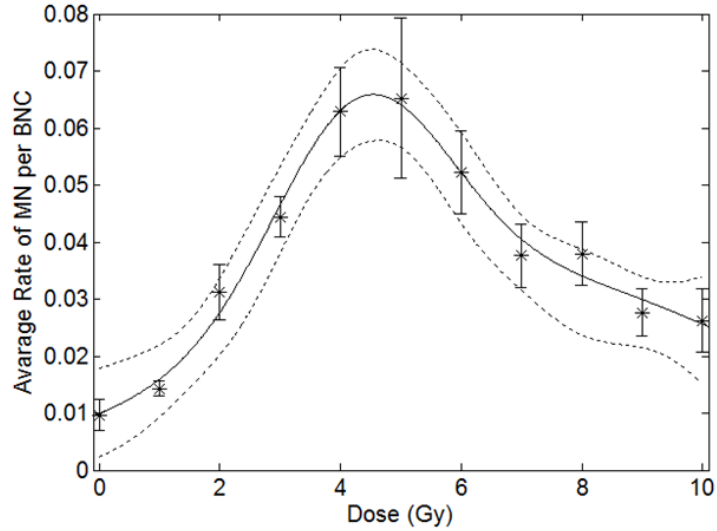
dose for each donor, showing a relatively large individual variability around the 4–6 Gy region. Figure 4-12 shows the weighted average of MN per BNC versus dose for all donors, with the error bars representing the standard error of the mean (SEM). The curve was fit and plotted in Matlab (Mathworks, MA) using a Gaussian of the form:

$$Y = a_1 e^{-((x-b_1)/c_1)^2} + a_2 e^{-((x-b_2)/c_2)^2} \quad (4-6)$$

( $R^2 = 0.985$ ) where all coefficients are determined in Matlab along with the 95% CI. The fit peaks at a value of 4.70 Gy, declines beyond 5 Gy and then begins to plateau.



**Figure 4-11:** Rate of MN per BNC versus dose (Gy) for six donors (3 male (m), 3 female (f)).



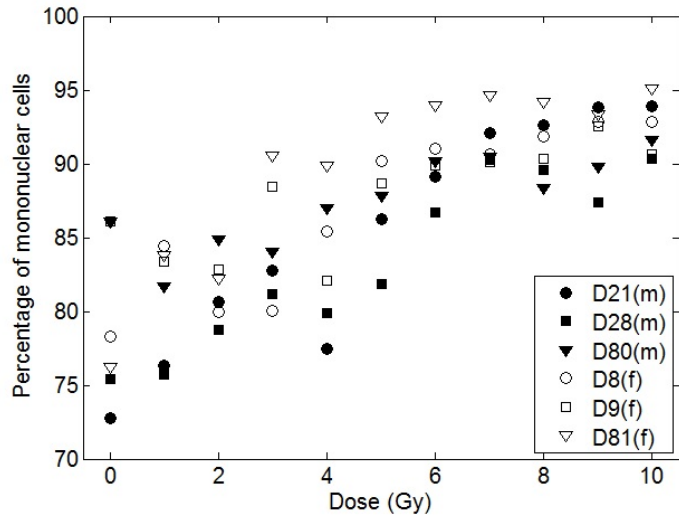
**Figure 4-12:** Average rate of MN per BNC versus dose (Gy) where the stars represent the weighted average of the six donors, the error bars represent the SEM. The data is fit to a summed Gaussian (solid line,  $R^2 = 0.985$ ) and the dashed lines represent the upper and lower 95% CI.

Figure 4-13 represents the percentage of mononuclear cells as a function of dose for each donor. A large spread between donors is evident at doses below 4 Gy. Figure 4-14 shows the weighted average of the percentage of mononuclear cells from all six donors, fit to a quadratic ( $R^2 = 0.954$ ) with error bars representing the SEM. The 95% CI are also plotted. The percentage of mononuclear cells increases from an average of 79.1% at 0 Gy to 92.4% at 10 Gy. Figure 4-15 plots the RI as a function of dose for all six donors illustrating an overall decrease across the full dose range. In the context of this work specifically, the RI is defined as:

$$RI = \frac{(BNC \times 2) + MNC}{N} \quad (4-7)$$

where N is the total number of mononuclear and BNCs scored in each sample (8,32). As with the percentage of mononuclear cells, there are large variations in the RI between

donors at doses below 4 Gy. Figure 4-16 shows the weighted average of the RI from all six donors fit to a quadratic ( $R^2 = 0.963$ ) with the corresponding 95% CI and error bars representing the SEM. The RI decreases from an average of 1.20 at 0 Gy to 1.07 at 10 Gy.



**Figure 4-13:** The percentage of MNCs versus dose for 6 donors (3 male (m) and 3 female (f)). There is a large variation in the percentage of MNCs below 4 Gy.

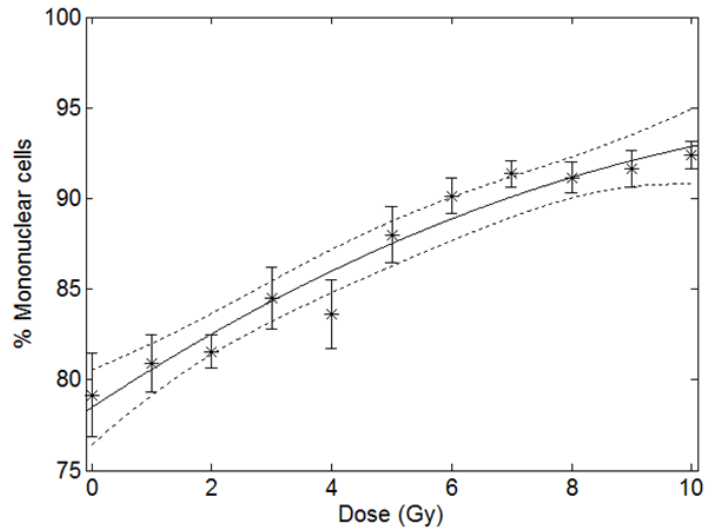


**Figure 4-14:** The weighted average percentage of MNCs versus dose (Gy), where the stars represent the weighted average of the six donors, and the error bars represent the SEM. The data is fit to a quadratic ( $R^2 = 0.954$ ) and the dashed lines represent the upper and lower 95% CI

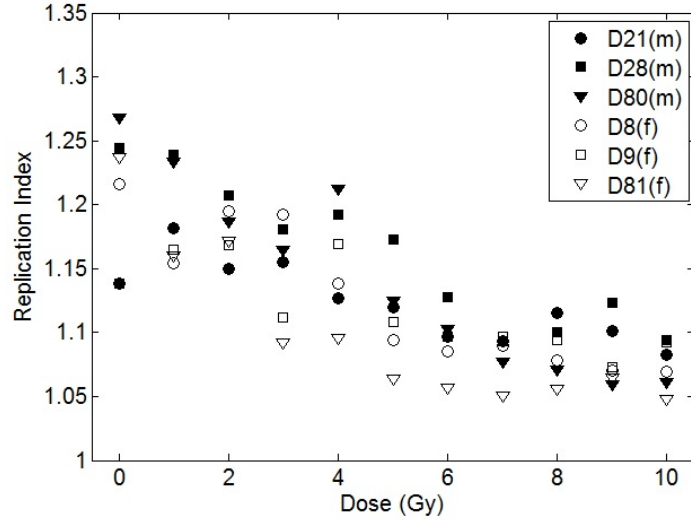


**Figure 4-15:** The RI versus dose for 6 donors (3 male (m) and 3 female (f)). There is a large variation in the RI below 4 Gy.

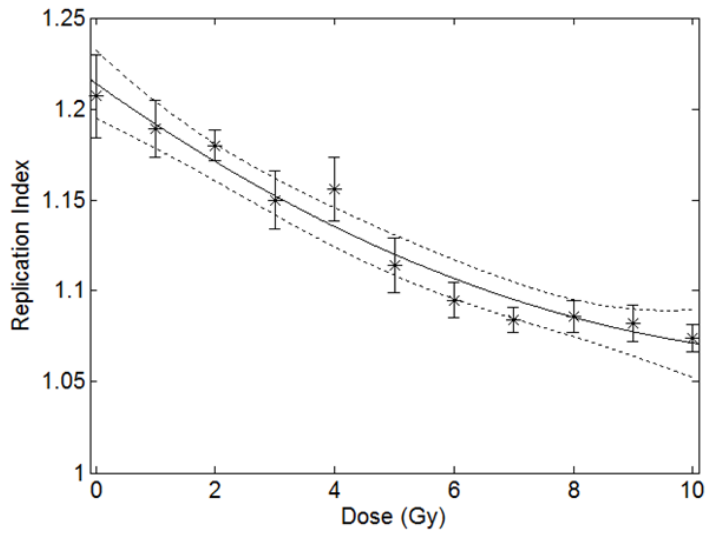


**Figure 4-16:** Average RI versus dose (Gy), where the stars represent the weighted average point at each dose and the error bars represent the SEM. The data is fit to a quadratic ( $R^2 = 0.963$ ) and the dashed lines represent the upper and lower 95% CI.

#### 4.4.3. Receiver operating characteristics

For MN, in both the original and optimized templates, a gate was placed across all populations in Figure 3-9 and events were analyzed visually until 200 cells were classified

as one of the four categories (TP, FP, TN, FN). A TP is a BNC with a correctly masked and counted MN (cells with multiple correctly masked MN were also considered TP events). A FP is a true BNC with a masked, counted object that is not a true MN. A TN is correctly masked BNC with no MN and a FN is correctly masked BNC with a true MN that has not been masked and counted.

For BNCs, in the original template a gate was placed around both the one and two-lobed populations in Figure 3-3, and in the optimized template, the population inside the 1&2 lobes gate in Figure 4-4 were examined. The first 200 events shown in the display area of the IDEAS® template were analyzed. A TP is a correctly masked and counted BNC. A FP is a masked, counted object in the BNC population that is not a true BNC. A TN is a cell that is not a BNC and is not included in the final BNC population so visual confirmation that these events did not appear in the population inside the gate in Figure 4-7 was necessary. Finally, a FN is a true BNC that has been missed by the gating/masking procedure and is not counted in the final BNC population.

#### **4.4.3.1. Receiver operating characteristics for micronuclei**

Table 4-1 gives the TP, FP, TN and FN data for MN at each dose in the original and optimized IDEAS® analysis templates. It can be seen that the number of TP events is approximately the same between both templates at lower and higher doses, but in the dose range between 4-7 Gy more TP events are identified in the optimized template. Additionally, the number of FP and FN events are dramatically reduced in the optimized analysis template. Table 4-2 and Table 4-3 show the values for sensitivity, specificity, precision, negative predictive value and accuracy at each dose point as well as an average value across all dose points for MN in the original and optimized templates respectively. The sensitivity increases, on average, from 52% in the original template to 76% in the

original template and the precision increases, on average, from 73% in the original template to 91% in the optimized template. These improvements are expected based on the reduction in FP and FN events in the optimized template. The specificity, NPV and accuracy reveal marginal improvements when the optimized analysis template is used.

**Table 4-1:** Number of TP, FP, TN and FN MN in the original and optimized IDEAS® analysis template. A total of 200 cells were analyzed at each dose point for one donor (D9).

Dose (Gy)	MN - Original template				MN - Optimized template			
	TP	FP	TN	FN	TP	FP	TN	FN
<b>0</b>	3	0	197	0	2	0	198	0
<b>1</b>	3	1	194	2	2	1	197	0
<b>2</b>	11	0	180	9	9	0	189	2
<b>3</b>	9	4	174	13	7	1	188	4
<b>4</b>	13	9	169	9	17	1	178	4
<b>5</b>	14	9	158	19	17	0	178	5
<b>6</b>	13	6	164	17	15	0	180	5
<b>7</b>	14	6	166	14	11	1	185	3
<b>8</b>	10	4	162	24	8	0	187	5
<b>9</b>	13	11	164	12	9	1	186	4
<b>10</b>	12	5	159	24	4	2	190	4

**Table 4-2:** Sensitivity, specificity, precision, NPV and accuracy, expressed as a percentage, for MN in the original analysis template for all doses.

Dose (Gy)	0	1	2	3	4	5	6	7	8	9	10	Avg
<b>Sensitivity (%)</b>	100	60	55	41	59	42	43	50	29	52	33	<b>52</b>
<b>Specificity (%)</b>	100	99	100	98	95	95	96	97	98	94	97	<b>97</b>
<b>Precision (PPV) (%)</b>	100	75	100	69	59	61	68	70	71	54	71	<b>73</b>
<b>NPV (%)</b>	100	99	95	93	95	89	91	92	87	93	87	<b>93</b>
<b>Accuracy (%)</b>	100	99	96	92	91	86	89	90	86	89	86	<b>91</b>

**Table 4-3:** Sensitivity, specificity, precision, NPV and accuracy, expressed as a percentage, for MN in the optimized analysis template for all doses.

Dose (Gy)	0	1	2	3	4	5	6	7	8	9	10	Avg
<b>Sensitivity (%)</b>	100	100	82	64	81	77	75	79	62	69	50	<b>76</b>
<b>Specificity (%)</b>	100	99	100	99	99	100	100	99	100	99	99	<b>100</b>
<b>Precision (PPV) (%)</b>	100	67	100	88	94	100	100	92	100	90	67	<b>91</b>
<b>NPV (%)</b>	100	100	99	98	98	97	97	98	97	98	98	<b>98</b>
<b>Accuracy (%)</b>	100	100	99	98	98	98	98	98	98	98	97	<b>98</b>

#### 4.4.3.2. Receiver operating characteristics for binucleated cells

Table 4-4 gives the TP, FP, TN and FN data for BNCs at each dose in the original and optimized analysis templates respectively. It can be seen that the number of TP increases at nearly every dose point in the optimized template, especially beyond 3 Gy. Also, the number of FN events is dramatically decreased at all doses in the optimized template. The number of TN events and FP events remain approximately constant between both templates, though there is a slight improvement in the FP events in the optimized template. Table 4-5 and Table 4-6 show the values for sensitivity, specificity, precision, negative predictive value and accuracy at each dose point as well as an average value across all dose points for BNCs in the original and optimized templates respectively.

**Table 4-4:** Number of TP, FP, TN and FN BNCs in the original and optimized analysis templates. A total of 200 cells were analyzed at each dose point for one donor (D9).

Dose (Gy)	BNCs - Original template				BNCs - Optimized template			
	TP	FP	TN	FN	TP	FP	TN	FN
0	11	3	171	18	8	1	189	2
1	11	3	176	10	15	1	179	5
2	25	9	140	26	13	1	181	5
3	10	5	160	25	21	5	167	7
4	5	2	176	17	12	0	185	3
5	8	0	167	25	22	5	169	4
6	8	5	167	20	18	3	176	3
7	14	7	152	27	26	3	168	3
8	10	6	167	17	23	8	164	5
9	6	5	165	24	32	8	151	9
10	4	9	174	13	24	9	159	8

**Table 4-5:** Sensitivity, specificity, precision, negative predictive value and accuracy, expressed as a percentage, for BNCs in the original analysis template for all doses.

Dose (Gy)	0	1	2	3	4	5	6	7	8	9	10	Avg
<b>Sensitivity (%)</b>	38	52	49	29	23	24	29	34	37	20	24	<b>33</b>
<b>Specificity (%)</b>	98	98	94	97	99	100	97	96	97	97	95	<b>97</b>
<b>Precision (PPV) (%)</b>	79	79	74	67	71	100	62	67	63	55	31	<b>68</b>
<b>NPV (%)</b>	90	95	84	86	91	87	89	85	91	87	93	<b>89</b>
<b>Accuracy (%)</b>	90	94	83	85	91	88	88	83	89	86	89	<b>87</b>

**Table 4-6:** Sensitivity, specificity, precision, negative predictive value and accuracy, expressed as a percentage, for BNCs in the optimized analysis template for all doses.

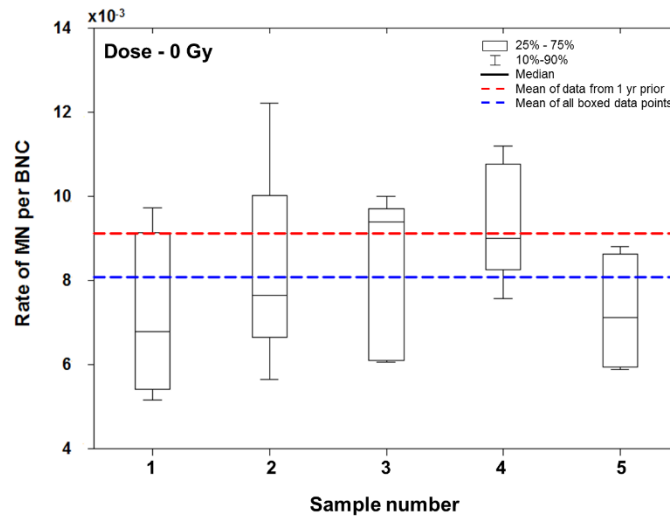
<b>Dose (Gy)</b>	<b>0</b>	<b>1</b>	<b>2</b>	<b>3</b>	<b>4</b>	<b>5</b>	<b>6</b>	<b>7</b>	<b>8</b>	<b>9</b>	<b>10</b>	<b>Avg</b>
<b>Sensitivity (%)</b>	80	75	72	75	80	85	86	90	82	78	75	<b>80</b>
<b>Specificity (%)</b>	99	99	99	97	100	97	98	98	95	95	95	<b>98</b>
<b>Precision (PPV) (%)</b>	89	94	93	81	100	81	86	90	74	80	73	<b>85</b>
<b>NPV (%)</b>	99	97	97	96	98	98	98	98	97	94	95	<b>97</b>
<b>Accuracy (%)</b>	99	97	97	94	99	96	97	97	94	92	92	<b>96</b>

The sensitivity for BNCs increases dramatically from 33% in the original template to 80% on average between the original and optimized templates. Further, the precision increases, on average, from 68% in the original template to 85% in the optimized template. These improvements are once again expected based on the reduction in FP and FN events in the optimized template. The specificity, NPV and accuracy reveal marginal improvements when the optimized analysis template is used similar to the trends seen in the analysis performed on the MN populations.

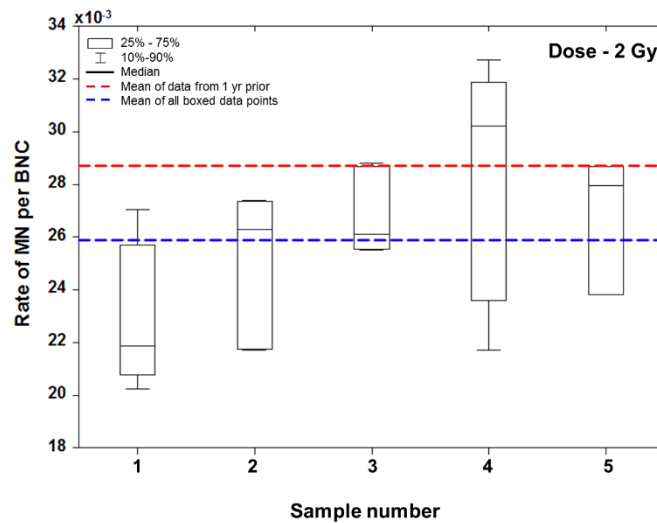
#### **4.4.4. Donor variability in the ISX-CBMN method**

Figure 4-17 and Figure 4-18 show box and whisker plots of the rate of MN per BNC versus dose at 0 Gy and 2 Gy for D21(m) to determine intra-donor variability. Each box in both plots is comprised of five separate data points except for the 5<sup>th</sup> box in Figure 4-17 that only contains four data points due to a loss of sample during data collection. The upper and lower horizontal box lines represent the 25<sup>th</sup> and 75<sup>th</sup> percentile respectively, the solid black horizontal line in each box represents the median of that box and error bars above and below the box represent the 90<sup>th</sup> and 10<sup>th</sup> percentiles respectively. The dashed red line represents the average rate of MN per BNC from donor D21(m) calculated one year prior ( $9.1 \times 10^{-3}$  MN per BNC at 0 Gy and  $2.8 \times 10^{-2}$  MN per BNC at 2 Gy). The dashed blue line represents the average rate of MN per BNC for all data points in the boxes ( $8.1 \pm 0.4 \times 10^{-3}$  MN per BNC at 0 Gy and  $2.6 \pm 0.07 \times 10^{-2}$  MN per BNC at 2 Gy). At both 0 Gy

and 2 Gy, the rate of MN per BNC for the average of all data collected is statistically similar to the rate of MN per BNC obtained one year prior ( $P_{0\text{Gy}}=0.363$ ,  $P_{2\text{Gy}} = 0.992$ ). All data points at both 0 Gy and 2 Gy fall within the upper and lower quartiles.



**Figure 4-17:** Box and whisker plots for 24 data points collected at 0 Gy from donor 21(m). Each box is comprised of 5 data points except for the 5<sup>th</sup> box that contains 4 points. The 25<sup>th</sup> and 75<sup>th</sup> percentile (box edges) as well as the 90<sup>th</sup> and 10<sup>th</sup> percentiles (upper and lower error bars) are shown. The dashed red line shows the rate of MN per BNC for this donor from data collected 1 yr prior and the dashed blue line shows the average rate of MN per BNC from all 24 data points.



**Figure 4-18:** Box and whisker plots for 25 data points collected at 2 Gy from donor 21(m). Each box is comprised of 5 data points and the 25<sup>th</sup> and 75<sup>th</sup> percentile (box edges) as well as the 90<sup>th</sup> and 10<sup>th</sup> percentiles (upper and lower error bars) are shown. The dashed red line shows the rate of MN per BNC for this donor from data collected 1 yr prior and the dashed blue line shows the average rate of MN per BNC from all 25 data points.

Figure 4-19 and Figure 4-20 show box and whisker plots of the rate of MN per BNC versus dose at 0 Gy and 2 Gy for D28(m). Each box is comprised of five separate data points. Again, the upper and lower horizontal box lines represent the 25<sup>th</sup> and 75<sup>th</sup> percentile respectively, the solid black horizontal line in each box represents the median of that box and error bars above and below the box represent the 90<sup>th</sup> and 10<sup>th</sup> percentiles respectively. The dashed red line represents the average rate of MN per BNC from donor D28(m) calculated one year prior ( $2.4 \times 10^{-2}$  MN per BNC at 0 Gy and  $4.4 \times 10^{-2}$  MN per BNC at 2 Gy). The dashed blue line represents the average rate of MN per BNC for all data points in the boxes ( $7.5 \pm 0.3 \times 10^{-3}$  MN per BNC at 0 Gy and  $3.9 \pm 0.08 \times 10^{-2}$  MN per BNC at 2 Gy). At 0 Gy, the rate of MN per BNC obtained one year prior is statistically different ( $P < 0.05$ ) than the average rate of MN per BNC for all data collected. Figure 4-11 demonstrates that the rate of MN per BNC at 0 Gy for the remaining donors are closely distributed about the mean, so the most likely explanation is that the rate of MN per BNC from one year prior is simply an extreme outlier. At 2 Gy, the rate of MN per BNC from one year prior is statistically similar ( $P=0.10$ ) to the average rate of MN per BNC for all data collected. Again, at 2 Gy the data varies more with respect to the mean and all data points at both 0 Gy and 2 Gy fall within the upper and lower quartiles.

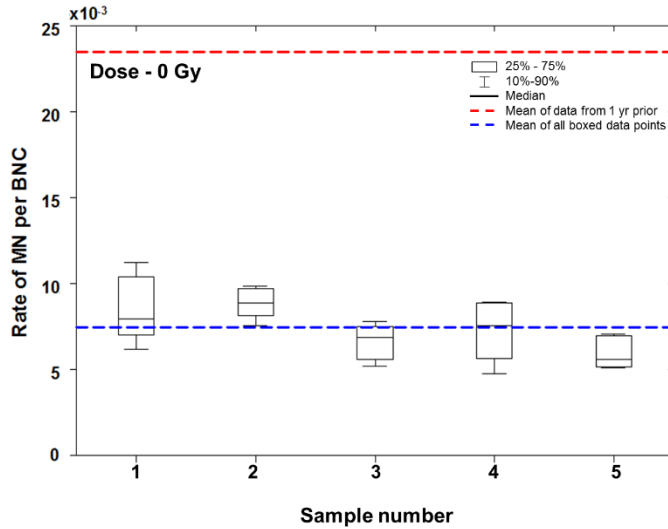


**Figure 4-19:** Box and whisker plots for 25 data points collected at 0 Gy from donor 28(m). Each box is comprised of 5 data points and the 25<sup>th</sup> and 75<sup>th</sup> percentile (box edges) as well as the 90<sup>th</sup> and 10<sup>th</sup> percentiles (upper and lower error bars) are shown. The dashed red line shows the rate of MN per BNC for this donor from data collected 1 yr prior and the dashed blue line shows the average rate of MN per BNC from all 25 data points.

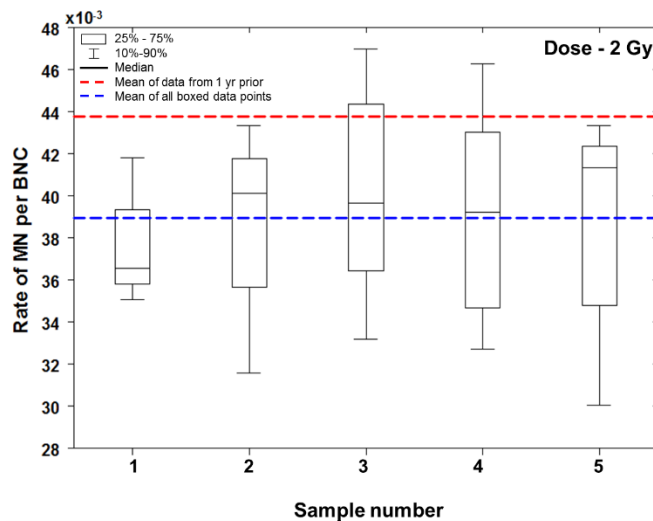


**Figure 4-20:** Box and whisker plots for 25 data points collected at 2 Gy from donor 28(m). Each box is comprised of 5 data points and the 25<sup>th</sup> and 75<sup>th</sup> percentile (box edges) as well as the 90<sup>th</sup> and 10<sup>th</sup> percentiles (upper and lower error bars) are shown. The dashed red line shows the rate of MN per BNC for this donor from data collected 1 yr prior and the dashed blue line shows the average rate of MN per BNC from all 25 data points.

Figure 4-21 shows box plots at 0 Gy and 2 Gy for both donors D21(m) and D28(m) to determine inter-donor variability in the ISX-CMBN method. Each box in Figure 4-21 was

generated by computing the average MN per BNC value for all of the five boxes presented in Figure 4-17-Figure 4-20. For example, at 0 Gy for D21(m), the average of all data points in each box in Figure 4-17 was computed resulting in five values for the rate of MN per BNC. The box at 0 Gy in Figure 4-21 was then created using the average of these five values. This allowed both intra- and inter- variability to be represented together in Figure 4-21.

At 0 Gy, the average rate of MN per BNC from D21(m) is  $8.1 \pm 0.4 \times 10^{-3}$  MN per BNC and  $7.5 \pm 0.3 \times 10^{-3}$  MN per BNC for D28(m), a difference of about 15% and about 20% respectively from the average value of  $9.7 \times 10^{-3}$  MN per BNC shown in the calibration curve presented in Figure 4-12. This result is not surprising given the distribution of the rates of MN per BNC at 0 Gy from six different donors (Figure 4-11). At 2 Gy, the average rate of MN per BNC from D21(m) is  $2.6 \pm 0.07 \times 10^{-2}$  MN per BNC and  $3.9 \pm 0.08 \times 10^{-2}$  MN per BNC for D28(m), a difference of about 15% and about 25% respectively from the average value of  $3.1 \times 10^{-2}$  MN per BNC shown in the calibration curve presented in Figure 4-12. The average rates of MN per BNC at 2 Gy are expected to show differences of this magnitude based on the range of variability in the rates of MN per BNC at 2 Gy from six different donors (Figure 4-11).

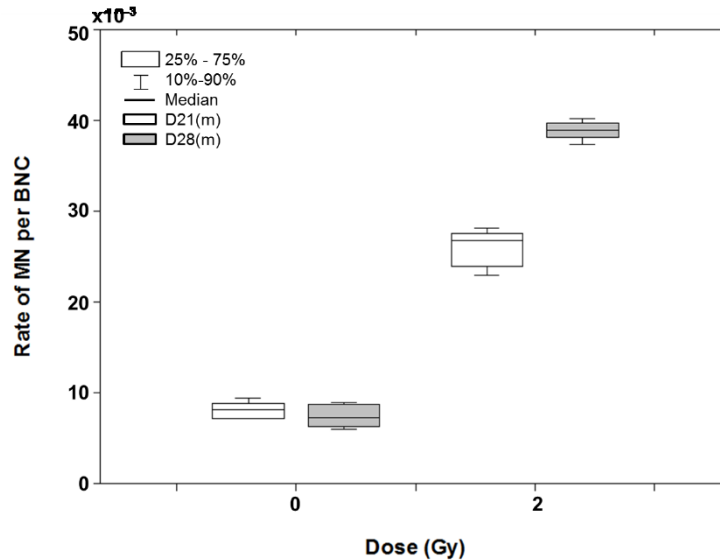


**Figure 4-21:** Box and whisker plot for donors 21(m) and 28(m) at both 0 Gy and 2 Gy illustrating the median, 25<sup>th</sup> and 75<sup>th</sup> percentile (box edges) as well as the 90<sup>th</sup> and 10<sup>th</sup> percentiles (upper and lower error bars).

## 4.5. Discussion

In Chapter 3 the possibility of adapting the traditional CBMN assay to a new imaging FCM method using the ISX, outlining its potential as a biodosimetry tool was described. The aim of the current chapter was to develop a more robust version of the method with a wider dose range and to investigate the possibility of using the percentage of mononuclear cells as well as the RI, in parallel with the rate of MN per BNC, to quantify blinded doses. Figure 4-11 and Figure 4-12 present the rate of MN per BNC as a function of dose for six individual donors and for the weighted average of all six donors, respectively. There is a quadratic dependence from 0 to 4 Gy as expected from biological considerations and historical work on the CBMN assay [32, 33, 35]. Interestingly, however, beyond 5 Gy the rate of MN per BNC declines and appears as though it would plateau beyond 10 Gy. The number of BNCs scored (not shown) also decreases dramatically beyond 5 Gy, by as much as a factor of 3 in some donors. This phenomenon was observed

up to 7 Gy in our previous work [79], and by other authors performing the CBMN assay at very high doses [51, 66, 87]. This decline in BNC frequency appears to be a direct result of the increased difficulty of cells to pass through karyokinesis following very high doses, and therefore results in a decrease in proliferation after 72 h. Additionally, the rate of MN per BNC observed here is approximately one order of magnitude lower than what is traditionally reported with the manual slide-scoring based CBMN method. Other authors employing automated methods to score the CBMN assay have also reported reductions in this parameter [39, 61, 79]. It should be noted that no direct validation of our method against traditional microscope-based manual or automated scoring was performed. Calibration curves using the standard CBMN assay have been generated in our laboratory by McNamee et al. [35] and by several other authors [36, 37, 51, 61, 87]. It is fully acknowledged and accepted that the calibration curve generated for the rate of MN per BNC developed in this work is different in both magnitude and shape when compared to previous publications and when compared to the calibration curves generated using manual slide scoring by McNamee et al [35]. However, all future sample analysis with our method would be performed using the IDEAS® template developed here and dose estimations would be generated from the calibration curves, making cross-calibration to the standard CBMN method unnecessary.

The reduced number of MN observed appears to be related to the strictness of scoring parameters found in automated methods that can be more subjective in manual scoring. In this work, visual inspection of the data revealed that in some cases, MN touching the nuclei were enveloped by the BNC mask and therefore not scored. Also, some very small MN that would be scored manually can be missed due to the area threshold placed on the MN mask. Reducing these types of events so that more MN were scored was only partially possible through optimization of the mask parameters. Reducing the area of the BNC

mask such that it would not envelope a MN in close proximity sometimes caused too many smaller non-valid nuclei to be masked and incorrectly scored. By the same token, reducing the area of the MN mask to count small nuclei presented two problems, the first being that the size of MN being scored would then fall outside of the guidelines presented by Fenech et al. [67], the second being that reducing the size of the MN mask caused smaller debris to be falsely counted as MN. Further, in the three dimensional system used in the ISX, some MN may be hidden behind a nucleus and cannot be visualized, or MN may be at a different depth of field than the nuclei and are not intense enough to be clearly identified and masked. In an attempt to increase MN frequency, hypotonic swelling of the cells using a KCl solution was attempted before and after application of the BD FACS™ Lysing Solution. No improvement in the MN frequency was observed. Therefore, as one of the strengths of our method is the minimal number of sample processing steps, it was ultimately decided to forego the use of a hypotonic swelling step. Figure 4-11 also reveals a large inter-individual variation between donors typically in the range of 4–6 Gy but also across the whole dose range, specifically in the case of Donor 80(m). This variation between donors has been noted in other works across a wide range of doses. Wojcik et al. [88] examined the sensitivity of the CBMN assay at doses below 1 Gy and noted a variation in the rate of MN per BNC among eight donors to be as high as 30% from the average. Lyulko et al. [66] also reported large variations, as high as 50% between 4 Gy and 6 Gy among seven donors. Kacprzak et al. [87] examined the variation in the rate of MN per BNC in five donors up to 20 Gy. At a dose of 5 Gy they report standard deviations larger than we present here. By averaging all the data, the calibration curve accounts for individual radiosensitivity and further underscores the need for a multi-parameter approach to biodosimetry using the CBMN assay.

The relation between the percentage of mononuclear cells and dose is presented in Figure 4-13 and Figure 4-14. The percentage of mononuclear cells increases quadratically from 79.1% at 0 Gy to 92.4% at 10 Gy. This trend has been observed in other research with some variation at lower doses, but seems to plateau around 90% at 10 Gy and beyond [51, 87]. Figure 4-13 shows a large variation in the percentage of mononuclear cells between donors at lower doses (about 10–15%), that becomes much smaller at higher doses (about 5%). These deviations are slightly better than those observed by Kacprzak et al. [87] who report a variation of about 30% at 0 Gy and about 10% at 10 Gy. The large fraction of mononuclear cells at very high doses is expected as the proliferation of cells slows dramatically and very few pass through even a single mitosis, hence the population is largely composed of single, undivided cells [51]. The large variation in this parameter at low doses is likely due to differing cell division rates between donors, making the percentage of mononuclear cells a useful dose prediction parameter at higher doses (above 5 Gy). Müller and Rode report that the percentage of mononuclear cells ranges from about 50% at 0 Gy to about 95% at 10 Gy [51]. While the authors indicate that 354,033 total lymphocytes were analyzed, no explicit values for the number of mononuclear cells scored from any donors are provided. Kacprzak et al. report that the percentage of mononuclear cells ranges from about 60% at 0 Gy to about 90% at 10 Gy [87]. In this work, the authors do provide the number of mononuclear cells scored for each donor however, these values are relatively low ranging from 201 to 487. The results presented by Kacprzak et al. also indicate a relatively large standard error of the mean in non-irradiated cultures, and show that the percentage of mononuclear cells ranges from about 40% to about 80% [87]. Our method possesses the capability to score about 15,000 mononuclear cells per sample. For the six donors used in our study, with 11 dose points per donor this translates to an approximate total of one million mononuclear cells scored

in this study. Therefore, with the increased statistics afforded by our method and the apparent significant variation in the percentage of mononuclear cells in non-irradiated samples shown here and by Kacprzack et al. [87], it is entirely possible that previous publications have underestimated the percentage of mononuclear cells in non-irradiated samples and that the true value of this parameter is indeed as high as about 75–80%. It should be noted that the use of both the percentage of mononuclear cells, as well as the rate of MN per mononucleated cell in the CBMN assay should not be used as independent predictors of dose. These parameters are typically only useful if the culture conditions remain constant between experiments and between laboratories. It should be cautioned that while attempts are made to maintain constant culture and processing conditions across all experiments, slight variations in the environment are inevitable which may impact the frequency of MNCs, BNCs as well as multi-nucleated cells. Additionally, the time in which mononuclear cells with MN appear in the blood following exposure to ionizing radiation is not yet well defined [88]. As a result, the percentage of mononuclear cells should only be used as an additional parameter in conjunction with the rate of MN per BNC where high doses are suspected.

Figure 4-15 and Figure 4-16 shows the relation between the RI and dose. The average RI decreases with dose from 1.21 at 0 Gy to 1.07 at 10 Gy. This dose-dependent decrease in RI has been observed in other research with similar variations at lower doses. Figure 4-15 illustrates that this variation between 0 Gy and 5 Gy is 10-15%, the same variability as reported by Kacprzak et al. [87]. At higher doses, the deviation in the RI between donors follows the same trend as the percentage of mononuclear cells, dropping off to about 5% at 10 Gy. Overall, the decrease in RI with increasing dose is expected for the same reasons that the percentage of mononuclear cells increases with dose. From the RI equation, the numerator is directly dependent on the number of mononuclear cells

so, as this parameter increases with dose and the number of BNCs declines, the RI value is expected to decrease toward a value of 1. Additionally, decreasing standard deviation with increasing dose makes the RI another effective parameter when attempting to identify doses beyond 4 Gy.

The results of this work and other publications [66, 87] indicated that the rate of MN per BNC follows a Gaussian distribution across the dose range from 0 to 10 Gy, plateauing at higher doses. This makes correctly distinguishing between low and high doses virtually impossible based on this single parameter alone, and a method for making this distinction is essential for biodosimetry. Both the percentage of mononuclear cells and the RI show a clear quadratic relation with dose, and we posit that by combining these three parameters, a better estimation of dose can be provided than with any one parameter alone. In the context of triage biodosimetry, the 72 h incubation time required for the CBMN assay, combined with the time required for slide making and counting MN, BNCs, and mononuclear cells, makes a multi-parameter analysis difficult to perform when rapid and accurate dose estimations are needed. However, combining the speed of the ISX imaging flow cytometer and the automated analysis template developed in IDEAS®, a multi-parameter dose estimation can be obtained within about 2 h following the culture time. The use of the same analysis template for every sample virtually eliminates any user bias that is inherently present in manual CBMN slide scoring. Additionally, the template can be easily shared with other laboratories that have an ISX and the IDEAS® software, which would be beneficial for inter-laboratory comparisons of the method, and in a large-scale radiological event where multiple laboratories are involved in estimating doses for large numbers of casualties.

Several recent publications have reported on a cell preparation procedure to perform the CMBN assay using traditional FCM that involves using a detergent lysing procedure

for liberating MN and nuclei [75, 89, 90]. While this method is ideal for performing the CBMN assay on a traditional flow cytometer, there are several major limitations that our method overcomes when adapting the CBMN assay to an imaging cytometry method for radiation biodosimetry. This detergent lysis method described by Avlasevich et al. [75] requires 1.5 h of incubation time following the addition of two separate solutions that must be prepared, resulting in the lysis of all cells in the sample. For high throughput biodosimetry, rapidity of the assay is important, and the use of a product such as BD FACS™ Lysing Solution is desirable. The BD FACS™ Lysing Solution can be added directly to a cell solution, requires only a 10 min incubation time and lyses only red blood cells, leaves the lymphocytes completely intact. Thus, while the detergent lysis method is applicable for traditional FCM measurements of MN and nuclei, it is less than ideal for applications in biodosimetry. Using the protocol developed in this work, the 11 samples per experiment were processed in approximately 1 h following culture by two people working simultaneously in the laboratory. Another 10–20 min was required for staining with DRAQ5 and data collection on the ISX where 150–200 events per second can be imaged and stored in a data file. While the gating strategy removes many unwanted events from the final population, the number of BNCs scored is typically greater than 2,000 at lower doses (0-4 Gy), nearly double the number counted by microscope-based CBMN. The number of BNCs falls off to approximately 1,000 at higher doses (8-10 Gy) as expected from the reduction in proliferation, but is still significantly more BNCs than can be scored manually at such high doses, and in a fraction of the time. As mentioned previously, limiting the culture time to 72 h is the most likely explanation for the decline in BNCs at such high doses. It is reasonable to assume that this argument can be extended to the decrease in MN frequency as well. One could speculate that a longer culture time would generate more BNCs and MN, but this would directly contradict the strength of our

method which is to obtain a dose estimation as quickly as possible following the culture time. In fact, future work to optimize our method will investigate reducing the culture time to as little as 48 h to be directly comparable to the dicentric assay, the current gold standard in radiation biodosimetry.

Typical data acquired through FCM techniques requires colour compensation, which subtracts a portion of one detector's signal from another, leaving only the desired signal. In the method developed for this work, DRAQ5 is the only fluorescent dye used to stain the nuclear material while BF images are used to delineate the cytoplasm. One of the main goals of triage biodosimetry is to process samples as accurately and as rapidly as possible, so by using only DRAQ5 the need for color compensation is eliminated and the amount of processing time is further reduced. The use of cytoplasm stains and cell surface markers was investigated previously, and offered no enhancement over the gating strategies developed using the BF images [79].

Hall and Giaccia provide a timeline on the appearance of the symptoms of the acute radiation syndrome [16]. The distinction must be made between symptoms as a result of exposure and the eventual cause of death that, at doses below the threshold for lethality (< 8 Gy), manifest after a latency period. Mild doses (below 2 Gy) are not considered to be life-threatening and typically do not require hospitalization. In this case rapid biodosimetry is not essential. However, doses in the moderate to very severe range (2–8 Gy) will require hospitalization for symptoms that typically include fever, infection, fatigue, vomiting, and possibly diarrhea. These symptoms are not life-threatening and can be controlled. The significant threat to life comes from depression of whole blood elements during what is known as the latent period following initial exposure. This latency period ranges from about 18 days for mild doses around 2 Gy to about 7 days for more severe doses around 6 Gy. This is where a rapid, high throughput method of dose estimation

becomes very valuable to healthcare officials. The method presented in this work can provide dose estimations in about 2–3 h following the 72 h culture time, meaning that on the third or fourth day after initial exposure dosimetric information can be provided to clinicians who can begin the appropriate treatment. The true strength of our method is realized when considering a large number of casualties who have received doses between the mild and severe thresholds. By being able to provide accurate dose estimations for many patients within the first week of exposure, appropriate and possibly life-saving treatment can begin during the latent period.

The original data analysis template in IDEAS®, presented in section 3.3.7, was modified significantly to better identify MN and BNCs while eliminating more debris from the final scored population. Examination of the receiver operating characteristics presented in Table 4-2 and

Table **4-3** revealed that the specificity for MN was very high in both the original and optimized templates indicating that TN events (BNCs with zero MN) were well-identified. As seen by the reduction in FP events, the optimized template improved on the correct identification of true MN. The NPV and accuracy were marginally increased in the optimized template, again reinforcing the improvement observed in the detection of TN events. The most significant increases in the ROC parameters for MN were in sensitivity and precision, illustrating that the optimized template better identified TP and TN events while reducing the frequency of FN events. For BNCs, the most dramatic improvement between the original and optimized templates was the reduction in the number of FN events (Table 4-4) that markedly increased the sensitivity and the NPV as demonstrated in Table 4-5 and Table 4-6. The frequency of FP BNCs also decreased at lower doses in the optimized template but increased at higher doses, likely as a result of the significant DNA damage that occurs at high doses and the subsequent reduction in BNCs. The NPV

and accuracy for BNC identification also showed and increase between the original template and the optimized template, albeit marginal. Finally, as with the MN population, the sensitivity and precision with which BNCs are identified decreased at higher doses in both the original and optimized template.

In order to examine the variability of the rate of MN per BNC for a single donor over time as well as in the ISX-CBMN method itself, whole blood samples from the same donor at 0 Gy and 2 Gy were examined about 1 yr apart. Figure 4-17 and Figure 4-18 show that for samples from D21(m), all of the data points fall within the 25<sup>th</sup> and 75<sup>th</sup> percentiles at both doses. Additionally, the rate of MN per BNC at 0 Gy from one year prior fell within the 10<sup>th</sup> and 90<sup>th</sup> percentiles in four of the five boxes in Figure 4-17 and at 2 Gy, the rate of MN per BNC from one year prior fell within the 10<sup>th</sup> and 90<sup>th</sup> percentiles in three of the five boxes in Figure 4-18. Figure 4-19 and Figure 4-20 show that for samples from D21(m), all of the data points fall within the 25<sup>th</sup> and 75<sup>th</sup> percentiles at both doses. However, the rate of MN per BNC at 0 Gy from one year prior fell well outside the 90<sup>th</sup> percentile and at 2 Gy, the rate of MN per BNC from one year prior fell outside the 90<sup>th</sup> percentile in all but two of the five boxes in Figure 4-20. Given the highly symmetric nature of the data about the mean of all boxed data points, as well as the data shown in Figure 4-11 that indicated that the rate of MN per BNC at 0 Gy for the remaining donors was closely distributed about the mean, it can be assumed that the data obtained from the previous date of donation at 0 Gy was simply an extreme outlier. This could be due to a number of factors including, but not limited to, culture contamination, the overall health of the donor at the time of blood draw or simply a variation in background rates of MN. For both donors, all data points are concentrated around the mean value at 0 Gy indicating a low variability in the background rates of MN. This same trend has been observed in a number of other studies where the CBMN assay was performed with multiple donors using both manual and automated

CBMN methods [35, 37, 61, 87, 91]. At 2 Gy, the inter-donor variability is slightly larger than at 0 Gy that was expected since the rate of MN per BNC is now dependent on the individual differences in response to radiation and not just background rates of MN, a trend that was also observed by Thierens et al. [91]. Overall, these results revealed low intra-donor variability and illustrated that both the sample processing procedure and the data analysis using the IDEAS® template in the ISX-CBMN method were reproducible. Moreover, the inter-donor variability between samples processed from two different donors at 0 Gy was relatively low, indicating that the method detects a consistent rate of background MN that was comparable to previously published studies on the CBMN assay [35, 37, 61, 87, 91]. This becomes important for future work with the ISX-CBMN method, specifically in estimating doses in irradiated samples as the rate of MN per BNC can be assumed to result directly from radiation exposure and not any variations in background MN.

This chapter presents a multi-parameter, imaging FCM based method for performing high throughput triage biodosimetry using the CBMN assay. These results build upon our previous work by extending the dose range to 10 Gy, as well as by including the percentage of mononuclear cells and the RI as additional parameters to more accurately predict doses within about 2 h following culture.

## **5. VALIDATION OF THE CYTOKINESIS-BLOCK MICRONUCLEUS ASSAY USING IMAGING FLOW CYTOMETRY FOR HIGH THROUGHPUT TRIAGE RADIATION BIODOSIMETRY**

### **5.1. Summary**

This chapter is based on the manuscript *Validation of the Cytokinesis-Block Micronucleus Assay Using Imaging Flow Cytometry for High Throughput Triage Radiation Biodosimetry* submitted to Health Physics (March 2015). This work investigates the feasibility reducing the CBMN culture time from 72 h to 48 h and reducing the initial blood culture volume from 2 mL to 200  $\mu$ L. Results indicate that dose estimations can be generated to within 0.5 Gy of the delivered dose after only 48 h of culture time with an initial blood volume of 200  $\mu$ L. The adaptation of the CBMN assay to an imaging FCM method allows for a significant reduction in the culture time/volume requirements and greatly increases its applicability in high throughput triage radiation biodosimetry.

Additional sections detailing the methods used to determine the minimum blood volume required to generate sufficient BNCs ( $> 500$ ), 0-10 Gy dose response calibration curves for the rate of MN per BNC for the 72 h, 200  $\mu$ L; 48 h, 2 mL and 48h, 200  $\mu$ L culture conditions as well as dose estimations on all blinded samples examined between 0-10 Gy are presented.

### **5.2. Introduction**

Recent advances in automated slide scoring for the CBMN assay allows for more rapid scoring of individual samples and therefore increasing throughput. Despite these advances, the CBMN has several drawbacks as outlined by Fenech [92], who stated that

the development and validation of a protocol that reduces the culture time to 48-56 h should be theoretically possible, as a sufficient number of lymphocytes would have completed at least one nuclear division. In addition to culture time reduction, Fenech also suggested that miniaturization of the assay using a drop of blood would further transform the assay into a minimally-invasive procedure that could be used for faster screening of a large number of individuals.

Koksal et al. [93] were among the first to demonstrate that following addition of cytochalasin B 24 h after initial incubation, the yield of BNCs did not differ significantly from cultures that were harvested at 56 h when compared to cultures harvested at 72 h. However, they did conclude that an incubation time of only 48 h was too short to score a sufficient number of BNCs and MN using standard microscopy. Lee et al. [94] illustrated that an incubation time of 64 h yielded statistically equivalent numbers of BNCs and MN when compared to the standard 72 h incubation. Recently, with the adaptation of the CBMN assay to an imaging FCM method [79], nearly 2000 BNCs can be scored in as little as 15 min. As this method allows for many cells to be analyzed, it is possible that a sufficient number of BNCs could be scored after only 48 h of culture time to generate accurate dose estimations, something that is challenging using traditional microscope-based forms of the assay.

In addition to the 72 h culture time requirement, typical standard CBMN protocols involve culturing 500  $\mu$ L to 2 mL of peripheral blood in a large volume of culture medium (5-20 mL) [35, 66, 87]. This can be problematic for several reasons including the required use of more reagents, which can be costly. Furthermore, a reduction in the initial blood culture volume may eliminate the need for peripheral blood sampling using venipuncture, which is invasive and may not be possible depending on the nature of the emergency and the state of the patient. Lee et al. [95] performed the CBMN assay using 500  $\mu$ L of capillary

blood obtained from a finger stab and found no statistically significant difference in MN and BNC frequency when compared to blood obtained through venipuncture.

This chapter validates the accuracy of the ISX-CBMN method to estimate blinded doses using standard culture time (72 h) and blood volume (2 mL) conditions. This chapter also investigates the accuracy of the ISX-CBMN method to estimate blinded doses when reducing the culture time from 72 h to 48 h as well as reducing the initial blood volume from 2 mL to 200  $\mu$ L that would improve the applicability of the CMBN assay as a high throughput triage biodosimeter.

### **5.3. Materials and methods**

#### **5.3.1. Determination of minimum culture volume**

The minimum volume of whole blood that could be cultured to yield a sufficient number of BNCs was determined by processing samples with the ISX-CBMN method with initial volumes ranging from 100  $\mu$ L to 2 mL. Whole blood was collected from one anonymous donor (D8(f)) and irradiated to 2 Gy using the irradiation protocol outlined in section 3.3.1. Samples were then aliquoted to the volumes indicated in Table 5-1, cultured and processed using the ISX-CBMN method as outlined in section 3.3.3. Each sample was then run on the ISX and 100,000 events were collected for the 500  $\mu$ L, 750  $\mu$ L, 1 mL and 2 mL cultures. Only 50,000 events could be collected for the 100  $\mu$ L, 200  $\mu$ L and 300  $\mu$ L cultures as the sample concentration limited the collection speed. Sample concentrations decreased as initial blood volumes decreased since all samples were resuspended in the same final volume (100  $\mu$ L) before processing on the ISX. All data was then processed using the IDEAS® template described in section 4.4.1.

**Table 5-1:** The number of BNCs scored at each culture volume using the IDEAS® template

<b>Culture volume</b>	<b>Number of BNCs scored</b>
100 µL	316
200 µL	1124
300 µL	1415
500 µL	1548
750 µL	2922
1 mL	3142
2 mL	3090

Table 5-1 indicated that culturing as little as 200 µL of whole blood initially, resulted in 1124 BNCs being scored, but once the volume was reduced below this volume to 100 µL, only 316 BNCs were scored. As the number of BNCs decreases with dose, the number of scorable BNCs would fall below 200, which is the recommended number of BNCs to be scored for triage biodosimetry [35]. Therefore, the minimum volume of whole blood that could be cultured to generate a sufficient number of BNCs using the ISX-CBMN method was determined to be 200 µL.

### **5.3.2. Blood collection, irradiation and CBMN assay for calibration curves**

Blood was collected by venipuncture with informed consent from healthy anonymous donors (3 males and 3 females between the ages of 27 and 48) as described in section 3.3.1. For all calibration curves, irradiations were performed according to the procedure described in section 3.3.1. Each irradiated blood sample was then split into two 200 µL volumes and two 2 mL volumes and the CBMN assay was performed as described in section 3.3.3. For initial blood volumes of 2 mL, this achieved 20 mL cultures in 25 cm<sup>2</sup> vented flasks and for initial blood volumes of 200 µL, this achieved 2 mL cultures in 3 mL

wells of a 24-well plate. Four separate culture conditions were achieved: (a) 2 mL blood volume at 72 h incubation, (b) 2 mL blood volume at 48 h incubation, (c) 200  $\mu$ L blood volume at 72 h incubation and (d) 200  $\mu$ L blood volume at 48 h incubation, with (a) being the standard CBMN culture volume and incubation time conditions.

### **5.3.3. Blood collection, irradiation and CBMN assay for validation with blinded samples**

Twenty blood samples were collected from five healthy anonymous donors (males between the ages of 34 and 56 years of age) in 6 mL lithium-heparinized Vacutainer® tubes. All donors were asked to have the same age, health and historical radiation exposure criteria as described above. Each whole blood sample was then irradiated to a known dose between 0-10 Gy using the procedure described in section 3.3.1 and then blinded before culture. The doses were 0, 0.5, 0.7, 1.3, 1.7, 2.4, 2.9, 3.1, 3.9, 4.2, 5.0, 5.4, 5.8, 6.1, 6.8, 7.5, 7.9, 8.4, 9.4 and 9.8 Gy. Each blood sample was split into two 200  $\mu$ L volumes and two 2 mL volumes and CBMN culture was performed as described in section 3.3.3.

### **5.3.4. Data collection on the ImageStream<sup>x</sup> and data analysis**

All samples were processed and run on the ISX according to the procedure described in section 4.3.3.2. For the calibration curves, approximately 100,000 events were collected per sample from the 2 mL blood volumes. For the 200  $\mu$ L blood volumes, the number of total events that could be collected was limited by the sample concentration and therefore, only 50,000 events were collected from each sample. For the blinded samples, events were collected for 5, 10, 15, 20, 25, 30, 35 and 40 min. Data was collected this way such that when performing the analysis, a minimum collection time to estimate the delivered

dose to within  $\pm 0.5$  Gy could be determined. All data was processed using IDEAS® as described in section 4.3.3.2. The number of BNCs and MN were stored and exported to Microsoft Excel 2013, Sigmaplot 11.0 (Systat Software Inc.) and Chromosome Aberration Calculation Software (CABAS v2) [96] for analysis.

## **5.4. Results**

### **5.4.1. Dose response calibration curves and estimation of blinded doses between 0-10 Gy**

Calibration curves for the rate of MN per BNC, the percentage of MNCs and the RI were generated from 0-10 Gy for each of the four culture conditions described above. Each curve appeared similar to the curves shown in Figure 4-12, Figure 4-14 and Figure 4-16. To illustrate this, the calibration curves for the rate of MN per BNC for the 48 h, 2 mL; 72 h, 200  $\mu$ L and the 48 h, 200  $\mu$ L culture conditions are shown in Figure 5-1, Figure 5-2 and Figure 5-3 respectively. For the 48 h, 2 mL condition (Figure 5-1) the data was fit to a summed Gaussian as described in section 4.4.2 and the fit peaks at a value of 3.59 Gy, nearly 1 Gy lower than the 72 h, 2 mL condition. Additionally, the rate of MN per BNC plateaus at a lower dose than the 72 h, 2 mL condition.

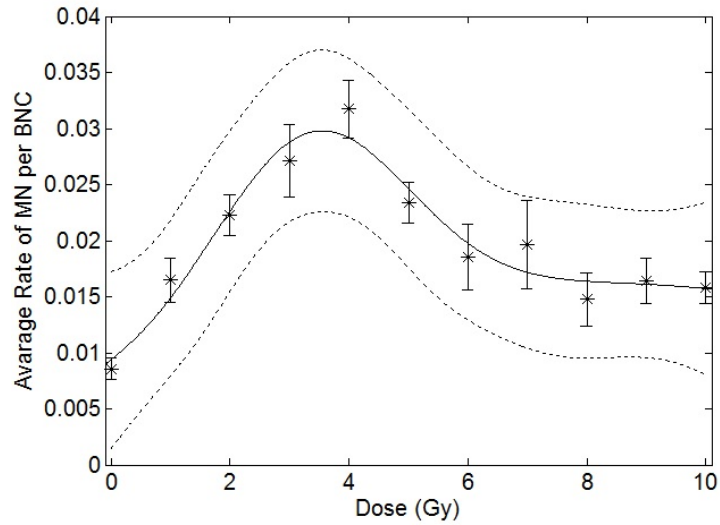


**Figure 5-1:** Average rate of MN per BNC versus dose (Gy) for the 48 h, 2 mL culture condition. The stars represent the weighted average of the six donors, the error bars represent the SEM. The data is fit to a summed Gaussian (solid line,  $R^2 = 0.879$ ) and the dashed lines represent the upper and lower 95% CI.

For the 72 h, 200  $\mu$ L and 48 h, 200  $\mu$ L conditions (Figure 5-2 and Figure 5-3) the data was fit to a rational function of the form:

$$Y = \frac{ax^2 + bx + c}{x^2 + dx + e} \quad (5-1)$$

as summed Gaussian functions provided a poor fit in both cases as determined by the  $R^2$  values. All coefficients were determined in Matlab along with the 95% CI. Despite fitting to a different function, the fit for the 72 h, 200  $\mu$ L culture condition matches well to the Gaussian fit for the 72 h, 2 mL culture condition shown in Figure 4-12. The fit peaks at 4.29 Gy, declines past 5 Gy and would plateau beyond 10 Gy. For the 48 h, 200  $\mu$ L culture condition the fit is more symmetric about the maximum value (3.02 Gy), declines quickly beyond 4 Gy and appears to begin plateauing for the reasons discussed above for the 48 h, 2 mL culture condition.

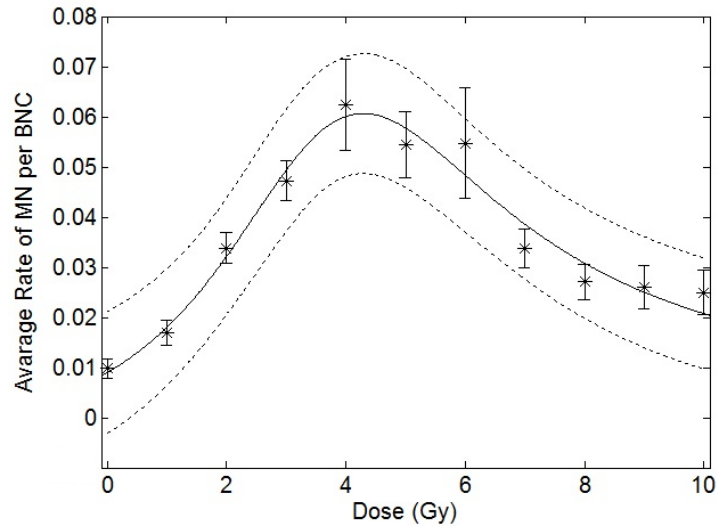


**Figure 5-2:** Average rate of MN per BNC versus dose (Gy) for the 72 h, 200 µL culture condition. The stars represent the weighted average of the six donors, the error bars represent the SEM. The data is fit to a rational function (solid line,  $R^2 = 0.957$ ) and the dashed lines represent the upper and lower 95% CI.

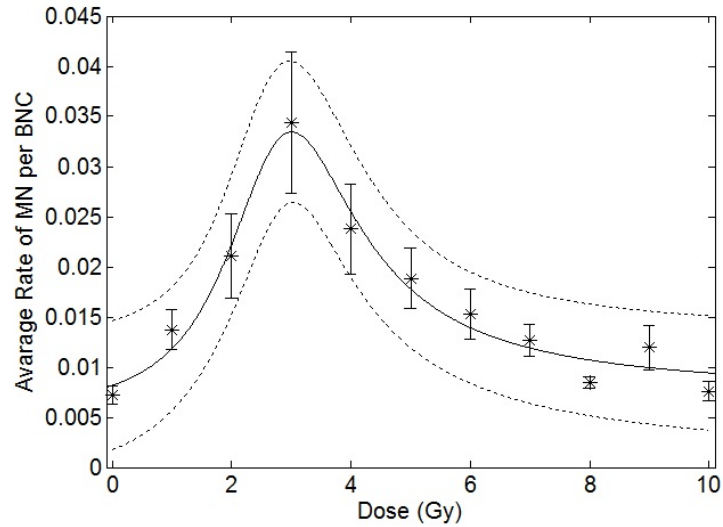


**Figure 5-3:** Average rate of MN per BNC versus dose (Gy) for the 48 h, 200 µL culture condition. The stars represent the weighted average of the six donors, the error bars represent the SEM. The data is fit to a rational function (solid line,  $R^2 = 0.962$ ) and the dashed lines represent the upper and lower 95% CI.

#### 5.4.2. Estimation of blinded doses between 0-10 Gy

The number of MN, BNCs and MNCs were obtained from the IDEAS® software template for all 20 blinded samples for each culture condition at each collection time (5-40 min at 5 min increments). These values were then entered into a Matlab code that determined the two possible dose estimates based on the rate of MN per BNC as well as the dose estimates based on the percentage of MNCs and the RI. For example, Figure 5-4 shows a plot of the rate of MN per BNC versus dose used to estimate a blinded dose of 1.7 Gy using standard culture conditions (72 h, 2 mL). It can be seen that each value for the rate of MN per BNC would generate two possible dose estimations, except for the maximum rate of 0.0649 that results in a dose estimation of 4.29 Gy and below a rate of 0.0267 (a dose of 1.9 Gy) that would only return one dose estimate. The red circles highlight the intersection points between the rate of MN per BNC and the summed Gaussian (2.1 Gy and 9.3 Gy). The dashed lines represent the 95% CI and the error bars represent the SEM. The blue horizontal lines illustrate the lower and upper range on the estimated dose based on the 95% CI. For the 2.1 Gy dose estimate the range is 1.7 Gy to 2.5 Gy and for the 9.3 Gy dose estimate the range is 7.2 Gy to >10 Gy. Figure 5-5 and Figure 5-6 show plots of the percentage of MNCs versus dose and RI versus dose respectively that were used to estimate the same blinded dose using the same culture conditions. Again, the dashed lines represent the 95% CI and the error bars represent the SEM. For the percentage of MNCs, the dose estimate is 2.3 Gy with a range of 1.6 Gy to 2.9 Gy while for the RI, the upper dose estimate is also 2.3 Gy with a range of 1.8 Gy to 2.9 Gy. Based on this analysis using the three plots, the lower dose from Figure 5-4 (1.7 Gy) was chosen to be the correct one.

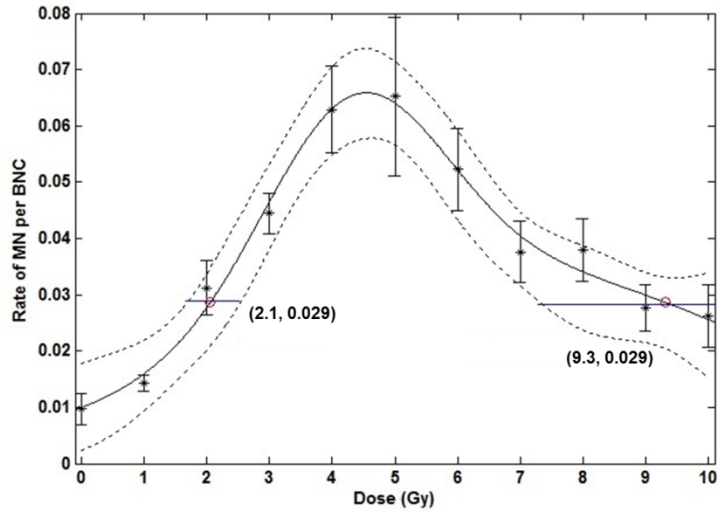


**Figure 5-4:** Dose estimations based on the rate of MN per BNC. The red circles highlight the points where the rate of MN per BNC intersect the summed Gaussian fit and the blue line indicates the lower and upper uncertainties on the dose estimate based on the 95% CI. The values in brackets are the dose estimation and rate of MN per BNC at both points. The dashed lines represent the 95% CI while the error bars represent the SEM.

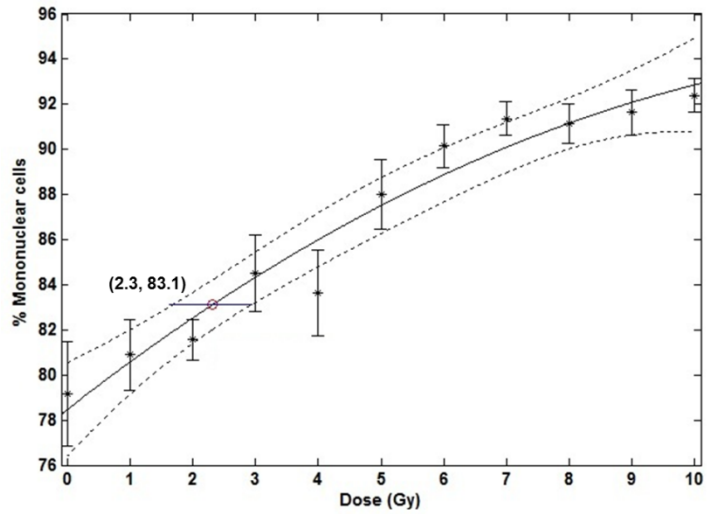


**Figure 5-5:** Dose estimation based on the percentage of MNCs. The red circle highlights the point where the percentage of MNC value intersects the quadratic fit and the blue line indicates the lower and upper uncertainties on the dose estimate based on the 95% CI. The values in brackets are the dose estimation and percentage of MNCs at the intersection point. The dashed lines represent the 95% CI while the error bars represent the SEM.

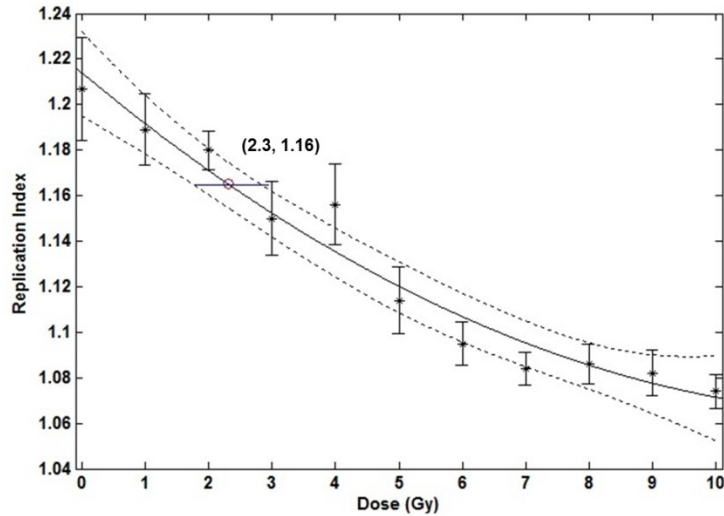


**Figure 5-6:** Dose estimation based on the RI. The red circle highlights the point where the RI value intersects the quadratic fit and the blue line indicates the lower and upper uncertainties on the dose estimate based on the 95% CI. The values in brackets are the dose estimation and RI value at the intersection point. The dashed lines represent the 95% CI while the error bars represent the SEM.

Dose estimations using these parameters were generated for each blinded dose at each data collection time (5-40 min at 5 min increments). Figure 5-7 shows a graphical representation of the delivered dose versus the estimated dose determined using the ISX-CBMN method for each of the four culture conditions using data acquired from the longest ISX collection time (40 mins) for all 20 blinded samples. The dashed line represents the line where the delivered dose and the estimated dose would be equal and the dotted lines are the  $\pm 0.5$  Gy lines. The dose estimate for each sample was determined by examining the two dose estimates generated from the rate of MN per BNC (Figure 5-4) in conjunction with the dose estimates from both the percentage of MNCs (Figure 5-5) and RI (Figure 5-6). If the dose estimates from the percentage of MNCs and RI were below 5 Gy, then the dose estimate from the lower portion of the rate of MN per BNC calibration curve was used as the best estimation of the delivered dose. However, if the dose estimates from the percentage of MNCs and RI were above 5 Gy, then the dose estimate from the upper portion of the rate of MN per BNC calibration curve was used as the best estimation of the

delivered dose. The error bars represent the lower and upper uncertainties on the dose estimation as determined by the 95% CI. At some lower and higher doses no lower or higher error bars are shown that is due to the dose estimation not intersecting the 95% CI. Examination of Figure 5-7 indicated that beyond 4 Gy, the ISX-CBMN method was unable to predict most delivered doses to within 0.5 Gy. Even using standard CBMN culture conditions (72 h, 2 mL), none of the blinded samples above 4 Gy were estimated correctly to within 0.5 Gy. However, below 4 Gy, all but two of the nine delivered doses were estimated correctly to within 0.5 Gy. Based on these results, it is apparent that the ISX-CBMN method in its current form is unable to correctly estimate doses with an acceptable level of accuracy ( $\pm 0.5$  Gy) for doses beyond 4 Gy. However, it does appear that the method can predict doses below 4 Gy with acceptable accuracy so, it was decided to abandon the multi-parameter dose estimation method and focus solely on the rate of MN per BNC parameter as a single estimation parameter for of doses below 4 Gy.

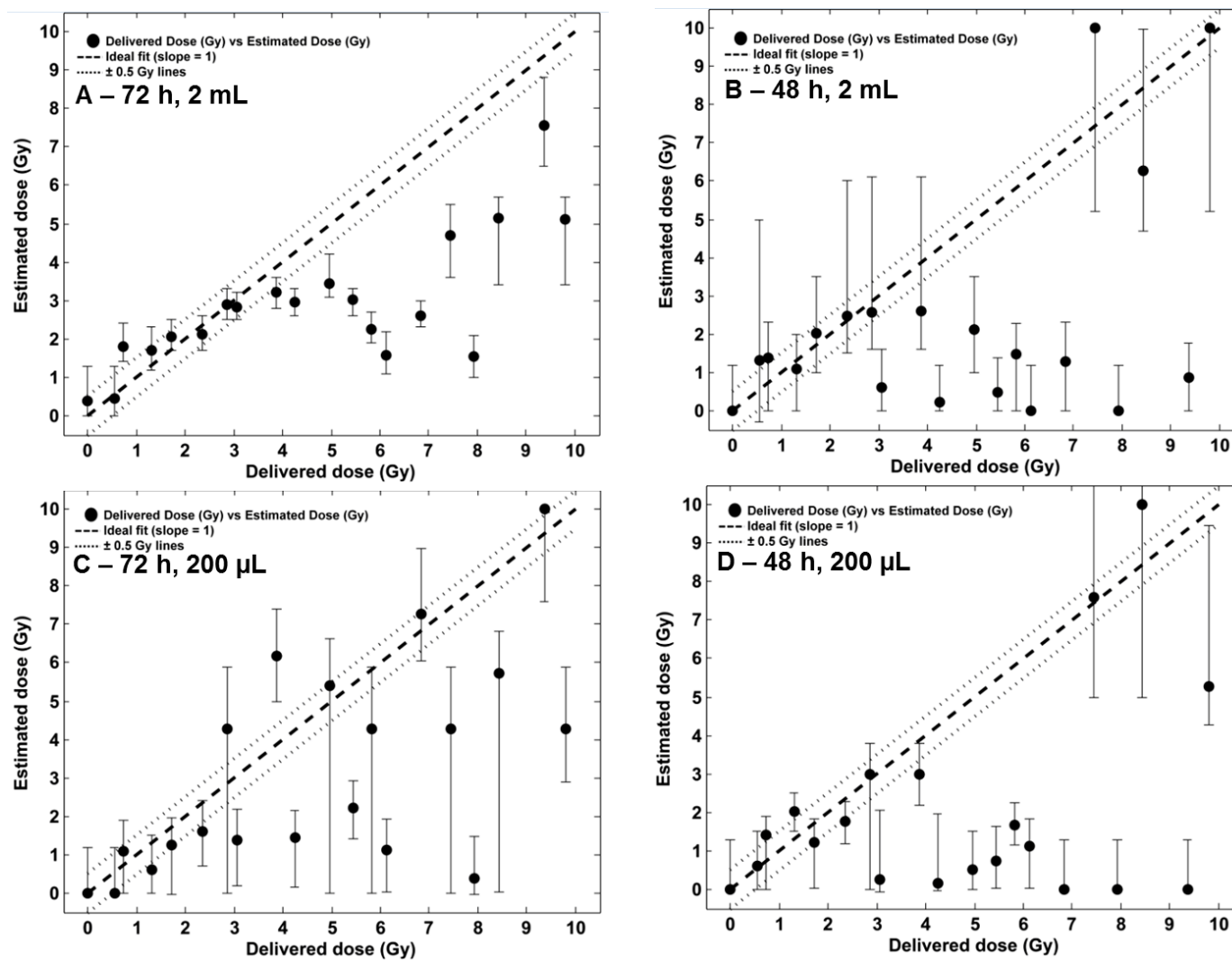


**Figure 5-7:** Estimated dose (Gy) versus delivered dose (Gy) determined by the ISX-CBMN method for all 20 blinded samples using the four culture conditions: **A.** 72 h, 2 mL; **B.** 48 h, 2 mL; **C.** 72 h, 200 μL; **D.** 48 h, 200 μL. The dashed line represents a slope of one, where the estimated dose would equal the delivered dose and the dotted lines represent  $\pm 0.5$  Gy from the ideal slope. Error bars represent the lower and upper uncertainties on the dose estimate based on the 95% CI.

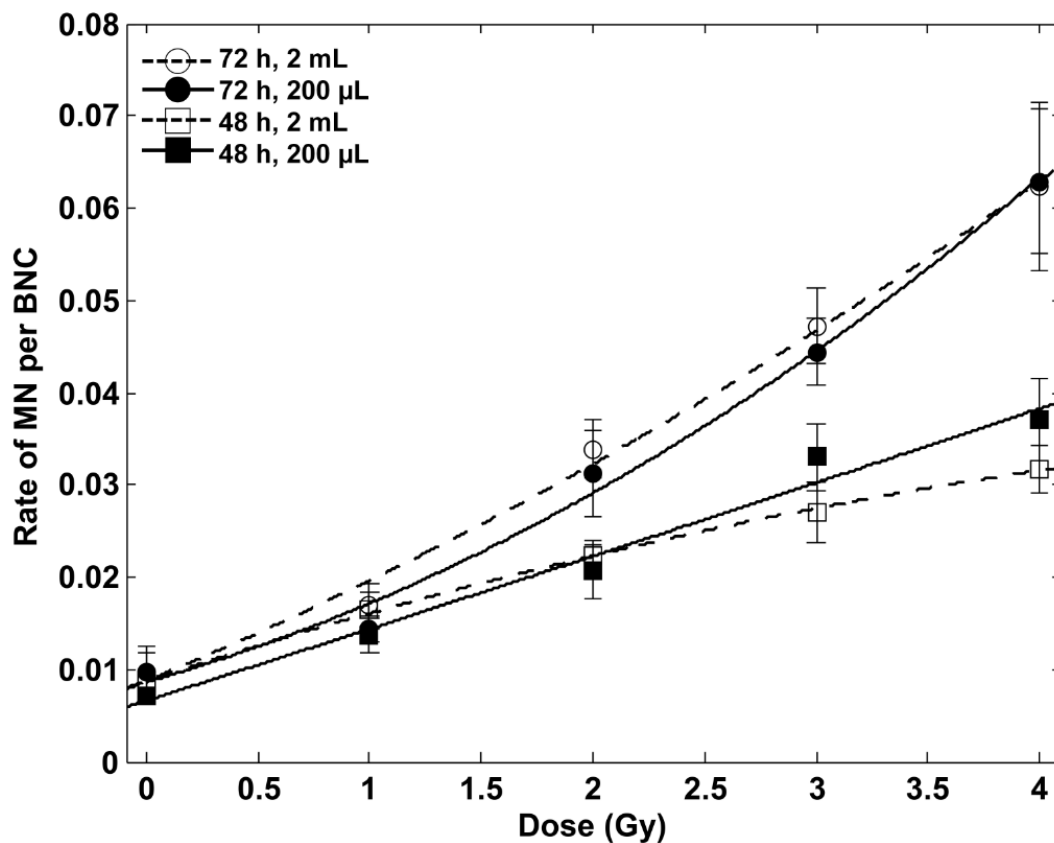
#### 5.4.2.1. Dose response calibration curves between 0-4 Gy

Figure 5-8 presents the weighted mean rate of MN per BNC from all six donors as a function of dose for each of the four culture conditions fit to a quadratic equation of the form:

$$Y = c + \alpha D + \beta D^2 \quad (5-2)$$

where  $Y$  is the number of MN per BNC,  $D$  is the dose,  $c$  is a constant and  $\alpha$  and  $\beta$  are constants corresponding to the linear and quadratic components of cell killing by radiation respectively. The error bars represent the standard error of the mean (SEM).

Table 5-2 presents the coefficients of each calibration curve, their associated standard errors and  $R^2$  values calculated with CABAS. The calibration curves for samples cultured for 72 h increase quadratically up to 4 Gy, while the calibration curves cultured for only 48 h appear to plateau around 4 Gy. Nevertheless, standard quadratic equations fit well to each data set, with  $R^2$  values of greater than 0.990 in each case. For the 2 mL and 200  $\mu$ L volumes, approximately 3000 BNCs and 1000 BNCs were collected at each dose point for each donor, respectively. The reduction in the number of scored BNCs in the smaller volume cultures resulted directly from the lower cell concentrations.



**Figure 5-8:** Calibration curves from 0 to 4 Gy for the four culture time/volume conditions (72 h, 2 mL; 48 h, 2 mL; 72 h, 200  $\mu$ L and 48 h, 200  $\mu$ L). Each data point represents the weighted mean rate of MN/BNC at each dose point for each condition and the error bars represent the standard error of the mean (SEM). Each curve was fit with a separate quadratic function.

**Table 5-2:** Coefficient values calculated for each quadratic fit for the four calibration curves

	$\beta \pm SE^*$	$\alpha \pm SE$	$c \pm SE$	$R^2$
<b>72 h, 2 mL</b>	$(2.4 \pm 0.7) \times 10^{-3}$	$(4.6 \pm 2.6) \times 10^{-3}$	$(8.7 \pm 1.5) \times 10^{-3}$	0.993
<b>48 h, 2 mL</b>	$(-0.6 \pm 0.6) \times 10^{-3}$	$(8.2 \pm 1.9) \times 10^{-3}$	$(8.2 \pm 1.1) \times 10^{-3}$	0.991
<b>72 h, 200 <math>\mu</math>L</b>	$(0.9 \pm 1.3) \times 10^{-3}$	$(10 \pm 0.43) \times 10^{-3}$	$(8.3 \pm 2.3) \times 10^{-3}$	0.994
<b>48 h, 200 <math>\mu</math>L</b>	$(0.0 \pm 1.2) \times 10^{-3}$	$(6.8 \pm 4.0) \times 10^{-3}$	$(7.8 \pm 2.3) \times 10^{-3}$	0.998

\*SE – standard error

#### **5.4.2.2. Estimation of blinded doses between 0-4 Gy**

The number of BNCs and MN were obtained from the IDEAS® software template for all nine blinded samples for each culture time and volume condition at each collection time (5 – 40 min in 5 min increments). The rate of MN per BNC was then calculated and the calibration curves presented in Figure 5-8 were used to generate dose estimates. Figure 5-9 shows a graphical representation of the delivered dose (Gy) versus the estimated dose (Gy) determined using the ISX-CBMN method for each of the four culture time and volume conditions using data acquired from the longest ISX collection time (40 min). Also plotted is the ideal line with a slope of 1 (where the delivered dose and the estimated dose would be equal) as well as the  $\pm 0.5$  Gy lines. The error bars represent the standard errors (SE) on the dose estimations obtained from CABAS. Figure 5-9A illustrates that for the standard 72 h, 2 mL culture time and volume condition, the ISX-CBMN method was able to estimate blinded doses to within 0.5 Gy of the delivered dose in all nine samples. The error bars associated with each data point are also within the 0.5 Gy lines. Figure 5-9B illustrates that for the 48 h, 2 mL condition, blinded doses were estimated correctly to within 0.5 Gy for all samples but the 3.1 Gy dose point (0.7 Gy lower than the delivered dose). Figure 5-9C and Figure 5-9D show the results of the ISX-CBMN method's ability to estimate blinded doses when only 200  $\mu$ L of whole blood is cultured for 72 h and 48 h respectively. After 72 h, dose estimations for seven of the nine samples were estimated correctly to within 0.5 Gy, with only estimations on the 2.9 Gy and 3.1 Gy doses falling outside of this range (0.7 Gy higher and 1.8 Gy lower, respectively). After 48 h of culture time, dose estimates for six of the nine samples were correct to within 0.5 Gy, with only estimations on the 1.3 Gy, 2.9 Gy and 3.1 Gy doses falling outside the 0.5 Gy lines (0.5 Gy higher, 0.8 Gy higher and 2.8 Gy lower, respectively). After careful examination of the data associated with the estimations on the 3.1 Gy sample, it was determined that the

results obtained when using an initial culture volume of 200  $\mu\text{L}$  were not representative of the accuracy of the method when compared to all other data points. As a result, this data point was identified as an outlier and was removed from all subsequent analysis.

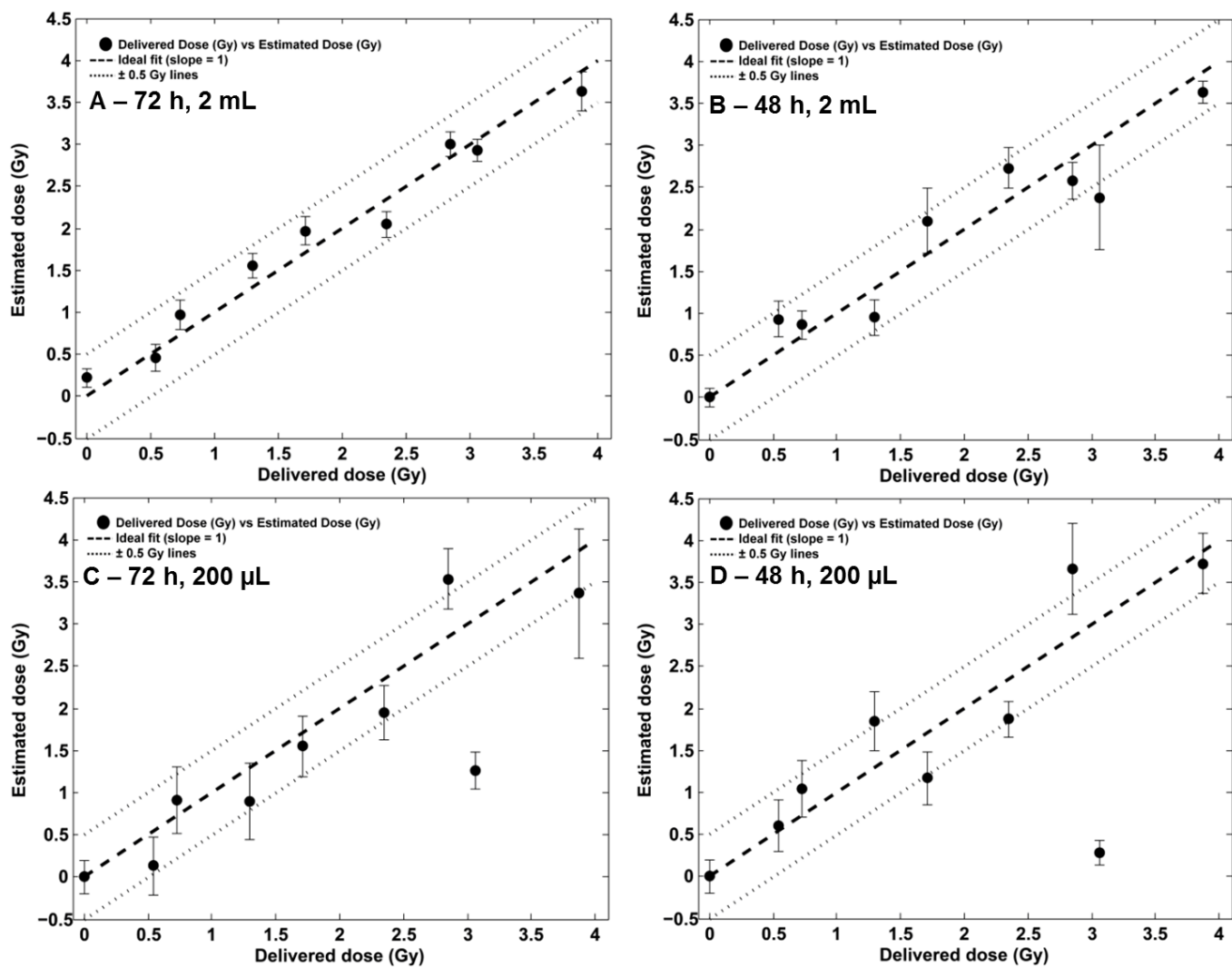


**Figure 5-9:** Estimated dose (Gy) versus delivered dose (Gy) determined by the ISX CBMN method for all nine unknown samples using the four culture time/volume conditions **A.** 72 h, 2 mL; **B.** 48 h, 2 mL; **C.** 72 h, 200  $\mu$ L **D.** 48 h, 200  $\mu$ L. The dashed line represents a slope of one, where the estimated dose would equal the delivered dose and the dotted lines represent  $\pm 0.5$  Gy from the ideal slope. The error bars represent the standard error on the estimated dose.

### 5.4.2.3. Determination of the standard error on dose estimations

While there was no difficulty in determining dose values from dose response calibration curves shown in Figure 5-8, determining the uncertainty (standard error) on the dose estimation was slightly more complex. A well-established method for determining uncertainties has been published by the International Atomic Energy Agency [97]. The solution of the quadratic equation used to estimate dose is:

$$D = \frac{-b + \sqrt{b^2 + 4a(Y - c)}}{2a} \quad (5-3)$$

where  $D$  is the dose estimation,  $Y$  is the rate of MN per BNC and  $a$ ,  $b$  and  $c$  are parameters of the quadratic fit. To determine the standard error on  $D$ , the variance on  $D$  must first be obtained. Differentiation of the equation above yields the variance on  $D$  ( $\text{var } D$ ):

$$\begin{aligned} \text{var } D = & \left(\frac{\partial D}{\partial Y}\right)^2 (\text{var}(Y)) + \left(\frac{\partial D}{\partial a}\right)^2 (\text{var}(a)) + \left(\frac{\partial D}{\partial b}\right)^2 (\text{var}(b)) + \left(\frac{\partial D}{\partial c}\right)^2 (\text{var}(c)) + \\ & 2\left(\frac{\partial D}{\partial a}\right)\left(\frac{\partial D}{\partial b}\right) \text{covar}(a, b) + 2\left(\frac{\partial D}{\partial b}\right)\left(\frac{\partial D}{\partial c}\right) \text{covar}(b, c) + 2\left(\frac{\partial D}{\partial a}\right)\left(\frac{\partial D}{\partial c}\right) \text{covar}(a, c) \end{aligned} \quad (5-4)$$

Then, the standard error is obtained by taking the square root of the variance on  $D$ . These calculations can become quite cumbersome but fortunately the CABAS software has been written to perform these calculations automatically. Data from the calibration curves as well as the rate of MN per BNC from each blinded sample was entered into CABAS that calculated the standard errors on all dose estimations that are represented by the error bars in Figure 5-9.

#### **5.4.3. Minimum collection time required to estimate doses to within 0.5 Gy**

Data for all nine blinded samples was collected for 5 – 40 min (in 5 min increments) on the ISX in an attempt to determine an approximate minimum collection time required to estimate doses to within 0.5 Gy of the delivered dose. Figure 5-10 and Figure 5-11 present the average absolute value of the difference between the estimated dose and the delivered dose for all nine blinded samples at each collection time. For the 72 h, 2 mL and 48 h, 2 mL conditions as well as the 48 h, 200  $\mu$ L condition, the data was found to fit best to a quadratic relation but for the 72 h, 200  $\mu$ L condition the data fit best to a rational function. All fits were generated using the weighted fitting algorithm in Sigmaplot. The error bars represent the SEM of the average absolute difference between the estimated and delivered doses for all nine samples. From Figure 5-10 it can be seen that for samples cultured for 72 h with an initial volume of 2 mL, blinded doses were estimated to within 0.5 Gy of the delivered dose, on average, after only 6.5 min of data collection. However, when the initial blood culture volume was reduced to 200  $\mu$ L, 11 min of data collection was required. For samples cultured for 48 h with an initial volume of 2 mL, Figure 5-11 shows that an average collection time of 19 min was required to estimate blinded doses to within 0.5 Gy. When the initial blood volume was reduced to 200  $\mu$ L, 27 min of data collection time was required, on average, to achieve the same accuracy. On average, for the 72 h, 2 mL culture condition, 6.5 min of data collection resulted in approximately 1000 BNCs being scored while 11 min of data collection for the 72 h, 200  $\mu$ L culture condition generated approximately 400 scored BNCs. For the 48 h, 2 mL culture condition, 19 min of data collection resulted in approximately 2000 BNCs scored and for the 48 h, 200  $\mu$ L culture condition, 27 min of data collection generated approximately 600 scored BNCs, on average.

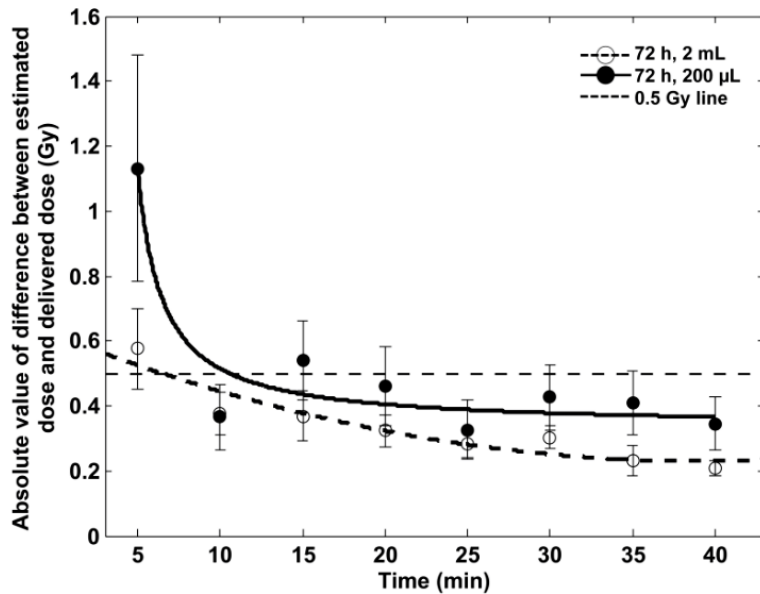


**Figure 5-10:** Average absolute value of the difference between the estimated dose and the delivered dose (Gy) versus collection time for all unknown samples cultured for 72 h with initial blood volumes of 2 mL and 200 µL. The 2 mL data was fit with a quadratic function (dashed line) while the 200 µL data was fit to a rational function (solid line). The error bars represent the SEM of the average difference between the estimated and delivered doses. The dashed line highlights the 0.5 Gy difference between the estimated and delivered doses.

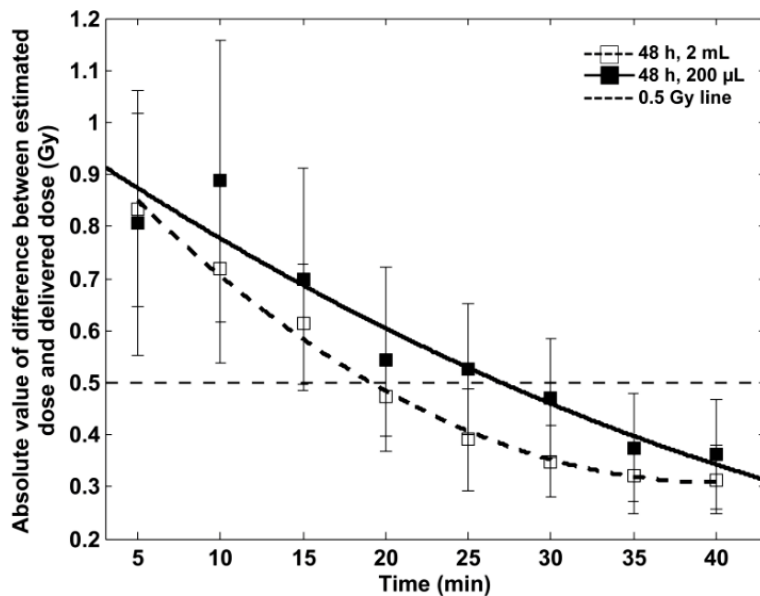


**Figure 5-11:** Average absolute value of the difference between the estimated dose and the delivered dose (Gy) versus collection time for all unknown samples cultured for 48 h with initial blood volumes of 2 mL and 200 µL. Data sets were fit with separate quadratic functions. The error bars represent the SEM of the average difference between the estimated and delivered doses. The dashed line highlights the 0.5 Gy difference between the estimated and delivered doses.

## 5.5. Discussion

Chapters 3 and 4 have introduced the feasibility of adapting the traditional microscope-based CBMN assay to a new imaging FCM method using the ISX, demonstrating its potential as a rapid, high throughput triage biodosimetry tool [79, 83]. The aim of the present study was to validate the accuracy of this method to quantify blinded doses between 0-4 Gy using standard and reduced culture time and volume conditions.

Figure 5-4, Figure 5-5 and Figure 5-6 present plots used to estimate delivered doses using the rate of MN per BNC, percentage of MNCs and RI parameters, respectively. The use of the percentage of MNCs as well as the RI were intended to compliment the rate of MN per BNC when determining doses above 5 Gy, thus obtaining multi-parameter dose estimations. Figure 5-7 shows the results of dose estimations performed by the ISX-CBMN method for twenty samples irradiated to known doses and blinded for each of the four culture conditions. It can be seen that below 4 Gy, the estimated dose was within the  $\pm 0.5$  Gy lines for the majority of points at each condition.. However beyond 5 Gy, the dose predictions were drastically underestimated in nearly every sample at each culture condition that is likely the result of multiple factors. At such high doses, delays in the S and G<sub>2</sub> phases of the cell cycle cause a decrease in proliferation that results in a fewer cells entering mitosis and passing through karyokinesis, leading to a reduction in the number of MN expressed [50]. Additionally, the percentage of MNC and RI values caused the wrong portion of the rate of MN per BNC calibration curve in Figure 5-4 being chosen that may be due to the fact that the range of both the percentage of MNCs and the RI at standard culture time and volume conditions was somewhat narrow (79.1% at 0 Gy to 92.4% at 10 Gy for the percentage of MNCs and 1.21 at 0 Gy to 1.07 at 10 Gy for the RI). Furthermore, the range in both of these parameters was further narrowed when the culture

times and volumes were reduced and therefore, reliably distinguishing between low and high doses became more difficult. While these results are somewhat disappointing, it has been stated previously that following a whole body dose of greater than 4 Gy, the physical symptoms would be treated by clinicians long before biodosimetric dose estimates are provided. Furthermore, in the 0-4 Gy dose range where biodosimetry is most applicable, the ISX-CBMN method is able to generate dose estimations that are within about 0.5 Gy of the delivered dose (Figure 5-7). Therefore, given these results, it was decided to focus on the accuracy of the ISX-CBMN method in the 0-4 Gy dose range with reduced culture time and volume conditions.

Dose response calibration curves were generated at 72 and 48 h for both large and small volume cultures. For the 72 h, 2 mL condition there was a clear quadratic dependence from 0-4 Gy that was expected as this culture time and volume represents standard CBMN conditions. This quadratic dependence has been demonstrated previously in various works on the CBMN assay [32, 35, 79, 83, 98]. Approximately 3000 BNCs were scored on average from each donor at each dose point in the IDEAS® analysis template. This is a significantly higher number than was reported in the first publication on this work [79], that resulted from the creation of a more optimal IDEAS® analysis template [83]. When a smaller blood volume was used, a quadratic relation was still observed after 72 h of culture time and approximately 1000 BNCs from each donor at each dose point were scored on average. For both blood volumes cultured for 48 h, the rate of increase of MN per BNC begins to plateau towards 4 Gy. This result is not unexpected as a similar trend was noted at 5 Gy using standard culture time and volume conditions in recent work using the ISX-CBMN method [83] and in other automated CBMN techniques [66]. After only 48 h of culture time, fewer cells would be expected to have passed through mitosis at higher doses as compared to 72 h of culture time with damaged cells cycling even more

slowly than healthy cells. Therefore, a decrease in both BNCs and subsequently the number of MN expressed is expected. Nevertheless, for the 48 h, 2 mL condition approximately 2000 BNCs were scored from each donor at each dose point and for the 48 h, 200  $\mu$ L condition an average of 1000 BNCs were scored, illustrating that after a culture time of only 48 h the ISX-CBMN method is able to score at least an equivalent number of BNCs as conventional microscope-based CBMN.

In order to evaluate the ability of the ISX-CBMN method to estimate dose, nine samples were irradiated, blinded and cultured according to the four time and volume conditions. Data was acquired from each sample for 40 min and processed in IDEAS® to obtain the number of MN and BNCs that was converted to a dose based on the appropriate calibration curve. With standard culture time and volume conditions (72 h, 2 mL), the ISX-CBMN method was able to correctly estimate doses to within 0.3 Gy for all nine blinded samples. Willems et al. [37] were able to generate dose estimates to within 0.2 Gy of the delivered dose using automated slide-scoring however, only a single dose point (1 Gy) was examined. Additionally, in recent publications by De Amicis et al. [62] and De Sanctis [63] dose estimates were generated to within 0.3 Gy (or less) of the delivered dose using automated slide-scoring for a number of doses between 0-4 Gy. The results of the work presented here demonstrates that the ISX-CBMN method, performed using standard culture time and volume conditions, is also able to estimate blinded doses between 0-4 Gy to within 0.3 Gy of the delivered dose and is comparable to results presented in other works using automated slide-scoring versions of the CBMN assay.

To address the ability of the ISX-CBMN method to estimate blinded doses when reduced culture time and volume conditions were implemented as suggested by Fenech [92], doses were estimated based on calibration curves and blinded samples generated with three additional culture conditions. Results showed that doses were correctly

estimated to within 0.5 Gy of the delivered dose in eight, seven and six of the nine blinded samples with culture time and volume conditions of 48 h, 2 mL; 72 h, 200  $\mu$ L and 48 h, 200  $\mu$ L respectively. Deviations larger than 0.5 Gy at higher doses are not unexpected as error bars in the calibration curves tended to increase with decreasing culture time and/or volume. With increasing doses, the standard error of the mean in the calibration curves increased, indicating larger variability in the rate of MN per BNC as doses approached 3 Gy. In addition, the error bars on the blinded samples themselves also increased at higher doses as culture time and volume decreased. This can be attributed to the reduction in the overall number of BNCs when culturing only 200  $\mu$ L of blood for 48 h that translated to a larger uncertainty in the rate of MN per BNC. After careful examination of the data associated with the 3.1 Gy sample, no inconsistencies in any portion of the IDEAS® analysis template (cell population locations with respect to gate positions, cell image quality, masking, etc.) were discovered. This result is unexpected and no definitive explanation for the deviation between delivered and estimated doses is available.

In triage radiation biodosimetry, generating an estimation of the dose received by an individual that is both accurate and obtained in a timely manner is necessary. As such, it was desirable to determine, on average, the minimum ISX data collection time required to generate dose estimations to within 0.5 Gy of the delivered dose for each of the four culture conditions. The results demonstrate that after 72 h of culture, dose estimates within 0.5 Gy can be generated with only 6.5 min and 11 min of data collection for the 2 mL and 200  $\mu$ L blood volumes respectively. In these times, approximately 1000 and 600 BNCs were scored on average, respectively. Similarly, for samples cultured for 48 h, doses can be estimated to within 0.5 Gy after 19 min and 27 min of data collection for the 2 mL and 200  $\mu$ L blood volumes respectively. Approximately 2000 and 400 BNCs were scored in these times on average, respectively. The larger number of BNCs scored with 2 mL initial

blood volumes was expected even with shorter collection times, due to the high cell concentrations. Despite longer data collection times for the 200  $\mu$ L blood volumes, a reduction in the number of BNCs scored was observed. This is not surprising as the cell concentrations were one order of magnitude lower than the 2 mL blood volumes but this does not impact the ability of the method to generate accurate dose estimations. The longer collection time required to estimate blinded doses to within 0.5 Gy after only 48 h of culture was also expected as the rate of MN expressed is reduced as illustrated in the calibration curves. The 6.5 min of data collection at standard conditions combined with an additional 5 min to process the data file in IDEAS® allows dose estimations to be generated in about 10 min from the time the sample is introduced into the ISX. This is markedly faster than any automated procedure that has been presented in the literature to perform the CBMN assay using slide-based microscopy. The automated slide-scoring procedure described by Willems et al. [37] generates dose estimations with slightly better accuracy than the ISX-CBMN method but with nearly double the time required to score 1000 BNCs (22 min). De Amicis et al. [62] also used an automated slide-scoring method to score CBMN slides and were able to generate dose estimations with the same level of accuracy as the ISX-CBMN method in approximately the same time (8 min). The Rapid Automated Biodosimetry Tool (RABiT) developed at Columbia University claims to be able to process 6,000 samples per day and while dose response calibration curves have been generated using the system, the number of BNCs scored at each dose point was an order of magnitude lower than the number of BNCs scored to generate similar curves using the ISX-CBMN method. In addition, the time to identify and score the MN and BNCs to generate one data point in each calibration curve was estimated at 22 min [66]. Therefore, using the standard CBMN culture time and volume conditions described in this work (72

h, 2 mL), the ISX-CBMN method is as rapid and accurate as any other currently available methods that use the CBMN assay to estimate blinded radiation doses between 0-4 Gy.

The true power of the ISX-CBMN method has been realized by reducing the overall culture time to 48 h while still maintaining an acceptable level of accuracy when attempting to estimate blinded doses. Doses were correctly estimated to within 0.5 Gy for eight of nine blinded samples and this accuracy can be obtained with an average data collection time of just 19 min. Furthermore, the same level of accuracy can be obtained when only 200  $\mu$ L of whole blood is cultured for 48 h with 27 min of data collection on the ISX required. To the best of our knowledge, at present, no methods of performing the CBMN assay for the purposes of radiation biodosimetry exist in the literature in which dose estimations can be generated after only 48 h of culture time to the level of accuracy obtained with the ISX-CBMN method. By reducing the required culture time to only 48 h, the ISX-CBMN method is now comparable with the dicentric chromosome assay (DCA) that is considered the gold standard in radiation biodosimetry [1, 6, 99]. Furthermore, the time required to estimate an unknown dose using the most rapid DCA technique (Quickscan) is approximately 20 min [26, 100]. This is roughly the same amount of time that a dose estimation can be acquired using the ISX-CBMN method using the 48 h, 2 mL culture time and volume condition (19 min).

## **5.6. Conclusion**

The results presented in this chapter demonstrate that the CBMN assay can be performed on the ISX to generate dose estimations to within 0.3 Gy of the delivered dose after only 6.5 min of data collection using standard culture time and volume conditions. By reducing the required culture time to 48 h, the method can be performed in a timeframe that is comparable to the DCA (19 min). Furthermore, with only 200  $\mu$ L of whole blood

cultured for 48 h, the blinded doses were estimated to within 0.5 Gy after collecting data for only 27 min. Being able to provide accurate and reliable dose estimations for a large number of exposed individuals after only 48 h would allow appropriate and possibly life-saving treatment to begin very quickly that dramatically increases the relevance and applicability of the CBMN assay as a radiation biodosimetry tool following a mass casualty event.

## **6. GENERAL CONCLUSIONS**

The CBMN assay developed nearly 30 years ago is a well-established technique in radiation biodosimetry for estimating blinded doses by correlating the rate of MN in BNCs to dose using peripheral blood lymphocytes. In recent years, a number of attempts have been made to increase the throughput of the assay for the purposes of triage biodosimetry by automating the slide-scoring process. The research presented in this thesis has focused on the development of an entirely new and novel method of performing the CBMN assay on the ISX imaging flow cytometer.

### **6.1. Summary of thesis findings**

Chapter 3 of this thesis described a new and novel protocol developed to adapt the traditional CBMN assay into an imaging FCM method on the ISX. This new ISX-CBMN method allows for visualization of the cytoplasm, main nuclei and MN in every scored cell. Although the frequency of MN scored is lower than traditional versions of the assay, this has been noted in other automated methods and is likely a consequence of the stricter scoring parameters applied in image analysis or the inability to observe MN which may be hidden behind the main nuclei in a BNC [39, 61-63]. While the same IDEAS® software template used to generate the dose response calibration curves would be employed to provide dose estimations in radiation biodosimetry, the lower frequency of MN would impact sensitivity and accuracy. The results presented indicate that the ISX-CBMN method is able to automatically image, identify and score nearly twice the number of BNCs that are typically scored in all manual and automated microscope-based versions of the assay.

It has been posited in the literature that it may be possible to use the CBMN assay to estimate doses beyond 5 Gy through the use of a multi-parameter approach. Chapter 4

introduced a more robust, multi-parameter version of the ISX-CBMN method by extending the dose range for the rate of MN per BNC parameter to 10 Gy, as well as including the percentage of MNCs and the RI as additional scoring parameters. The rate of MN per BNC was shown to decline beyond 5 Gy, a result that is consistent with findings in other literature and is likely due to the reduction in cell proliferation following high doses. Furthermore, a consistent increase in the percentage of MNCs as well as a steady decline in the RI was illustrated from 0-10 Gy, results that were expected based on other works in the literature. Additionally, the data analysis template developed in IDEAS® was optimized to better identify MN and BNCs and reduce false positive events. The effect of donor variability in both sample processing and analysis on the ISX was also investigated and shown to be negligible when compared to the variability that is observed between donors.

Two drawbacks of the CBMN assay in its traditional form are the large initial blood culture volume and the relatively long culture time requirement. Chapter 5 investigated whether the ISX-CBMN method could be performed with an initial blood volume of 200  $\mu$ L cultured for only 48 h. Blinded doses between 0-4 Gy were estimated to within 0.5 Gy of the delivered dose using standard culture time/volume conditions (72 h, 2 mL) 100% of the time after only 5 min of data collection (on average) on the ISX. Furthermore, following culture of 200  $\mu$ L of whole blood for just 48 h, the ISX-CBMN method was able to predict blinded doses to within 0.5 Gy nearly 70% of the time after 30 min of data collection. The results presented in this chapter indicate that ISX-CBMN method is able to provide accurate dose estimations after only 48 h of culture time that dramatically increases the relevance and applicability of the CBMN assay as a radiation biodosimetry tool.

## **6.2. Further work and suggested improvements with the ISX-CBMN method**

The ISX-CBMN method in its current form is able to estimate blinded doses with an accuracy of 0.5 Gy for doses between 0-4 Gy after only 48 h of culture time. While the assay performs well in its current form, a number of possible improvements should be investigated.

The data files generated by the ISX are quite large (about 1 GB) that results from unwanted events (such as large debris) being acquired due to the limited classification filters applied during data collection. Furthermore, in a data file of about 30,000 events, roughly 10% are scored BNCs while the remainder are filtered out in the gating process. Optimization of the data collection parameters on the ISX could be investigated to reduce the number of undesirable events collected, which would in turn reduce the size of the data files. This may also increase the MN frequency in the final gated populations as the number of true BNCs that are possibly gated out may be reduced.

Some studies have suggested that the frequency of micronucleated mononuclear cells as well as the frequency of trinucleated (three nuclei in one cytoplasm) and tetranucleated (four or more nuclei in one cytoplasm) cells may be used as complementary parameters to the rate of MN per BNC, that may increase the dose range of the CBMN assay [51, 87, 92]. In addition, the CBMN cytome assay described by Fenech [47] also incorporates the scoring of nucleoplasmic bridges (a biomarker of DNA misrepair), nuclear buds (a biomarker of elimination of amplified DNA and/or DNA repair complexes) and cell death (necrosis or apoptosis). The IDEAS® analysis template could be modified from its current form to score these additional endpoints to create an even more robust multi-parameter method. Inclusion of these scoring parameters may improve dose estimation

capabilities beyond 5 Gy that were less than desirable when only the percentage of MNCs and RI were used as complimentary parameters to the rate of MN per BNC.

Currently, individual samples are manually placed to the ISX but the capability to process a high number of samples consecutively through the addition of a 96 well plate autosampler is possible. Additionally, upgraded acquisition templates are available for the INSPIRE software which controls the ISX that would allow multiple experiments to be conducted per plate. The addition of an autosampler would dramatically increase the rate at which data could be collected by the ISX, as well as the number of samples that could be processed. The ISX could then be run unattended during the day or even overnight, which would significantly increase throughput for the purposes of radiation biodosimetry.

Validation of the ISX-CBMN method should be performed at a different laboratory possessing similar equipment. Whole blood should be irradiated by x-rays as described in section 3.3.3, the sample processing protocol described in Appendix I should be followed exactly and the IDEAS® data analysis template described in section 4.4.1 should be used to develop calibration curves from 0-4 Gy. It has been demonstrated that both the protocol and data analysis methods are highly reproducible between samples and donors within the same laboratory. Validation performed in this way would allow for a complete independent verification of the entire method and would determine if the protocol and results are reproducible between laboratories.

Some clinical radiotherapy treatments may involve total body irradiation of a patient, typically as part of a preparative regimen for haematopoietic stem cell transplants. Depending on the procedure, some doses can be as high as 10 Gy, often given in 2 Gy fractions [101]. Being able to perform the CBMN assay on the ISX after only 48 h of culture time may make this form of the assay applicable as a biodosimeter to compare the biological and physical doses following fractionated total body irradiation.

Finally, the MN assay is used extensively in toxicological screening for potential genotoxic compounds and assesses clastogenic (chromosome breakage) and aneugenic (causes daughter cells with abnormal numbers of chromosomes) events as well as some epigenetic effects [102]. The *in vitro* MN test is an attractive tool due to its simplicity of scoring, accuracy and wide applicability in many cell types. Protocols designed to assess human primary lymphocytes and cell lines have been established and validated [103, 104]. It may be possible to adapt these protocols for use on the ISX which may increase the throughput of these protocols. Furthermore, the IDEAS® software may allow for simultaneous automatic scoring of MN, nucleoplasmic bridges, nuclear buds and apoptotic or necrotic cells by incorporating a multi-colour approach which would improve the robustness of the test.

### **6.3. Concluding remarks**

Following a radiation accident or event involving large numbers of casualties, it is imperative to assess the dose received by exposed individuals as quickly as possible. The potential for occurrence of these types of events is ever increasing and as such, rapid and accurate dose assessments obtained from biological dosimetry techniques are necessary to provide clinicians with guidance to perform appropriate triage. Medical intervention for the ARS as early as possible has been shown to improve the survival of exposed individuals so it is important to distinguish between those who require treatment in hospital (doses greater than 1.5-2 Gy) from those who do not (doses less than 1.5 Gy). The results presented in this thesis describe the first known automated method for performing the CBMN assay after a total culture time of only 48 h to achieve dose estimations within 0.5 Gy of the delivered dose. By adapting the traditional CBMN assay for use on the ISX imaging flow cytometer, throughput has been significantly increased while maintaining

accuracy in dose estimations that are similar to other works using automated versions of the traditional form of the assay. Further work should be performed to investigate the practicality of the ISX-CBMN method at doses beyond 4 Gy and independent verifications in other laboratories should be performed to validate the method.

## REFERENCES

- [1] Lloyd, D.C., et al., *The role of cytogenetics in early triage of radiation casualties*. Applied Radiation and Isotopes, 2000. 52(5): p. 1107-1112.
- [2] Lindholm, C., et al., *Premature Chromosome Condensation (PCC) assay for dose assessment in mass casualty accidents*. Radiation Research, 2010. 173(1): p. 71-78.
- [3] Pinto, M.M., N.F. Santos, and A. Amaral, *Current status of biodosimetry based on standard cytogenetic methods*. Radiat Environ Biophys, 2010. 49(4): p. 567-81.
- [4] Riecke, A., C.G. Ruf, and V. Meineke, *Assessment of radiation damage-the need for a multiparametric and integrative approach with the help of both clinical and biological dosimetry*. Health Physics, 2010. 98(2): p. 160-167.
- [5] IAEA, *Cytogenetic Dosimetry: Applications in Preparedness for and Response to Radiation Emergencies*. 2011. Vienna, EPR-Biodose.
- [6] Sullivan, J.M., et al., *Assessment of biodosimetry methods for a mass-casualty radiological incident: medical response and management considerations*. Health physics, 2013. 105(6): p. 540-54.
- [7] Tofani, A., *Assessing the Radiological Impact of Radiation Exposure Devices*. Risk Analysis, 2011. 31(4): p. 566-577.
- [8] Margeanu, C.A., *Comparative Study on Radiological Impact due to Direct Exposure to a Radiological Dispersal Device using a Sealed Radiation Source in Tenth Radiation Physics & Protection Conference*. 2010: Cairo, Egypt. p. 27-30.
- [9] UNSCEAR, *Sources and effects of ionizing radiation, Annex D: Health effects due to radiation from the Chernobyl accident*. 2008. Vienna.
- [10] Nuclear and Industrial Safety Agency, *Seismic Damage Information (110th Release)*. 2011.
- [11] Chino, M., et al., *Preliminary estimation of release amounts of  $^{131}\text{I}$  and  $^{137}\text{Cs}$  accidentally discharged from the Fukushima Daiichi Nuclear power plant into the atmosphere*. Journal of Nuclear Science and Technology, 2011. 48(7): p. 1129-1134.
- [12] IAEA, *The Radiological Accident in Goiania*. 1988. Vienna.
- [13] IAEA, *The Radiological Accident in Samu Prakarn*. 2002. Vienna.
- [14] Bolognesi, C., et al., *Micronucleus test for radiation biodosimetry in mass casualty events: Evaluation of visual and automated scoring*. Radiation Measurements, 2011. 46(2): p. 169-175.

- [15] Chen, Y.C., et al., *Validating High-Throughput Micronucleus Analysis of Peripheral Blood Reticulocytes For Radiation Biodosimetry: Benchmark Against Dicentric and CBMN Assays In a Mouse Model*. Health Physics, 2010. 98(2): p. 218-227.
- [16] Hall, E.J. and A.J. Giaccia, *Radiobiology for the Radiologist*. 7th ed. 2012: Lippincott Williams & Wilkins.
- [17] Donnelly, E.H., et al., *Acute radiation syndrome: Assessment and management*. Southern Medical Journal, 2010. 103(6): p. 541-546.
- [18] IAEA, *Effects of Ionizing Radiation on Blood and Blood Components: A Survey*. 1997. Vienna.
- [19] Singh, V.K., V.L. Newman, and T.M. Seed, *Colony-stimulating factors for the treatment of the hematopoietic component of the acute radiation syndrome (H-ARS): A review*. Cytokine, 2015. 71(1): p. 22-37.
- [20] Yen, T.H. and N.A. Wright, *The gastrointestinal tract stem cell niche*. Stem Cell Reviews, 2006. 2(3): p. 203-212.
- [21] Campbell, N.A., et al., *Biology*. 8th ed. 2009: Pearson Benjamin Cummings.
- [22] Goodhead, D.T., *Initial events in the cellular effects of ionizing radiations: Clustered damage in DNA*. International Journal of Radiation Biology, 1994. 65(1): p. 7-17.
- [23] Prasanna, P.G.S., M. Moroni, and T.C. Pellmar, *Triage dose assessment for partial-body exposure: dicentric analysis*. Health Physics, 2010. 98(2): p. 244-251.
- [24] Romm, H., U. Oestreicher, and U. Kulka, *Cytogenetic damage analysed by the dicentric assay*. Annali dell'Istituto Superiore di Sanita, 2009. 45(3): p. 251-259.
- [25] Flegal, F.N., et al., *Quickscan dicentric chromosome analysis for radiation dosimetry*. Health Physics, 2010. 98(2): p. 276-281.
- [26] Flegal, F.N., et al., *Validation of Quickscan dicentric chromosome analysis for high throughput radiation biological dosimetry*. Health Physics, 2012. 102(2): p. 143-153.
- [27] Vaurijoux, A., et al., *Detection of Partial-Body Exposure to Ionizing Radiation by the Automatic Detection of Dicentrics*. Radiation Research, 2012. 178(4): p. 357-364.
- [28] Vaurijoux, A., et al., *Strategy for Population Triage Based on Dicentric Analysis*. Radiation Research, 2009. 171(5): p. 541-548.
- [29] Fantes, J.A., et al., *Detecting radiation damage to human chromosomes by flow cytometry*. Mutation Research, 1983. 119(2): p. 161-168.
- [30] Fantes, J.A., et al., *Flow cytometry measurements of human chromosome kinetochore labeling*. Cytometry, 1989. 10(2): p. 134-142.

- [31] Beaton, L.A., et al., *Analysis of chromosome damage for biodosimetry using imaging flow cytometry*. *Mutat. Res.: Genet. Toxicol. Environ. Mutagen.*, 2013.
- [32] Fenech, M. and A.A. Morley, *Measurement of Micronuclei in Lymphocytes*. *Mutation Research*, 1985. 147(1-2): p. 29-36.
- [33] Fenech, M. and A.A. Morley, *Cytokinesis-block micronucleus method in human lymphocytes - effect of in vivo aging and low dose x-irradiation*. *Mutation Research*, 1986. 161(2): p. 193-198.
- [34] Fenech, M., *The cytokinesis block micronucleus technique - A detailed description of the method and its application to genotoxicity studies in human populations*. *Mutation Research*, 1993. 285(1): p. 35-44.
- [35] McNamee, J.P., et al., *Validation of the cytokinesis-block micronucleus (CBMN) assay for use as a triage biological dosimetry tool*. *Radiation Protection Dosimetry*, 2009. 135(4): p. 232-242.
- [36] Vral, A., M. Fenech, and H. Thierens, *The micronucleus assay as a biological dosimeter of in vivo ionising radiation exposure*. *Mutagenesis*, 2011. 26(1): p. 11-17.
- [37] Willems, P., et al., *Automated micronucleus (MN) scoring for population triage in case of large scale radiation events*. *International Journal of Radiation Biology*, 2010. 86(1): p. 2-11.
- [38] Tucker, J.D., et al., *Estimating the lowest detectable dose of ionizing radiation by the cytokinesis-block micronucleus assay*. *Radiation Research*, 2013. 180(3): p. 284-291.
- [39] Varga, D., et al., *An automated scoring procedure for the micronucleus test by image analysis*. *Mutagenesis*, 2004. 19(5): p. 391-397.
- [40] Rahman, M., *Introduction to Flow Cytometry*. 2006, Kidlington, Oxford, UK: Serotec Ltd. Endeavour House.
- [41] Brown, M. and C. Wittwer, *Flow cytometry: Principles and clinical applications in hematology*. *Clinical Chemistry*, 2000. 46(8 II): p. 1221-1229.
- [42] Zuba-Surma, E.K., et al., *The ImageStream system: A key step to a new era in imaging*. *Folia Histochemica et Cytobiologica*, 2007. 45(4): p. 279-290.
- [43] Schmid, W., *The micronucleus test*. *Mutation Research*, 1975. 31(1): p. 9-15.
- [44] Countryman, P.I. and J.A. Heddle, *The production of micronuclei from chromosome aberrations in irradiated cultures of human lymphocytes*. *Mutation Research*, 1976. 41(2-3): p. 321-332.

- [45] Theodoropoulos, P.A., et al., *Cytochalasin B may shorten actin filaments by a mechanism independent of barbed end capping*. *Biochemical Pharmacology*, 1994. 47(10): p. 1875-1881.
- [46] Moore, G.E. and L.K. Woods, *Culture Media for Human Cells - RPMI 1603, RPMI 1634, RPMI 1640 and GEM 1717*. 1976.
- [47] Fenech, M., *Cytokinesis-block micronucleus cytome assay*. *Nature Protocols*, 2007. 2(5): p. 1084-1104.
- [48] Lim, H.K., P.V. Asharani, and M.P. Hande, *Enhanced genotoxicity of silver nanoparticles in DNA repair deficient mammalian cells*. *Frontiers in Genetics*, 2012. 3(JUN).
- [49] Fenech, M., et al., *HUMN project: Detailed description of the scoring criteria for the cytokinesis-block micronucleus assay using isolated human lymphocyte cultures*. *Mutation Research - Genetic Toxicology and Environmental Mutagenesis*, 2003. 534(1-2): p. 65-75.
- [50] Maity, A., W.G. McKenna, and R.J. Muschel, *The molecular basis for cell cycle delays following ionizing radiation: a review*. *Radiotherapy and Oncology*, 1994. 31(1): p. 1-13.
- [51] Müller, W.U. and A. Rode, *The micronucleus assay in human lymphocytes after high radiation doses (5-15 Gy)*. *Mutation Research-Fundamental and Molecular Mechanisms of Mutagenesis*, 2002. 502(1-2): p. 47-51.
- [52] Thierens, H., et al., *Cytogenetic monitoring of hospital workers occupationally exposed to ionizing radiation using the micronucleus centromere assay*. *Mutagenesis*, 2000. 15(3): p. 245-249.
- [53] Bigatti, P., et al., *Cytogenetic monitoring of hospital workers exposed to low-level ionizing radiation*. *Mutation Research*, 1988. 204(2): p. 343-347.
- [54] Jha, A.N. and T. Sharma, *Enhanced frequency of chromosome aberrations in workers occupationally exposed to diagnostic x-rays*. *Mutation Research - Genetic Toxicology Testing and Biomonitoring of Environmental or Occupational Exposure*, 1991. 260(4): p. 343-348.
- [55] Barquinero, J.F., et al., *Cytogenetic analysis of lymphocytes from hospital workers occupationally exposed to low levels of ionizing radiation*. *Mutation Research - Fundamental and Molecular Mechanisms of Mutagenesis*, 1993. 286(2): p. 275-279.
- [56] Liu, Q., et al., *Dose estimation by chromosome aberration analysis and micronucleus assays in victims accidentally exposed to <sup>60</sup>Co radiation*. *British Journal of Radiology*, 2009. 82(984): p. 1027-1032.
- [57] Thierens, H., et al., *Cytogenetic biodosimetry of an accidental exposure of a radiological worker using multiple assays*. *Radiation Protection Dosimetry*, 2005. 113(4): p. 408-414.

- [58] Voisin, P., et al., *The cytogenetic dosimetry of recent accidental overexposure*. Cellular and Molecular Biology, 2001. 47(3): p. 557-564.
- [59] Castelain, P., et al., *Automated Detection of Cytochalasin-B Blocked Binucleated Lymphocytes for Scoring Micronuclei*. Mutagenesis, 1993. 8(4): p. 285-293.
- [60] Verhaegen, F., et al., *Scoring of Radiation-Induced Micronuclei in Cytokinesis-Blocked Human-Lymphocytes by Automated Image-Analysis*. Cytometry, 1994. 17(2): p. 119-127.
- [61] Schunck, C., et al., *New developments in automated cytogenetic imaging: unattended scoring of dicentric chromosomes, micronuclei, single cell gel electrophoresis, and fluorescence signals*. Cytogenetic and Genome Research, 2004. 104(1-4): p. 383-389.
- [62] De Amicis, A., et al., *Dose estimation using dicentric chromosome assay and cytokinesis block micronucleus assay: Comparison between manual and automated scoring in triage mode*. Health Physics, 2014. 106(6): p. 787-797.
- [63] De Sanctis, S., et al., *Cytokinesis-block micronucleus assay by manual and automated scoring: Calibration curves and dose prediction*. Health Physics, 2014. 106(6): p. 745-749.
- [64] Garty, G., et al., *The RABiT: A rapid automated biodosimetry tool for radiological triage*. Health Physics, 2010. 98(2): p. 209-217.
- [65] Garty, G., et al., *The RABiT: A Rapid Automated Biodosimetry Tool for radiological triage. II. Technological developments*. International Journal of Radiation Biology, 2011. 87(8): p. 776-790.
- [66] Lyulko, O.V., et al., *Fast Image Analysis for the Micronucleus Assay in a Fully Automated High-Throughput Biodosimetry System*. Radiation Research, 2014. 181: p. 146-161.
- [67] Fenech, M., et al., *HUMN project initiative and review of validation, quality control and prospects for further development of automated micronucleus assays using image cytometry systems*. International Journal of Hygiene and Environmental Health, 2013. 216: p. 541-552.
- [68] Decordier, I., et al., *Automated image analysis of cytokinesis-blocked micronuclei: an adapted protocol and a validated scoring procedure for biomonitoring*. Mutagenesis, 2009. 24(1): p. 85-93.
- [69] Decordier, I., et al., *Automated image analysis of micronuclei by IMSTAR for biomonitoring*. Mutagenesis, 2011. 26(1): p. 163-168.
- [70] van de Loock, K., et al., *Maternal and gestational factors and micronucleus frequencies in umbilical blood: The newgeneris reha cohort in Crete*. Environmental Health Perspectives, 2011. 119(10): p. 1460-1465.

- [71] Kirsch-Volders, M. and M. Fenech, *Inclusion of micronuclei in non-divided mononuclear lymphocytes and necrosis/apoptosis may provide a more comprehensive cytokinesis block micronucleus assay for biomonitoring purposes*. *Mutagenesis*, 2001. 16(1): p. 51-58.
- [72] Nusse, M. and J. Kramer, *Flow cytometric analysis of micronuclei found in cells after irradiation*. *Cytometry*, 1984. 5(1): p. 20-25.
- [73] Nüsse, M. and K. Marx, *Flow cytometric analysis of micronuclei in cell cultures and human lymphocytes: Advantages and disadvantages*. *Mutation Research-Genetic Toxicology and Environmental Mutagenesis*, 1997. 392(1-2): p. 109-115.
- [74] Schreiber, G.A., et al., *Multiparametric flow cytometric analysis of radiation-induced micronuclei in mammalian cell cultures*. *Cytometry*, 1992. 13(1): p. 90-102.
- [75] Avlasevich, S.L., et al., *In vitro micronucleus scoring by flow cytometry: Differential staining of micronuclei versus apoptotic and necrotic chromatin enhances assay reliability*. *Environmental and Molecular Mutagenesis*, 2006. 47(1): p. 56-66.
- [76] Bryce, S.M., et al., *In vitro micronucleus assay scored by flow cytometry provides a comprehensive evaluation of cytogenetic damage and cytotoxicity*. *Mutation Research-Genetic Toxicology and Environmental Mutagenesis*, 2007. 630(1-2): p. 78-91.
- [77] Amnis Corp. (EMD Millipore), *INSPIRE User's Manual (version 4.0)*. 2010.
- [78] Amnis Corp. (EMD Millipore), *Image Data Exploration and Analysis Software (IDEAS) User's Manual (version 6.0)*. 2013.
- [79] Rodrigues, M.A., et al., *Automated Analysis of the Cytokinesis-Block Micronucleus Assay for Radiation Biodosimetry Using Imaging Flow Cytometry*. *Radiation Environmental Biophysics*, 2014a. 53(2): p. 273-282.
- [80] Cell Signaling Technology, *DRAQ5 Information*. 2009.
- [81] Alberts, B., Johnson, A., Lewis, J., Raff, M., Roberts, K., Walter, P., *Molecular Biology of the Cell*. 5th ed. 2008, New York: Taylor & Francis.
- [82] Thermo Scientific, *DAPI (4',6-diamidino-2'-phenylindole, dihydrochloride) Instructions*. 2010.
- [83] Rodrigues, M.A., et al., *Multi-parameter dose estimations in radiation biodosimetry using the automated cytokinesis-block micronucleus assay with imaging flow cytometry*. *Cytometry Part A*, 2014b. 85A(10): p. 883-893.
- [84] Fawcett, T., *An introduction to ROC analysis*. *Pattern Recognition Letters*, 2006. 27(8): p. 861-874.
- [85] Berger, M.E., et al., *Medical management of radiation injuries: Current approaches*. *Occupational Medicine*, 2006. 56(3): p. 162-172.

- [86] Haralick, R.M., K. Shanmugam, and I. Dinstein, *Textural features for image classification*. IEEE Transactions on Systems, Man and Cybernetics, 1973. smc 3(6): p. 610-621.
- [87] Kacprzak, J., et al., *Individual variations in the micronucleus assay for biological dosimetry after high dose exposure*. Mutation Research - Genetic Toxicology and Environmental Mutagenesis, 2013. 756(1-2): p. 196-200.
- [88] Wojcik, A., et al., *Validation of the micronucleus-centromere assay for biological dosimetry*. Genetics and Molecular Biology, 2000. 23(4): p. 1083-1085.
- [89] Darzynkiewicz, Z., et al., *Laser scanning cytometry for automation of the micronucleus assay*. Mutagenesis, 2011. 26(1): p. 153-161.
- [90] Leifert, W.R., et al., *Automation of the buccal micronucleus cytome assay using laser scanning cytometry*, in *Methods in Cell Biology*. 2011. p. 321-339.
- [91] Thierens, H., A. Vral, and L. De Ridder, *Biological dosimetry using the micronucleus assay for lymphocytes: Interindividual differences in dose response*. Health Physics, 1991. 61(5): p. 623-630.
- [92] Fenech, M., *The Lymphocyte Cytokinesis-Block Micronucleus Cytome Assay and its Application in Radiation Biodosimetry*. Health Physics, 2010. 98(2): p. 234-243.
- [93] Koksai, G., et al., *The dependence of the micronucleus yield in human lymphocytes on culture and cytokinesis blocking times*. Radiation Protection Dosimetry, 1989. 29(3): p. 209-212.
- [94] Lee, T.K., et al., *Assessment of two protocols for the human lymphocyte cytokinesis-blocked micronucleus assay*. Mutagenesis, 1995. 10(4): p. 375-377.
- [95] Lee, T.K., et al., *Reliability of finger stick capillary blood for the lymphocyte micronucleus assay*. Mutagenesis, 1997. 12(2): p. 79-81.
- [96] Deperas, J., et al., *CABAS: A freely available PC program for fitting calibration curves in chromosome aberration dosimetry*. Radiation Protection Dosimetry, 2007. 124(2): p. 115-123.
- [97] IAEA, *Cytogenetic Analysis for Radiation Dose Assessment*. 2001. Vienna.
- [98] Fenech, M. and A.A. Morley, *CYTOKINESIS-BLOCK MICRONUCLEUS METHOD IN HUMAN-LYMPHOCYTES - EFFECT OF INVIVO AGING AND LOW-DOSE X-IRRADIATION*. Mutation Research, 1986. 161(2): p. 193-198.
- [99] IAEA, *Cytogenetic Dosimetry: Applications in Preparedness for and Response to Radiation Emergencies*. 2011.
- [100] Flegal, F.N., et al., *QUICKSCAN DICENTRIC CHROMOSOME ANALYSIS FOR RADIATION BIODOSIMETRY*. Health Physics, 2010. 98(2): p. 276-281.

- [101] Quast, U., *Whole body radiotherapy: A TBI-guideline*. Journal of Medical Physics, 2006. 31(1): p. 5-12.
- [102] Kirsch-Volders, M., et al., *In vitro genotoxicity testing using the micronucleus assay in cell lines, human lymphocytes and 3D human skin models*. Mutagenesis, 2011. 26(1): p. 177-184.
- [103] Kirsch-Volders, M., et al., *Report from the in vitro micronucleus assay working group*. Mutation Research - Genetic Toxicology and Environmental Mutagenesis, 2003. 540(2): p. 153-163.
- [104] Kirsch-Volders, M., et al., *Report from the vitro micronucleus assay working group*. Environmental and Molecular Mutagenesis, 2000. 35(3): p. 167-172.

## APPENDIX I – AUTOMATED CBMN: STANDARD PROTOCOL ON THE ISX

Day 1 – \_\_\_\_\_

Blood draw time: \_\_\_\_\_

Donor #: \_\_\_\_\_

### IRRADIATION

1. Irradiate all blood tubes according to the table below. Complete all rows/columns as necessary.

Tube Number	Planned Dose (Gy)	Delivered Dose (Gy)	Irradiation program
1	0	0	---
2	1		
3	2		
4	3		
5	4		

### CULTURE SET-UP

1. Prepare 100 mL of RPMI media as follows:
  - a. 87.8 mL RPMI 1640 media (Lot: \_\_\_\_\_, Exp: \_\_\_\_\_)
  - b. 1 mL L-glutamine, penicillin-streptomycin (Lot: \_\_\_\_\_, Exp: \_\_\_\_\_)
  - c. 10 mL FBS (Lot: \_\_\_\_\_, Exp: \_\_\_\_\_)
  - d. 1.2 mL PHA (Lot: \_\_\_\_\_, Exp: \_\_\_\_\_)
2. Add 18.0 mL of media to each of the labelled 25 cm<sup>2</sup> flasks.
3. Put all flasks (numbered 1-5) in the incubator to warm up to 37 °C for 1hr before culture.
4. Transfer 2 mL of irradiated blood to each numbered flask and mix gently.
5. Incubate all flasks in a flat position for 24 h at 37 °C in the 5% CO<sub>2</sub> incubator.
6. **Time of incubation:** \_\_\_\_\_

Day 2 – \_\_\_\_\_

1. At **TIME 24 h** ( \_\_\_\_\_ ) after starting the culture, add 80.0 µL of Cytochalasin B @ 1.5 mg/mL stock solution in DMSO, to all flasks (final concentration 6.0 µg/mL) (Lot: \_\_\_\_\_).
2. Incubate in a flat position for another 48 h at 37°C in the 5% CO<sub>2</sub> incubator.

Day 4 - \_\_\_\_\_

At **72h** ( \_\_\_\_\_ ) after starting the culture:

1. Prepare a 1X solution of FACS Lysing solution:

- a. Total volume of solution needed = 210 mL
  - b. Amount of FACS Lysing solution needed = Total volume x 10% = 21 mL
  - c. Amount of deionized water needed = 1(a) – 1(b) = 189 mL
  - d. Lot #: \_\_\_\_\_
2. Transfer contents of each culture flask to a 50 mL polypropylene tube
  3. Spin at 200 x g (900 rpm) for 8 min at room temp.
  4. Aspirate supernatant and resuspend pellet
  5. Add 40 mL of 1X FACS Lysing solution to each tube
  6. Mix immediately and incubate at room temp for 10 min
  7. Spin at 400 x g (1300 rpm) for 10 min at room temp
  8. Aspirate supernatant and resuspend pellet in 10 mL of PBS
  9. Spin at 400 x g (1300 rpm) for 10 min at room temp
  10. Aspirate supernatant and resuspend pellet in 10 mL of PBS
  11. Spin at 400 x g (1300 rpm) for 10 min at room temp
  12. Aspirate supernatant and resuspend pellet in 100  $\mu$ L of PBS
  13. Stain each tube with a 1:100 concentration of DRAQ5 as follows:

**Tube #1 – 0 Gy**

1. Perform a cell count using the TC10 cell counter
  - a. Side 1: \_\_\_\_\_, Side 2: \_\_\_\_\_,  
Average: \_\_\_\_\_ c/mL
2. Calculate the amount of 1:100 dilution of DRAQ5 to add to the sample:
  - b. Average cell count/ $4 \times 10^5$  = \_\_\_\_\_ /  $4 \times 10^5$  = \_\_\_\_\_ uL

**Tube #2 – 1 Gy**

1. Perform a cell count using the TC10 cell counter
  - a. Side 1: \_\_\_\_\_, Side 2: \_\_\_\_\_,  
Average: \_\_\_\_\_ c/mL
2. Calculate the amount of 1:100 dilution of DRAQ5 to add to the sample:
  - b. Average cell count/ $4 \times 10^5$  = \_\_\_\_\_ /  $4 \times 10^5$  = \_\_\_\_\_ uL

**Tube #3 – 2 Gy**

1. Perform a cell count using the TC10 cell counter
  - a. Side 1: \_\_\_\_\_, Side 2: \_\_\_\_\_,  
Average: \_\_\_\_\_ c/mL
2. Calculate the amount of 1:100 dilution of DRAQ5 to add to the sample:
  - b. Average cell count/ $4 \times 10^5$  = \_\_\_\_\_ /  $4 \times 10^5$  = \_\_\_\_\_ uL

**Tube #4 – 3 Gy**

1. Perform a cell count using the TC10 cell counter
  - a. Side 1: \_\_\_\_\_, Side 2: \_\_\_\_\_,  
Average: \_\_\_\_\_ c/mL
2. Calculate the amount of 1:100 dilution of DRAQ5 to add to the sample:
  - b. Average cell count/ $4 \times 10^5$  = \_\_\_\_\_ /  $4 \times 10^5$  = \_\_\_\_\_ uL

**Tube #5 – 4 Gy**

1. Perform a cell count using the TC10 cell counter
  - a. Side 1: \_\_\_\_\_, Side 2: \_\_\_\_\_,  
Average: \_\_\_\_\_ c/mL
2. Calculate the amount of 1:100 dilution of DRAQ5 to add to the sample:
  - b. Average cell count/ $4 \times 10^5$  = \_\_\_\_\_ /  $4 \times 10^5$  = \_\_\_\_\_ uL

## References

1. R.A. Diamond and S. DeMaggio. In Living Color. Springer. 2000
2. M.G. Ormerod. Flow Cytometry. 3<sup>rd</sup> ed. 2000.

## ImageStream<sup>X</sup> Settings

### **Lasers:**

<b>Laser</b>	<b>Power (mW)</b>
BF	
658	20.0
785	

### **Classifiers:**

<b>Classifier</b>	<b>Channel</b>	<b>Value</b>
Area Lower Limit	1	75
Area Lower Limit	5	75

## Experiment Notes